Measuring human tissue at millimetre wavelengths

Samuli Lehtelä

School of Electrical Engineering

Thesis submitted for examination for the degree of Master of Science in Technology.

Espoo November 20, 2017

Thesis supervisor:

Prof. Antti Räisänen

Thesis advisors:

D.Sc. (Tech.) Aleksi Tamminen

M.Sc. (Tech.) Mika Salkola

D.Sc. (Tech.) Juha Ala-Laurinaho

Aalto University
School of Electrical
Engineering

AALTO UNIVERSITY
SCHOOL OF ELECTRICAL ENGINEERING

ABSTRACT OF THE
MASTER'S THESIS

Author: Samuli Lehtelä

Title: Measuring human tissue at millimetre wavelengths

Date: November 20, 2017 Language: English Number of pages: 12+84

Department of Electronics and Nanoengineering

Professorship: Radio Engineering

Supervisor: Prof. Antti Räisänen
Advisors: D.Sc. (Tech.) Aleksi Tamminen, M.Sc. (Tech.) Mika Salkola, D.Sc. (Tech.) Juha Ala-Laurinaho

This Master's thesis studies medical applications of millimetre-waves. The literature review introduces past studies of different millimetre- and submillimetre-wave medical applications. The literature review consists of possible applications in dermatology, dentistry and ophthalmology. The aim of this work is to measure a human tissue phantom and to determine the material parameters of the human tissue phantom.

First the millimetre- and submillimetre-waves are presented and the previous studies of possible medical applications at these wavelengths. The studies are compared to current diagnostic applications and alternative applications. Furthermore, the theory of the human tissue measurement at millimetre wavelengths is presented and a human tissue reflection measurement is simulated with MATLAB.

In the experimental part, a quasi-optical system operating at 220 - 330 GHz was built. Two different size silicon pieces, one cyclic-olefin copolymer (COC) piece, and one polytetrafluoroethylene (PTFE) piece was measured as reference. Moreover, measurements included materials with spherical geometry. The amplitude responses of the measurements were fitted with simulations and the relative permittivities of the materials were determined from the simulation results at the measurement frequencies.

The relative permittivity of COC was determined to be $2.321 - j9\times10^{-11}$ and the relative permittivity of PTFE was determined to be $2.023 - j2.41\times10^{-5}$. The relative permittivity of the larger silicon piece was determined to be $11.485 - j0.395$ and the relative permittivity of the smaller piece of silicon was determined to be $11.27 - j11\times10^{-4}$. The relative permittivities of spherical objects could not be determined due to the assumed phase-centre shift, but the effect of the curvature of the material to the reflection was analysed.

Keywords: electromagnetics, lossy media, reflection, stratified medium, millimetre wavelengths, quasi-optics

AALTO-YLIOPISTO
SÄHKÖTEKNIIKAN KORKEAKOULU

DIPLOMITYÖN
TIIVISTELMÄ

Tekijä: Samuli Lehtelä

Työn nimi: Ihmisen kudoksen mittaaminen millimetriaalloilla

Päivämäärä: November 20, 2017 Kieli: Englanti Sivumäärä: 12+84

Elektroniikan laitos

Professuuri: Radioteknikka

Työn valvoja: Prof. Antti Räisänen

Työn ohjaajat: TkT Aleksi Tamminen, DI Mika Salkola, TkT Juha Ala-Laurinaho

Tässä diplomityössä käsitellään millimetriaaltojen käyttöä lääketieteellisissä sovelluksissa. Kirjallisuuskatsaus kattaa laajahkon otannan erilaisiin sovellusmahdollisuuksiin diagnostiikassa. Työn painopiste on ihmiskudoksen kaltaisen aineen mittauksessa ja kudoksen ominaisuuksien määrittelyssä mittausten avulla. Työssä on toteutettu kvasioptinen mittausjärjestelmä, jolla voidaan mitata ihmisen kudosta.

Ensimmäiseksi esitellään lyhyesti millimetri- ja alimillimetriaaltoalue sekä aiempi tutkimustyö näillä aallonpituuksilla lääketieteellisiin sovelluksiin. Tutkimuksien tuloksia arvioidaan ja vertaillaan jo olemassa oleviin sovelluksiin sekä vaihtoehtoisiin sovelluksiin. Teoriaa ihmiskudoksen mittauksesta millimetriaalloilla esitellään ja heijastusesimerkki ihmiskudoksesta esitellään MATLAB:illa.

Kokeellista osuutta varten rakennettiin kvasioptinen mittausjärjestelmä, joka toimii 220 - 330 GHz:in taajuuksilla. Vertailumateriaaleina käytettiin kahta eri kokoista pii-kappaletta, jaksollista olefiinisekapolymeeriä (COC) sekä polytetrafluorieteeniä (PTFE). Lisäksi mittauksia tehtiin pallomaisien materiaalien kanssa. Mittaustulosten amplitudivasteet sovitettiin simuloimalla ja niiden avulla määriteltiin materiaalin suhteellinen permittiivisyys mittaustaajuuksilla.

COC:n permittiivisyydeksi saatiin 2.321 - $j9\times10^{-11}$ ja PTFE:n permittiivisyydeksi saatiin 2.023 - $j2.41\times10^{-5}$. Isomman pii-kappaleen permittiivisyydeksi saatiin 11.485 - $j0.395$ ja pienemmän pii-kappaleen permittiivisyydeksi saatiin 11.27 - $j11\times10^{-4}$. Pallomaisien materiaalien permittiivisyyksiä ei pystytty määrittämään, mutta materiaalin kaarevuuden vaikutusta heijastuskertoimeen analysoitiin.

Avainsanat: sähkömagnetiikka, häviöllinen aine, heijastus, kerroksellinen väliaine, millimetriaalto, kvasioptiikka

AALTO-UNIVERSITETET
HÖGSKOLAN FÖR ELEKTROTEKNIK

SAMMANDRAG AV
DIPLOMARBETET

Författare: Samuli Lehtelä

Titel: Mätning av människoväv på millimeter våglängder

Datum: November 20, 2017 Språk: Engelska Sidantal: 12+84

Institutionen för elektronik och nanoteknik

Professur: Radioteknik

Övervakare: Prof. Antti Räisänen

Handledare: TkD Aleksi Tamminen, DI Mika Salkola, TkD Juha Ala-Laurinaho

Detta diplomarbete studerar millimeter och submillimeter vågor i medicinska applikationer. Litteraturöversikten handlar om tidigare undersökningar av potentiella tillämpningar i diagnostik. Fokus av detta arbete är i definiera egenskaper av människoväv liknande material med hjälp av mätningar.
Först presenteras millimeter och submillimeter våglängder och tidigare undersökning för diagnostik på dessa våglängder. Undersökningar jämföras med tillämpningar i bruk i diagnostic samt med alternativa tillämpningar. Ytterligare teori om människoväv mätning på millimeter våglängder presenteras samt ett exempel av reflektion från människoväv presenteras med MATLAB.
I den experimentella delen byggdes en kvasi-optisk mätningssystem som opererar på 220 - 330 GHz. Två kisel bitar av olika storlek, en periodisk olefinkopolymer (COC) bit, och en polytetrafluoreten (PTFE) bit användes som referens material. Ytterligare mätningar gjordes med material med sfärisk geometri. Resultat av mätningarnas amplitud var förlikad med simulering och material egenskaper var definierats med hjälp av simuleringsresultat.
Relativ permittivitet av COC definierades som 2.321 - $j9\times10^{-11}$ och relativ permittivitet av PTFE definierades som 2.023 - $j2.41\times10^{-5}$. Relative permittivitet av den större kisel biten definierades som 11.485 - $j0.395$ och relativ permittivitet av den smalare kisel biten definierades som 11.27 - $j11\times10^{-4}$. Relativ permittivitet av sfäriska material var inte möjligt att definiera men effekt av krökning av materialen med reflektion var analyserad.

Nyckelord: elektromagnetik, förlustig medium, reflektion, millimeter våglängder, kvasi-optik

Preface

This thesis was done at Asqella Oy and at the Department of Electronics and Nanoengineering at Aalto University's School of Electrical Engineering.

First of all, I want to thank my supervisor Professor Antti Räisänen for sharing his knowledge of radio engineering. In addition, I want to thank Aleksi Tamminen and Arttu Luukanen for the opportunity to work and write this thesis at Asqella. Furthermore, I want to thank Aleksi Tamminen for his patience, guidance, and inspirational conversation during this thesis. His support has been of the utmost importance during this work. I want to extend my gratitude to Juha Ala-Laurinaho for his help with the measurement at Aalto University and Mika Salkola for sharing his knowledge of ophthalmology.

Last but not least, I want to thank everybody at Asqella for the memorable moments and kind words during my learning process, and my friends and family for their support and understanding during this work.

Helsinki, November 20, 2017

Samuli E. Lehtelä

Contents

Symbols and abbreviations

Symbols

a	aperture radius
$\mathbf{B}$	magnetic flux density
B_{-3dB}	half-power bandwidth
BW	bandwidth
c	speed of light in vacuum $\approx 2.998 \times 10^8$ m/s
$\mathbf{D}$	electric flux density
D_m	diameter of reflector
d_1	diameter of mirror 1
d_2	diameter of mirror 2
d_{alias}	distance of the object from the horn antenna
$\mathbf{E}$	electric field intensity
$\mathbf{E}_i$	incident electric field intensity
$\mathbf{E}_r$	reflected electric field intensity
$\mathbf{E}_t$	transmitted electric field intensity
E_{i+}	amplitude of forward moving incident electric field intesity
E_{i-}	amplitude of backward moving electric field intensity
E_{t+}	amplitude of forward moving transmitted electric field intensity
E_{t-}	amplitude of backward moving electric field intensity
$F(t)$	Signal response in time-domain
f	frequency
f_1	first relaxation frequency of water
f_2	second relaxation frequency of water
f_i	frequency ith frequency point
f_{r0}	resonant frequency of empty cavity
f_r	resonant frequency of fully loaded cavity
f_s	sampling frequency
fl_{in}	effective focal length of first mirror
fl_{out}	effective focal length of second mirror
$G(f)$	Signal response in frequency domain
GW	width of the filtering function
$\mathbf{H}$	magnetic field intensity
$\mathbf{H}_i$	incident magnetic field intensity
$\mathbf{H}_r$	reflected magnetic field intensity
$\mathbf{H}_t$	transmitted magnetic field intensity
HF	Hann function
i	the number of the fraction
$\mathbf{J}$	electric current density
$\mathbf{J}_m$	magnetic current density
j	imaginary unit $= \sqrt{-1}$
$\mathbf{k}$	wavenumber vector
k	wavenumber $= \lvert\mathbf{k}\rvert$

k_0	free-space wavenumber
k_1	wavenumber in medium 1
k_2	wavenumber in medium 2
k_r	wavenumber in material under test
L	Length of Pickett-Potter horn
l_i	length of the ith slab
l_r	thickness of the material under test
$\mathbf{M}$	magnification of the mirror system
M_ϕ	integer value of phase unwrapping algorithm
m_{alias}	number of coefficients
N	number of layers
N_{Signal}	number of measurement points
n	refractive index
n_1	refractive index of medium 1
n_2	refractive index of medium 2
n_{alias}	number of multiple reflections
$O_\phi(f)$	linear interpolated fit of $\phi(f)$
$\mathbf{P_e}$	polarisation density
pc	phase centre of the horn
$p_{w,i}$	water fraction part of the ith slab
Q	quality factor
Q_0	unloaded quality factor
Q_d	quality factor of the material under test
Q_e	external quality factor
Q_L	loaded quality factor
Q_m	quality factor of metal walls of the resonator
Q_{m0}	quality factor of metal walls of the resonator
Q_r	radiation quality factor
R	reflection coefficient
R_1	reflection coefficient of interface 1
R_2	reflection coefficient of interface 2
R_c	radius of curvature of the propagating beam
R_i	reflection coefficient of the ith slab
$R_{\text{steel ball}}$	radius of curvature of the steel ball
$\mathbf{r}$	3D arbitrary length vector
r	distance from the horn
T	transmission coefficient
T_E	edge taper
T_w	temperature of water
t	time
t_{alias}	aliased time instant
t_{centre}	centre time instant
t_{high}	higher boundary of alias-free distance
t_{low}	lower boundary of alias-free distance
t_{maximum}	maximum time instant
$\tan\delta$	loss tangent
$\mathbf{u}_x$	unit vector in x-direction

$\mathbf{u}_y$	unit vector in y-direction
$\mathbf{u}_z$	unit vector in z-direction
v_p	velocity of a wave in a medium
W_{alias}	alias-free distance
x	distance from the focal point
Z	wave impedance in complex medium
$\mathbf{z}$	position in z-direction
z	magnitude of $\mathbf{z}$ position vector
$z_{0,\text{steel ball}}(x)$	height of the curvature
$z_{1,\text{steel ball}}(x)$	height of the curvature at the distance of the steel ball
z_A	equal waist position
z_c	confocal distance
Γ_1	total overall reflection coefficient response
Γ_h	total reflection of a homogeneous slab
Γ_{Mirror}	reflection coefficient of planar mirror
Γ_{RAM}	reflection coefficient of radar absorbing material
Γ_r	total reflection of incident plane wave
δ	effective electrical length
δ_i	effective electrical length of the ith slab
$\overline{\overline{\varepsilon}}$	dyadic permittivity
ε	complex relative permittivity
ε_0	dielectric constant in vacuum $\approx 8.854 \times 10^{-12}$ F/m
ε_1	complex permittivity in medium 1
ε_2	complex permittivity in medium 2
$\varepsilon_\infty(T_w)$	second high-frequency constant of water at temperature T_w
ε_a	dielectric constant of half-space a
ε_b	dielectric constant of half-space b
$\varepsilon_{\text{collagen}}$	dielectric constant of collagen fibre
$\varepsilon_{\text{cornea},i}$	permittivity of ith slab of the cornea
ε_r	dielectric constant of the medium r
$\varepsilon_r^{'}$	real part of relative permittivity
$\varepsilon_r^{''}$	imaginary part of relative permittivity
$\varepsilon_{\text{s}}(T_w)$	static dielectric constant of water at temperature T_w
$\varepsilon_{\text{s1}}(T_w)$	first high frequency constant of water at temperature T_w
$\varepsilon_w(f)$	complex permittivity of water
$\overline{\overline{\zeta}}$	magnetoelectric coupling dyadic
η	wave impedance
η_1	wave impedance in medium 1
η_2	wave impedance in medium 2
$\eta_{\text{curvature}}$	efficiency of the phase difference
λ	wavelength
λ_0	free-space wavelength
λ_{centre}	wavelength at the centre frequency of the Pickett-Potter horn
λ_r	wavelength in the MUT
$\overline{\overline{\mu}}$	dyadic permeability

μ	complex relative permeability
μ_0	permeability in vacuum $\approx 4\pi \times 10^{-7}$ H/m
ν	angular frequency $= 2\pi f$
$\overline{\overline{\xi}}$	magnetoelectric coupling dyadic
π	pi ≈ 3.14159264
ϱ	electric charge density
ρ_r	reflection coefficient of voltage
$\sigma(T_w, S)$	conductivity of seawater at temperature T_w and salinity S
$\phi(f)$	unwrapped phase of measurement data
ω	beam radius
ω_0	beam waist radius at $z = 0$
ω_{01}	beam radius at mirror 1
ω_{02}	beam radius at mirror 2
ω_{in}	beam radius at focal point of first mirror
ω_{out}	beam radius at focal point of second mirror

Abbreviations

CCD	charge-coupled device
CCT	central cornea thickness
COC	cyclic-olefin copolymer
CTWC	corneal tissue water content
dB	decibel
EM	electromagnetic
FFT	Fast Fourier Transformation
FSPL	free-space path loss
FT	Fourier transform
IFFT	invers fast Fourier transform
LPI	laser Doppler perfusion imaging
MUT	material under test
NaCl	sodium chloride
OAP	off-axis parabolic mirror
PNA	performance network analyzer extension
ppt	parts per thousand
PS-OCT	polarisation sensitive optical coherence tomography
PTFE	polytetrafluoroethylene
QOW	quasi-optical waveguide
RAM	radar absorbing material
SNR	signal-to-noise ratio
TDR	time-domain reflectometry
THS	tissue hydration
THz	terahertz
THz-TDS	terahertz time-domain spectroscopy
TPI	terahertz pulse imaging
VNAX	vector network analyser extension

1 Introduction

Radiowaves are electromagnetic waves propagating in vacuum with the velocity of light. Generally, frequencies from 1 Hz to about 3 THz are called radiowaves. The frequencies higher than 3 THz are called infrared radiation, however, the frequency limits are loosely defined and may be different from one source to another. Figure 1.1 illustrates the electromagnetic spectrum with different wavelengths, corresponding frequencies, comparable size of the wavelength and sources of different frequencies and equipment which utilises the different frequencies.

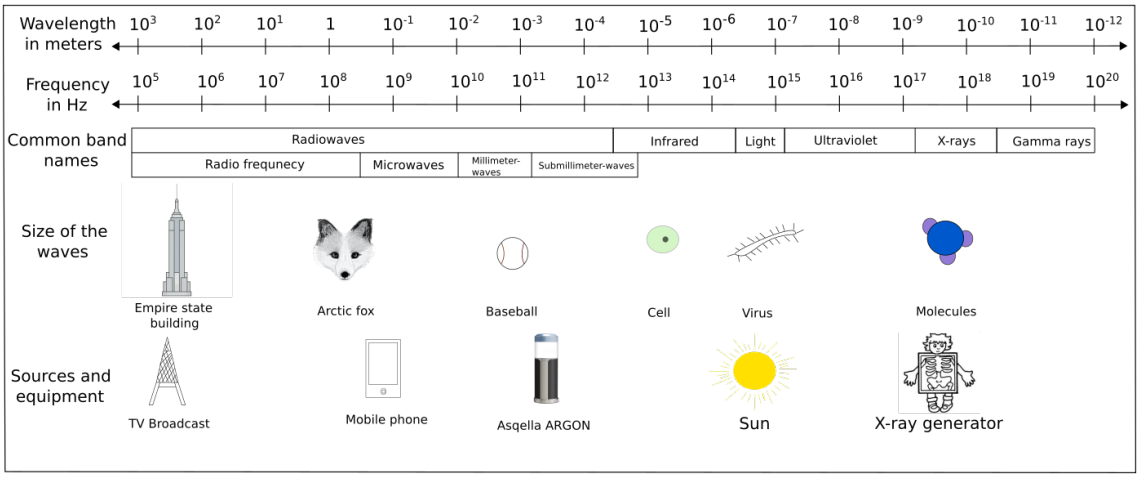

Figure 1.1: The electromagnetic spectrum.

Different frequencies are used to different applications depending on their wanted functionality and global location where the radiowaves are used. In long distance communication lower frequencies provide better signal strength. However, the lower the frequency is the less the signal can transfer data from one device to another. As an example devices using Wi-Fi technology use 2.4 GHz or 5.8 GHz frequencies, which allows large data transfer but the distance the signal can be detected from is about 46 meters indoors.

Radiowaves may also be used to image objects. If the wavelength is smaller than the size of the object the corresponding frequency may be used to image the object. In addition, the radio waces may be used to determine the electrical properties of the material the radiowave is illuminated to.

1.1 Millimetre and submillimetre technology

Millimetre wavelengths are defined as electromagnetic (EM) waves in the frequency range 30 - 300 GHz. This frequency range corresponds to 10 - 1 mm wavelengths. Millimetre waves are shorter than microwaves (10 - 1 cm) and longer than submillimetre waves (1 - 0.1 mm or 3 mm - 30 μm [1]). Although experiments with millimetre

wavelengths have been conducted since the early 1900 century, it was not until the 1970s, major application utilising millimetre waves were created. The primary driver of millimetre- and submillimetre-wave technology has been applications in radio astronomy.

Millimetre- and submillimetre-wave research in radio astronomy has three major interest areas, extragalactic radio sources, microwave background radiation, and research of interstellar molecules [2]. The primary driver of millimetre- and submillimetre-wave technology has been design of sensitive detectors to measure the radiation of extragalactic radio sources and microwave background radiation. The flux of stellar objects has been reported to peak at millimetre and submillimetre wavelengths.

Microwave background radiation has been vastly studied at millimetre and submillimetre wavelengths [2]. The black-body radiation of the background radiation at temperature of 3 K peaks at these wavelengths. The results have been more accurate than with longer wavelengths even though the concern of larger errors due to atmospheric radiation. Both on ground and space-borne observations millimetre observations indicate a slightly lower temperature than 3 K for the black-body radiation of the microwave background [3].

Wireless systems utilising millimetre wave technology has risen in the recent years. The need for standoff screening devices has fuelled research to better imaging techniques at millimetre and submillimetre wavelengths [4, 5]. Standoff screening devices ease the screening of a single person. In addition, it can provide anatomically discrete screening of contraband, loss prevention as well as medium and large sized weapons.

Another interest area of especially submillimetre wave commercial applications has been medical research. Millimetre and submillimetre waves penetrate little into biological tissue, and is therefore a suitable screening method for surface monitoring of biological tissue. Current interest of medical research at these wavelengths have been skin burn imaging [6], corneal tissue water content (CTWC) and central corneal thickness [7], and tumour region identification [8].

1.2 Scope and the aim of this thesis

This thesis discusses the possibility to use millimetre wavelengths to characterise material parameters, such as complex permittivity and thickness, of biological-like tissue. The thesis consists of literature review of medical research at millimetre and submillimetre wavelengths and currently used technologies of biological tissue characterisation. In addition, the thesis consists of theoretical review of measurements with millimetre waves, and an experimental part, wherein a millimetre wavelength measurement is implemented at frequency range from 220 GHz to 330 GHz.

The second chapter discusses briefly history of millimetre- and submillimetre-wave technology. In addition, previous studies of millimetre- and submillimetre-wave techniques in medical applications are presented. The possible medical applications

are compared to existing diagnostic tools used in diagnostics. Moreover, theory of millimetre wavelengths measurement is presented and a simulation example of human tissue reflection coefficient is presented and discussed.

The third chapter presents the measurement system built for the experimental part of this work. First the Gaussian beam and the conical dual-mode horn used as the radiation source is presented. The constructed beam waveguide is also presented as well as the materials used in the measurements.

The fourth chapter presents the signal processing and results of the measurements. Different measurements are analysed and differences between the measurement results are discussed.

The fifth chapter presents the parameter value estimation of the measured materials. The fitted parameter values are compared with literature values of the same material measured previously. The differences of the values are analysed as well.

The sixth chapter concludes the thesis and provides suggestions for future research of the subject.

2 Millimetre wave medical research

2.1 Medical research at millimetre and submillimetre wavelengths

Although the first submillimetre, or rather terahertz (THz), wave image was generated in 1960, [9], the bleeding edge of the millimetre and submillimetre technology has been the non-existence of components and sources for these wavelengths. Until the 1990s most sources where thermal sources or single-frequency molecular vapour lasers. During the 1990s non-linear optical techniques for frequency conversion encouraged new research at these wavelengths [10], particularly terahertz time-domain spectroscopy (THz-TDS) [11, 12].

As the first interest of submillimetre and millimetre tomography were transmission images of a leaf after it was removed from the host plant [13]. Two images were produced, first right after the removal of the leaf, and second 48 hours after plucking the leaf. The first images did not show significant difference in the transmission coefficient throughout the area as the leaf was still hydrated. Figure 2.1 presents the results of the two measurements of the same leaf [13]. However, due to the drying of the leaf, transmission coefficient difference was significant since the veins of the leaf only contained water.

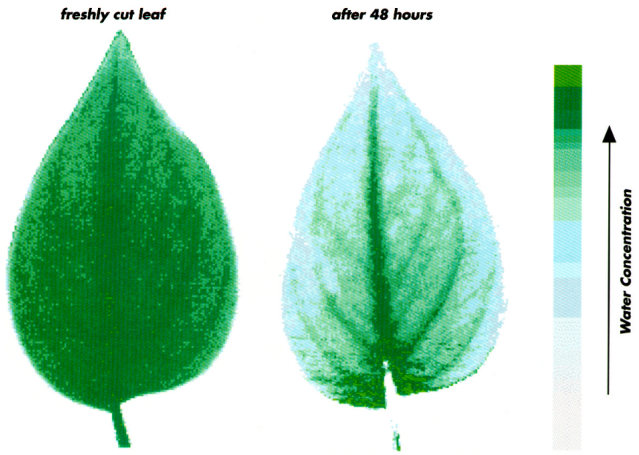

Figure 2.1: The results of [13], wherein the same leaf was measured after extraction and 48 hours after extraction. The green colour presents the magnitude of water absorption in the leaf.

2.2 Dermatology

Dermatology is the field of medicine, which focuses on hairs, nails, and skin as well as the diseases associated with these parts of the human body. Main focus is in treatment of burn wounds and skin cancers, such as basal-cell carcinoma, melanoma,

and squamous-cell carcinoma. Current examination is usually biopsy, which might be unpleasant for the patient. In addition, burns and tumours might occur on spots where excess removal of skin tissue is not preferred, such as face.

2.2.1 Burn wound detection

Burn wound, or simply burn, is an injury usually caused by instantaneously risen temperature in the tissue. Other causes for burns are electricity, radiation, and chemicals. Burns are categorised to four major groups depending on the depth of the injury. First degree burn is defined as superficial damage of the skin, second degree burn denotes damage that covers the epidermis and dermis of the skin tissue, third degree burn is damage that extends to fat tissue of the skin, and fourth degree burn denotes overall burnt limb. Figure 2.2 shows a simplified structure of human skin. The layers are not in scale and the total thickness of the skin tissue varies from 0.5 mm on the eyelids to 4 mm on the heels of feet. Depending on the degree of the burn the treatments vary from applying ointment to surgical removal of the damaged tissue.

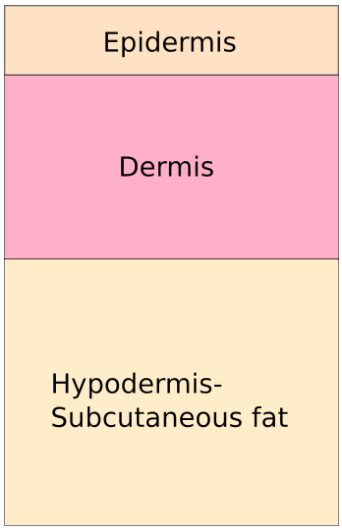

Figure 2.2: Simplified structure of human skin tissue.

Current diagnostic tools for burn depth examination are invasive and might be unappealing towards the patient, and thus the millimetre and submillimetre wave technology would offer a non-invasive option for such an examination. One of the first medically focused research utilising millimetre and submillimetre waves was published in the late 1990s [14], wherein burn wounds were measured on a extracted piece of chicken breast, i.e., *ex vivo* examination. The wounds were first produced with an argon ion laser. The burns were circularly shaped, and the severity of the burn was increasing towards the point where the laser beam was exposed.

A 3 cm $\times$ 2 cm tomogram with 0.25 mm steps was produced of the damaged area

by recording individual amplitudes of the reflected wave. One of the results was presented in [14], and Figure 2.3 shows the result of that measurement. The darkness of the pixel in the image represents the severity of the damage in the tissue. The burnt tissue is assumed to have higher water content, and reflect more of the transmitted millimetre and submillimetre radiation, and thus the burn margins are detectable from the normal tissue. The white area in Figure 2.3 represents undamaged skin tissue, wherein the water content is immutable compared to the damaged tissue. Although the change of the fluid content, which is mostly water, is assumed to be the primary cause of the difference in the amplitude of the reflected wave, the effects of other structural and chemical modifications of the damaged tissue cannot be excluded. In addition, the phase response might change in the damaged tissue compared with the undamaged tissue.

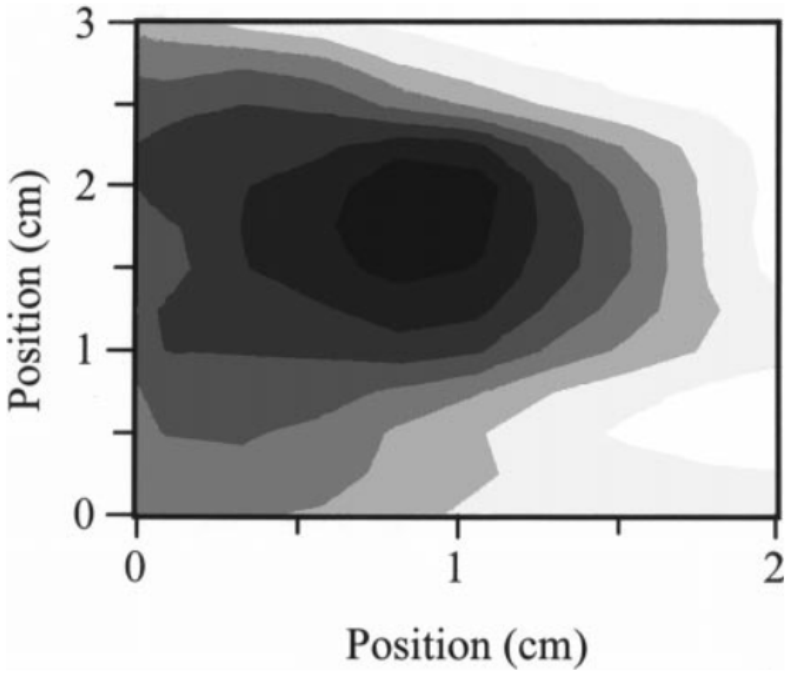

Figure 2.3: The false colour THz image of chicken breast reprinted from [14]. The darkness of the pixel means stronger reflection of the THz wave. In addition, stronger reflection indicates more severe damaged tissue since the water content of the tissue is higher.

Recent efforts in burn wound imaging with THz systems has been promising compared with other than millimetre of submillimetre techniques. In [15] a *ex vivo* burn examination was conducted on a piece of pork skin. The hypodermis was extracted from the pork skin resulting in a 2.5 mm thick piece. The material was then placed on a polypropylene substrate and a 25 mm $\times$ 50 mm grid was mounted on the material to ensure a flat surface. The piece was imaged once before applying an '+' shaped aluminium brand heated approximately to 315 °C.

After the brand was applied, a new reflection tomogram was obtained from the tissue. Figure 2.4 shows the results of the tomograms of undamaged skin, burnt skin, and the burnt skin with 3 layers of gauze placed on the skin. The result stated that the burn was distinguishable from the undamaged tissue. In addition, the benefit of broad band illumination is presented by the gauze layered image, where the shape of the gauze itself is visible as well as the burn. Moreover, the decreased blood flow at the burn margin is visible in both of the burn images.

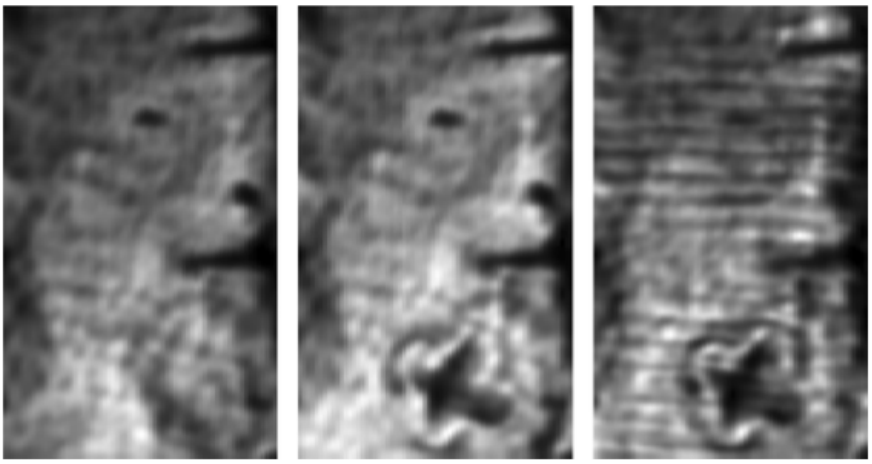

Figure 2.4: The results of the reflection tomograms of the porcine skin sample from [15]. (Left) The reflection tomogram of the undamaged porcine skin. (Middle) The reflection tomogram of damaged porcine skin. (Right) The reflection tomogram of damaged porcine skin with 3 layers of gauze stacked on the burn.

One of the first burn detection conducted *in vivo* was published in 2012 [16], wherein a burn was applied and measured in on an anaesthetised rat. The subject was placed on a plexiglass and tied to the surface with tape to ensure stagnation of the subject. A Mylar window was pressed on the subject to ensure planar surface of the observed area. The burn was applied with a brass brand, which formed a '+' shaped burn on the subject. Figure 2.5 shows the measured reflection tomograms of uninjured skin and injured skin after 10 minutes, 1 hour, and 7 hours after the brand was applied on the skin. The blood flow of the injured region is visible, since the whiter regions mark higher reflectivity of the THz wave. Figure 2.5 (b) shows the swelling of injured skin tissue caused by inrush of mostly water. Figure 2.5 (c) shows the clear '+' shaped burn that has begun to take its form, and the margin of decreased blood flow at the burn margin. Figure 2.5 (d) shows the burn 7 hours after the brand was applied on the skin, and the clear wound is visible with the increased fluid flow shown with higher reflectivity.

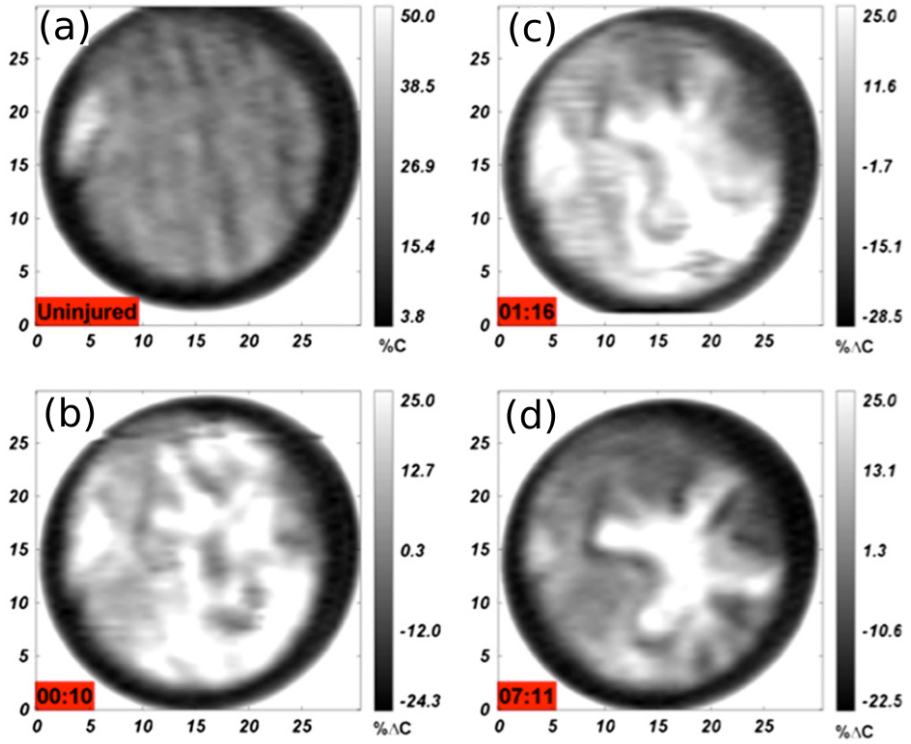

Figure 2.5: The results of the reflection tomograms of the rodent skin from [16]. (a) Uninjured skin tissue of the rodent, wherein the colour bar presents the water content of the tissue, (b) '+' shaped burn 0:10 hour after brand was applied on the skin, (c) 1 hour and 16 minutes post burn, and (d) 7 hours and 11 minutes post burn. The colour bar for (b)-(d) presents the water content change in the damaged skin.

Estimating the burn depth is linked with the overall fluid flow after the burn, and the water concentration of the injury can exceed 80 % during the first 10 minutes of the burn [17, 19]. Reference [16] claims to be the first study that presents clearly imaged region of stasis, i.e., tissue where normal fluid flow stops. This capability could be advantageous in pre-surgical examination, and to mark clear margins of damaged and undamaged tissue.

Other diagnostic methods applied for skin burn detection and severity quantification include laser Doppler perfusion imaging (LPI) and polarisation sensitive optical coherence tomography (PS-OCT). Both LPI and PS-OCT have shown potential to be used for skin burn identification, however, poor depth resolution and strong optical scattering tend to decrease the reliability of these techniques. Sensitivity of millimetre- and submillimetre-waves to water concentration may improve the depth estimation of burn wounds, and thus could be used in pre-examination of skin operation. In addition, accurate burn margin detections could be beneficial for patients since excess skin removal could be minimised. However, even the promising results such as [15, 16] do not have wide spread clinical acceptance at the moment.

2.2.2 Basal cell carcinoma

Another terahertz imaging technique used for biological tissue observation is terahertz pulsed imaging (TPI). TPI is based on photoconductive sources and utilises optoelectronic or photoconductive detectors. TPI has been used for observing basal cell carcinoma tumours [18]. Basal cell carcinoma is the most common form of skin cancer and it rarely spreads to other parts of the body, however, it might locally spread and grow rapidly. TPI used in [18] has approximately 80 μm axial resolution.

In [18] 15 reflection coefficients of healthy and infected areas were observed *in vitro*. The healthy samples were observed close to the infected area. More than half of the observations show a difference between healthy and infected area. The three results presented suggest that the tumour region results in higher reflection, and the healthy tissue in lower reflection. Since the THz radiation is highly sensitive for water absorption the result is considered to be due to increased hydration level in the tissue infected by the tumour.

The advantage of the basal cell carcinoma observation is the non-invasive observation method. Current diagnostic tools use visible examination and biopsy of the assumed area of the tumour, both of which are painful and time consuming. TPI would provide fast and painless diagnostic tool of the tumour and prevent excess skin removal from unwanted areas, such as face. However, more study is needed for identification of the tumour to ensure the accuracy of the TPI diagnosis. In addition, the increased hydration level of the tissue might not be unique enough for the tumour to determine the infected area since some of the tumours observed in [18] did not result in a significant increase in reflection compared with healthy tissue surrounding the tumour.

The work of Wallace, Arnone, and Pye, who also contributed in [18], continued in [20], wherein cancerous tumours were observed with commercial scanner based on TPI technique. The measurements were conducted *in vivo* and *ex vivo*, some from the same patient, whereas the previous [18] was conducted *in vitro*. The function of the commercial product, TPI scan by TeraView Ltd., is based on recording the reflection of tissue material placed on the quartz window of the device. The ultrafast pulses on the sample provide depth information of the sample. In addition, Fourier transform (FT) of recorded reflections offer spectroscopic information of the tissue.

Normal skin tissue was measured from 20 volunteers providing consistent data as the repeatability of the measurements were about 1 % and the day-to-day variation of the normal tissue measurements were less than 3 %. The *ex vivo* samples were acquired from 19 patients, six females and 13 males all ethnically caucasian. The samples included the tumour and healthy skin surrounding the tumour. The *in vivo* samples were acquired from five men, from which four of the patients' tumours were removed and used for *ex vivo* measurements.

Figure 2.6 shows *in vivo* TPI images of one basal cell carcinoma tumour from [20]. The results of these measurements showed that tumours had larger reflections than

normal tissue, based on a comparison made between the healthy tissue surrounding the tumour and reference measurements acquired from volunteers (normal tissue). The difference is seen also comparing the *in vivo* and *ex vivo* samples of the same tumour. However, the form of the reflection image did not exactly match due to the shrinking and dehydration of the skin sample when it was removed from the patient. In addition, the tumour margins detected with the TPI scan were sufficient enough when compared with histology of the tumour. The results of the study, [20], encourage for more research of basal cell carcinoma imaging and as the equipment at these wavelengths (3 mm to 15 μm) indicate that even shorter wavelengths could be used to acquire more accurate tumour margins and depth information.

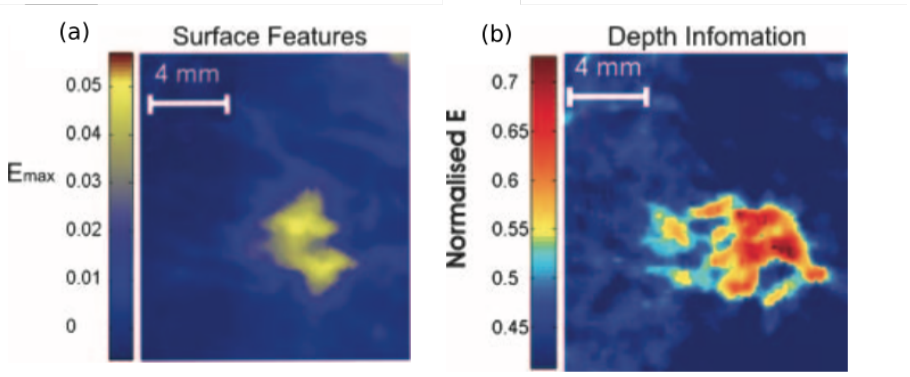

Figure 2.6: The results of *in vivo* TPI images of two patients reprinted from [20]. (a) Maximum reflected electric field plotted of one patient, (b) normalised electric field plotted of another patient. The higher intensity of the normalised electric field is assumed to be the result of the deeper tumour as the water content is higher.

2.3 Dentistry

Dentistry is the field of medicine, which focuses on diagnosis, treatment, prevention, and study of diseases of the oral cavity. Generally dentistry is associated with teeth, although it might also be extended to mean study of any tissue in the oral cavity. The visible characteristics on the tooth surface are nonexistent in the early stage of dental caries, and thus observing dental caries is difficult. Current examination uses X-ray, which reveals tooth decay at a late stage of the disease. The properties of the millimetre and submillimetre radiation might be used to image the decay at an early stage of the disease.

2.3.1 Dental caries

One of the first studies of submillimetre wave application for tissue identification and tooth decay (dental caries) was published in 1999 [21]. The measurement technique used was TPI. The observed tooth was an extracted premolar, i.e., a tooth between

corner (Canine) and back teeth (Molar). The tooth was approximately 9 mm thick and the tooth was sliced in half to observe the enamel, dentine, and the root canal. In addition, the data acquisition time was reduced by cutting the tooth. The provided reference images provided were a photograph and a charge-coupled device (CCD) camera image.

The study, [21], presented two different measurements conducted with TPI, refractive index imaging and panchromatic absorption imaging. The refractive index imaging used time-of-flight data, wherein the time delay of the transmitted waveform provided data of the different layers as the refractive index would be different. The results suggested that the enamel and dentine regions would have significantly different refractive indices at submillimetre wavelengths. The root canal was not visible with this post processing technique.

The same time-of-flight data was used to see the root canal. The peak power of the transmitted pulse was imaged so that the panchromatic absorption would be visible in the image. Figure 2.7 presents the results of [21] both the time delay and peak power of the transmitted pulse. The root canal was noted to be rather lossy and the assumption was that an empty root canal would be less absorptive than enamel and dentine regions. Therefore, the TPI could be used to provide information about the state of the root canal [21]. However, the tooth was examined *ex vivo*, and therefore, results might be drastically different when performed with living subjects.

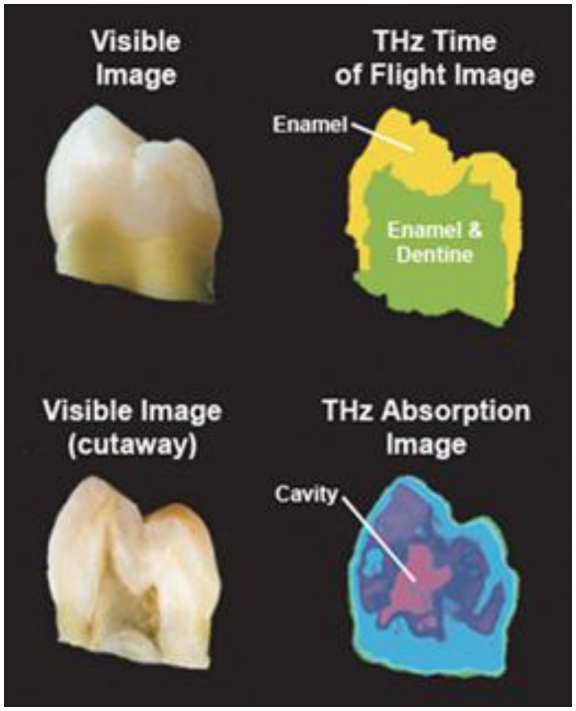

Figure 2.7: The results of tooth imaging reprinted from [21]. (Up)The result of time-of-flight measurement (time delay in transmission). (Down) The result of absorption measurement (transmitted peak power).

2.4 Ophthalmology

Ophthalmology is the field of medicine, which focuses on diagnosis, treatment and prevention of diseases of eyeball and orbit.

2.4.1 Corneal dystrophy

Corneal dystrophies are eye diseases that affects to the normal water-regulation process of the cornea, and they can be divided into three groups based on the location of the anomaly [22]. In addition, diseases, such as keratoconus, have been reported to have non-uniform changes in hydration of the cornea [23–26]. The small changes in hydration levels could be beneficial for millimetre and submillimetre wave imaging techniques in examination of these diseases.

The cornea is the outermost layer of the eye with a thin tear film on top of it, and a body of water beneath it is called the aqueous humour. Figure 2.8 shows a simplified structure of the cornea. The stroma is the largest layer of the cornea covering approximately 500 μm of the cornea. The other layers are about 5 - 15 μm thick. The corneal tissue water content (CTWC) in human eye is approximately 78 %, and the central corneal thickness (CCT) is approximately 580 μm [27]. The variation from person-to-person is estimated to be from 450 μm to 650 μm [28].

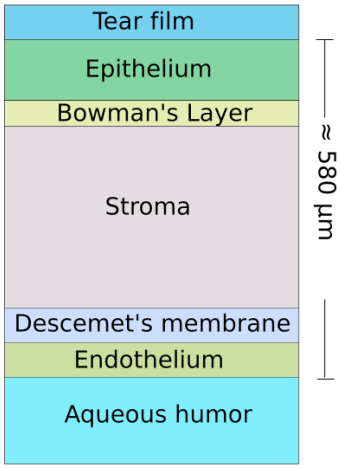

Figure 2.8: A simplified structure of human cornea. The thickness varies between 500-600 μm in a healthy cornea.

One of the first *ex vivo* studies of CTWC has shown excellent potential of millimetre and submillimetre wave techniques to map the hydration level, and thus the CCT of the cornea. In [29] a *ex vivo* porcine cornea was measured with a commercial TPI system (TPS Spectra 3000 CF system by TeraView Ltd.). It uses a photoconductive transceiver pumped with a mode-locked Ti:Sapphire laser generating a 90 femtosecond pulse with 80 MHz pulse repetition frequency, and average output power of 280 mW.

The signal is illuminated on the target in a 30° angle of incidence from the vertical plane. The reflected signal is recorded with a reflection-mode module, from which a 6 GHz frequency resolution spectrum can be acquired in 1 second.

Four different porcine corneas with different hydration levels from 79 % to 92 % were examined [29]. The corneas were placed in 0 %, 3 %, 5 %, and 7 % polyethylene glycol solutions containing 0.15 mol/litre sodium chloride (NaCl) for three days to obtain different hydration levels. Figure 2.9 presents the results of these four measurements. A decrease in the reflectivity is observable as the frequency grows, and the higher reflectivity of the THz wave at higher CTWC. The difference of these hydration levels are distinguishable at the lower frequencies than at the higher frequencies.

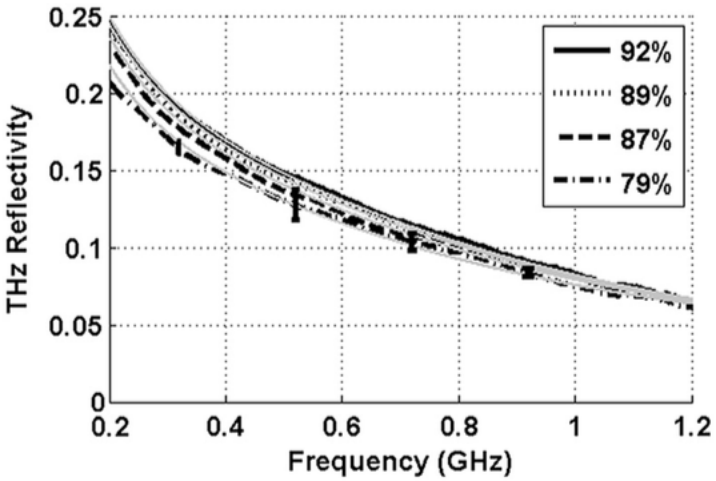

Figure 2.9: The results of 4 different corneal tissue water content (CTWC) profiles of four porcine corneas reprinted from [29]. Larger differences between the CTWC profiles is seen at lower frequencies. The reprinted figure has a typing error and the x-axis label should read: Frequency (THz).

In addition, [29] provided the first demonstration of *in vivo* cornea measurement, wherein 4 rabbit corneas where measured. The measurement system uses a Gunn diode source. The bias voltage of the source is swept from 7 to 10 V at kHz, resulting in a 100 GHz emitted signal with an approximately 1 GHz frequency modulated bandwidth. The reflected signal is detected with a pyroelectric detector with 1 $nW/Hz^{1/2}$ noise-equivalent power. The emitted signal is focused with a pair of polytetrafluoroethylene (PTFE) lenses with diameter of 50 mm and focal length of 100 mm for both lenses. The focused signal illuminates the target at 10° angle of incidence. The reflected signal is focused to the detector with another pair of PTFE lenses with identical parameters.

The rabbit corneas measured in [29] were chosen because the structure, size, and hydration is similar to humans [30]. Each one of the rabbits were anaesthetised and

placed on a table where the eye was held open and the cornea was dried with a gentle air blower. A thin Mylar window was gently placed on the cornea to ensure a planar geometry of the cornea. The cornea was imaged every 10 minutes until the water concentration did not change anymore. In addition, ultrasound pachymetry CCT measurements of the same cornea were measured and the CTWC of the cornea was calculated with the pachymetry data. Figure 2.10 shows the recorded THz wave reflection coefficients of the four corneas and the ultrasound pachymetry suggested CTWC data.

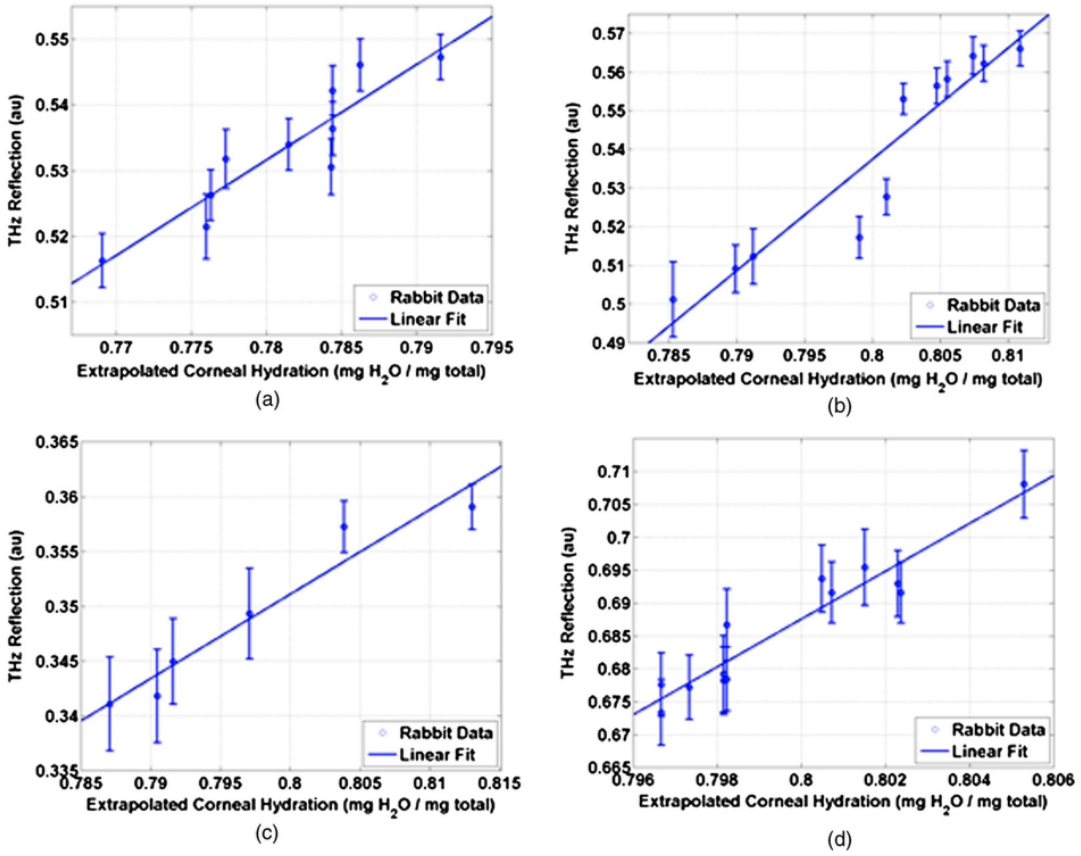

Figure 2.10: The results of 4 different rabbit corneas reprinted from [31]. The higher reflection coefficient is observable for all subjects as the CTWC grows.

The results of the four different rabbit corneas showed positive correlation with the reflected signal [31]. The change in the CTWC is only a few percent but the measurement system was able to identify various CTWC profiles within the limits with a 95 % confidence level. Tissue hydration sensitivities (TWS) were also computed for each cornea resulting in at least 0.33 % sensitivity. Even though the sensitivity level is less than what was expected with ultrasound pachymetry method which is the current standard used by ophthalmologists. However, the system can only map the CCT of the cornea due to rather large spot size of the incident signal. A broader mapping of the fluid shifts and different thicknesses of the cornea could be measured

with higher frequencies.

2.5 Safety concerns of electromagnetic radiation

The electromagnetic spectrum offers a non-invasive method for observing biological tissue structure. Wavelengths longer than the visible light's wavelength region (390 - 700 nm) may be utilised for surface observing of biological tissue. Shorter wavelengths e.g., 100 - 10 nm, are used as radiation therapy on cancer tumours, in order to break the biochemical structure of tumours and prevent its growth. In addition, wavelengths of 0.01 - 10 nm are used to image bones beneath biological tissue.

The propagation depth of the radiation depends on the wavelength and the photon of the radiation. In general the longer the wavelength is compared to the physical size of the object the less absorption of the energy is caused by the object. However, at extremely short wavelengths the photon enegy carries larger amount of energy than what an atom with low binding energy can absorb and the radiation will penetrate deeper until absorbed by an atom with high binding energy. Skin tissue cannot absorb X-rays and the radiation is absorbed in the molecules of bone.

The electromagnetic spectrum may be divided into two categories: non-ionising and ionising. The limit of ionising radiation depends on the energy of the photon. The radiation is non-ionising if the energy of the photon is less than 12 eV which is the needed amount of energy to break up skin molecules. Wavelengths from visible light region and longer do not carry enough energy to ionise the skin molecules. However, ionising radiation used with caution and precision may be beneficial, e.g., in radiation therapy.

Non-ionising electromagnetic radiation (EM) may be harmful even though it is not ionising. The harmful effects of these EM waves are divided into two categories: thermal and non-thermal effects [32]. Known thermal effects include cataract, risen temperature in cells, and burn wounds [33]. Therefore, the equivalent power density must be limited to 10 mW/cm^2 or less [34]. In addition, the exposure time must be limited with increasing power densities. The primary mechanism is that the power radiated on biological tissue is absorbed in the water molecules of the tissue. The harmful non-thermal effects include headache, fatigue, and insomnia. The mechanisms of these effects are not known and their existence is disagreed upon in the scientific community.

2.6 Maxwell's equations

The way electromagnetic fields are understood today would certainly be different if Maxwell had not published [35] in 1873. Although the combination of these fundamental equations for electromagnetic field theory are known as Maxwell's equations he based his work on empirical and theoretical work made by Faraday, Gauss, Ampere, and many others [36]. In addition, the vector forms presented next

where introduced in 1882 by Gibbs and Heaviside [37]. By combining the work of others Maxwell was able find relations between the electric field intensity $\mathbf{E}(\mathbf{r},t)$, magnetic field intensity $\mathbf{H}(\mathbf{r},t)$, electric current density $\mathbf{J}(\mathbf{r},t)$, and magnetic current density $\mathbf{J}_m(\mathbf{r},t)$. All of the quantities presented depend on the location $\mathbf{r}$ and time t. The first fundamental law is called Faraday's law

$$\nabla \times \mathbf{E}(\mathbf{r},t) = -\frac{\partial \mathbf{B}(\mathbf{r},t)}{\partial t} - \mathbf{J}_m(\mathbf{r},t), \tag{2.6.1}$$

where $\mathbf{B}(\mathbf{r},t)$ is the magnetic flux density. The second law is called Ampere's law

$$\nabla \times \mathbf{H}(\mathbf{r},t) = \frac{\partial \mathbf{D}(\mathbf{r},t)}{\partial t} + \mathbf{J}(\mathbf{r},t), \tag{2.6.2}$$

where $\mathbf{D}(\mathbf{r},t)$ is the electric flux density. The third and fourth laws are called Gauss laws for electric and magnetic sources and they are

$$\nabla \cdot \mathbf{D}(\mathbf{r},t) = \varrho(\mathbf{r},t) \text{ and} \tag{2.6.3a}$$

$$\nabla \cdot \mathbf{B}(\mathbf{r},t) = 0, \tag{2.6.3b}$$

where $\varrho(\mathbf{r},t)$ is the electric charge density. As Pozar states in [36] these cannot be related to each other in time-domain because of the phase difference. However, if time harmonic fields are considered, a relation can be found between the vectors. Lindell explains in [38] that for the most general linear, local, and non-dispersive medium the relations can be found as

$$\mathbf{D} = \overline{\overline{\varepsilon}} \cdot \mathbf{E} + \overline{\overline{\xi}} \cdot \mathbf{H} \text{ and} \tag{2.6.4a}$$

$$\mathbf{B} = \overline{\overline{\zeta}} \cdot \mathbf{E} + \overline{\overline{\mu}} \cdot \mathbf{H}, \tag{2.6.4b}$$

where $\overline{\overline{\varepsilon}}$ is the absolute dyadic permittivity, $\overline{\overline{\mu}}$ is the absolute dyadic permeability. The $\overline{\overline{\xi}}$ and $\overline{\overline{\zeta}}$ are magnetoelectric coupling dyadics. However, the media studied in this work are considered isotropic, i.e., the direction of the wave in the medium is uncorrelated to the medium parameters. Therefore, the medium parameters modify to

$$\overline{\overline{\varepsilon}} = \varepsilon, \tag{2.6.5a}$$

$$\overline{\overline{\mu}} = \mu, \text{ and} \tag{2.6.5b}$$

$$\overline{\overline{\zeta}} = \overline{\overline{\xi}} = 0. \tag{2.6.5c}$$

The equations (2.6.4a) and (2.6.4b) yield to

$$\mathbf{D} = \varepsilon \mathbf{E} \text{ and} \tag{2.6.6a}$$

$$\mathbf{B} = \mu \mathbf{H}. \tag{2.6.6b}$$

The absolute permittivity ε is the measure of resistance, e.g., a electromagnetic wave encounters when it creates an electric field in a medium. The absolute permittivity

ε is considered to be constructed of a relative part ε_r and an electric constant $\varepsilon_0 \approx 8.854 \times 10^{-12}$ F/m, and thus the absolute permittivity is

$$\varepsilon = \varepsilon_r \varepsilon_0. \tag{2.6.7}$$

The absolute permeability μ describes the formation of a magnetic field in a medium. The absolute permeability is generally defined similarly as the absolute permittivity. However, the materials studied in this thesis are nonmagnetic, and thus the relative permeability is considered $\mu_r = 1$ and for all materials the absolute permeability is

$$\mu = \mu_0 \approx 4\pi \times 10^{-7}\text{H/m}. \tag{2.6.8}$$

The relative permittivity may be a complex number, and the imaginary part describe the losses in a particular medium. The relative permittivity may be further expanded as

$$\varepsilon_r = \varepsilon_r^{'} - j\varepsilon_r^{''}, \tag{2.6.9}$$

where $\varepsilon_r^{'}$ is the real part of the relative permittivity, j is the imaginary unit, and $\varepsilon_r^{''}$ is the imaginary part of the relative permittivity. Furthermore, for passive material the $\varepsilon_r^{''}$ must be real and non-negative [38]. In literature the losses of the material is are often reported with the loss tangent $\tan\delta$, which is defined as

$$\tan\delta = \frac{\varepsilon_r^{''}}{\varepsilon_r^{'}}. \tag{2.6.10}$$

2.7 Propagation of an electromagnetic wave

2.7.1 Time-harmonic fields

Often it is convenient to consider only time-harmonic fields that oscillates sinusoidally at a certain angular frequency ν. Time-harmonic fields are convenient for computation and analysis of electromagnetic fields. In this work the fields are considered to be complex valued vectors and the applied time convention is $e^{j\nu t}$. The time derivatives in the Maxwell equations may be substituted by $j\nu$, and the Maxwell equations read

$$\nabla \times \mathbf{E}(\mathbf{r}) = -j\nu\mathbf{B}(\mathbf{r}) - \mathbf{J}_m(\mathbf{r}), \tag{2.7.1a}$$

$$\nabla \times \mathbf{H}(\mathbf{r}) = j\nu\mathbf{D}(\mathbf{r}) + \mathbf{J}(\mathbf{r}), \tag{2.7.1b}$$

$$\nabla \cdot \mathbf{E}(\mathbf{r}) = \frac{\varrho(\mathbf{r})}{\varepsilon}, \text{ and} \tag{2.7.1c}$$

$$\nabla \cdot \mathbf{H}(\mathbf{r}) = 0. \tag{2.7.1d}$$

2.7.2 Plane waves

In most cases the propagating plane waves are described as infinite parallel planes as in [39]. The plane waves propagate in the direction given by the wave vector $\mathbf{k}$. If $\mathbf{k}$ propagates in $+\mathbf{u}_z$ direction it can be written as,

$$\mathbf{k} = k\mathbf{u}_z, \tag{2.7.2}$$

where k is the wavenumber. For time-harmonic plane waves in sourceless medium the Maxwell equations may be written by replacing ∇ with $\mathbf{k}$ as

$$\mathbf{k} \times \mathbf{E}(z) = \nu\mathbf{B}(z), \tag{2.7.3a}$$

$$\mathbf{k} \times \mathbf{H}(z) = -\nu\mathbf{D}(z), \tag{2.7.3b}$$

$$\mathbf{k} \cdot \mathbf{E}(z) = 0, \text{ and} \tag{2.7.3c}$$

$$\mathbf{k} \cdot \mathbf{H}(z) = 0. \tag{2.7.3d}$$

The angular frequency ν of the electromagnetic wave defined as

$$\nu = 2\pi f, \tag{2.7.4}$$

where f is the frequency of the electromagnetic wave. The frequency can be determined as

$$f = \frac{v_p}{\lambda}, \tag{2.7.5}$$

where v_p is the phase velocity of the propagating wave and λ is the wavelength of the wave. The velocity of the wave depend on the material parameters of the medium as

$$v_p = \frac{1}{\sqrt{\varepsilon\mu}} = \frac{c}{\sqrt{\varepsilon_r}}, \tag{2.7.6}$$

where c is the speed of light in vacuum. The phase velocity relates to the wavenumber as

$$k = \frac{\nu}{v_p} = \frac{2\pi}{\lambda}. \tag{2.7.7}$$

The wavenumber k is the measure of spatial frequency of a wave. The wavenumber for a wave propagating in vacuum k_0 is defined as

$$k_0 = \frac{2\pi}{\lambda_0}, \tag{2.7.8}$$

where λ_0 is the wavelength of the propagating wave in vacuum defined as

$$\lambda_0 = \frac{c}{f}. \tag{2.7.9}$$

In addition the wavenumber depends on the material parameters, and thus, the wavenumber is complex if ε_r is complex. Furthermore, the wavenumber may be expanded as

$$k = k_0\sqrt{\varepsilon_r} = k_0 n, \tag{2.7.10}$$

where $n = \sqrt{\varepsilon_r}$ is the refractive index of the medium.

2.8 Reflection and transmission from an interface

When a travelling wave from a medium 1 with refractive index n_1 comes to a boundary at $z = 0$ to medium 2 with refractive index n_2, a portion of the wave is reflected away from the boundary and other part is absorbed, or transmitted, in to the other medium [36]. Let us consider a plane wave, which travels perpendicularly in $\mathbf{u}_z$ direction as in [40]. For simplicity the incident electric field $\mathbf{E}_i(z)$ is assumed to be linearly polarised in $\mathbf{u}_x$ direction, and the incident magnetic field $\mathbf{H}_i(z)$ is assumed to be linearly polarised in $\mathbf{u}_y$ direction. Figure 2.11 demonstrates such incidence of an EM wave at the boundary of two dielectric half-spaces.

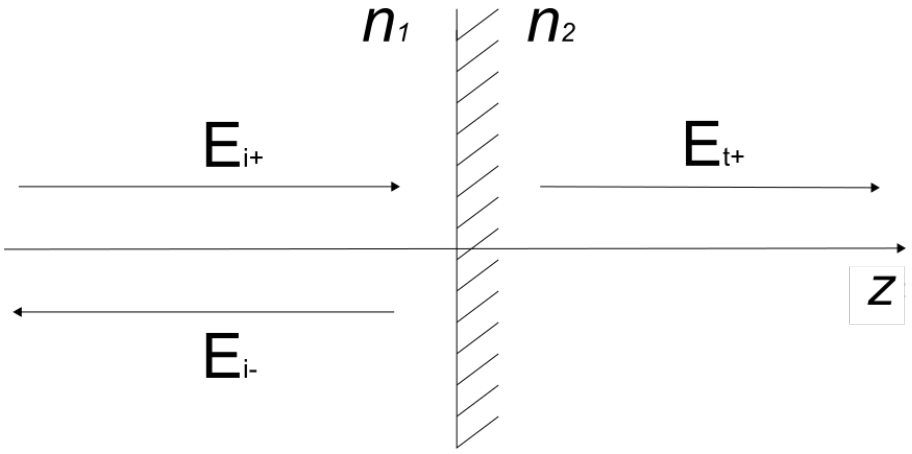

Figure 2.11: Geometry of a plane wave at the boundary of two dielectric half-spaces.

The incident fields can be written as

$$\mathbf{E}_i(z) = \mathbf{u}_x E_{i+} e^{-jk_1 z} + \mathbf{u}_x E_{i-} e^{jk_1 z} \text{ and} \tag{2.8.1a}$$

$$\mathbf{H}_i(z) = \mathbf{u}_y \frac{E_{i+}}{\eta_1} e^{-jk_1 z} - \mathbf{u}_y \frac{E_{i-}}{\eta_1} e^{jk_1 z}, \tag{2.8.1b}$$

where E_{i+} and E_{i-} are the amplitudes of incident electric field and reflected electric field respectively, k_1 is the wavenumber in medium 1, and η_1 is the wave impedance in medium 1. The wave impedance η describes the ratio of the electric and magnetic field amplitudes as

$$\eta = \sqrt{\frac{\mu_0}{\epsilon}}. \tag{2.8.2}$$

The transmitted fields $\mathbf{E}_t$ and $\mathbf{H}_t$ in medium 2 are defined as

$$\mathbf{E}_t(z) = \mathbf{u}_x E_{t+} e^{-jk_2 z} \text{ and} \tag{2.8.3a}$$

$$\mathbf{H}_t(z) = \mathbf{u}_y \frac{E_{t+}}{\eta_2} e^{-jk_2 z}, \tag{2.8.3b}$$

where E_{t+} is the amplitude of the transmitted field, k_2 is the wavenumber in medium 2, and η_2 is the wave impedance in medium 2. The reflection coefficient at the boundary

can be solved from two boundary conditions, wherein the tangential components ($\mathbf{u}_x$ and $\mathbf{u}_y$) of both electric and magnetic fields must be continuous

$$\mathbf{E}_i(0) = \mathbf{E}_t(0) \text{ and} \tag{2.8.4a}$$

$$\mathbf{H}_i(0) = \mathbf{H}_t(0). \tag{2.8.4b}$$

These conditions yield

$$E_{i+} + E_{i-} = E_{t+} \text{ and} \tag{2.8.5a}$$

$$\frac{E_{i+}}{\eta_1} - \frac{E_{i-}}{\eta_1} = \frac{E_{t+}}{\eta_2}. \tag{2.8.5b}$$

Now the reflection coefficient at the boundary R can be solved from (2.8.5) as

$$R = \frac{E_{i-}}{E_{i+}} = \frac{\eta_2 - \eta_1}{\eta_2 + \eta_1} = \frac{\sqrt{\varepsilon_1} - \sqrt{\varepsilon_2}}{\sqrt{\varepsilon_1} + \sqrt{\varepsilon_2}}, \tag{2.8.6}$$

where ε_1 is the relative permittivity in medium 1, and ε_2 is the relative permittivity in medium 2. Similarly the transmission coefficient can be solved from (2.8.5) as

$$T = \frac{E_{t+}}{E_{i+}} = \frac{2\eta_2}{\eta_2 + \eta_1} = \frac{2\sqrt{\varepsilon_1}}{\sqrt{\varepsilon_1} + \sqrt{\varepsilon_2}}. \tag{2.8.7}$$

For oblique incident fields the reflection and transmission coefficients for perpendicular and parallel polarisation at the boundary can be solved in the same manner as above by enforcing Snell's law and assuming that all of the exponential functions are equivalent [36, 40].

2.9 Material measurements

Electrical and magnetic properties of materials affect the propagation of EM waves in a medium. These properties must be known in order to design electrical circuits and electrical components [41]. Physical properties of materials may be determined by measuring permittivity and permeability of the materials. The relative permittivity of biological tissue is assumed to be mostly defined by the water content of the tissue.

2.9.1 Resonator method

The resonator method is a material measurement method were the material under test (MUT) is placed inside the resonator [41]. The MUT inside the resonator will change the loaded quality factor and resonance frequency of the cavity, and therefore, the permittivity of the MUT can be computed, in the case of fully loaded cavity as

$$\mathrm{Re}[\sqrt{\varepsilon_r}] = \frac{f_{r0}}{f_r}, \tag{2.9.1}$$

where ε_r is the complex relative permittivity of the MUT, f_{r0} is the resonant frequency of empty cavity, and f_r is the resonant frequency of fully loaded cavity.

The quality factor of the resonator denotes the under-dampness of the resonator, and it is defined as

$$Q = \frac{2\pi \times \text{ energy stored}}{\text{energy dissipated per cycle}}. \tag{2.9.2}$$

The dissipated energy is inversely proportional to the loaded quality factor, Q_L, and can be resolved into different loss factors as,

$$\frac{1}{Q_L} = \frac{1}{Q_e} + \frac{1}{Q_0} \text{ and} \tag{2.9.3a}$$

$$\frac{1}{Q_0} = \frac{1}{Q_m} + \frac{1}{Q_r} + \frac{1}{Q_d}, \tag{2.9.3b}$$

where Q_e is the external quality factor, and Q_0 is the unloaded quality factor. In addition, Q_m represents the power lost in the metal walls of the resonator, Q_r is the radiation quality factor, and Q_d is the MUT quality factor.

The loaded quality factor can be measured either from reflection measurement or transmission measurement. In both cases the Q_L is computed from the half-power bandwidth B_{-3dB} as

$$Q_L = \frac{f_r}{B_{-3dB}}. \tag{2.9.4}$$

From reflection measurement the unloaded quality factor is calculated from

$$Q_0 \approx \frac{2Q_L}{1+|R|}, \text{ if } Q_e > Q_0 \text{ and} \tag{2.9.5a}$$

$$Q_0 \approx \frac{2Q_L}{1-|R|}, \text{ if } Q_e < Q_0, \tag{2.9.5b}$$

where R is the reflection coefficient. For transmission measurement the Q_0 can be determined from

$$Q_0 \approx \frac{Q_L}{1-|T|}, \tag{2.9.6}$$

where T is the transmission coefficient.

The radiation quality factor may be determined from measuring two similar resonators with different metals. If a closed resonator is used, wherein $Q_r \approx \infty$, the $Q_0 = Q_{m0}$ at the frequency of f_{r0}. The Q_m of a fully loaded resonator is proportional to the square root of the used frequency. Moreover, the quality factor of the MUT is then

$$Q_d = \frac{\varepsilon_r^{'}}{\varepsilon_r^{''}}, \tag{2.9.7}$$

where $\varepsilon_r^{'}$ is the real part and $\varepsilon_r^{''}$ the imaginary part of the relative complex permittivity of the MUT. Correspondingly the imaginary part can be determined as

$$\varepsilon_r^{''} = \varepsilon_r^{'}\left(\frac{1}{Q_0} - \frac{1}{Q_{m0}} - \frac{1}{Q_r}\sqrt{\frac{f_{r0}}{f_r}}\right). \tag{2.9.8}$$

The resonator method for material measurements at millimetre wavelengths is the open quasi-optical resonator. Figure 2.12 illustrates the open quasi-optical resonator. Small ε_r'' is possible to determine with this resonator, since the unloaded quality factor is large ($Q_0 \geq 10^5$) [41].

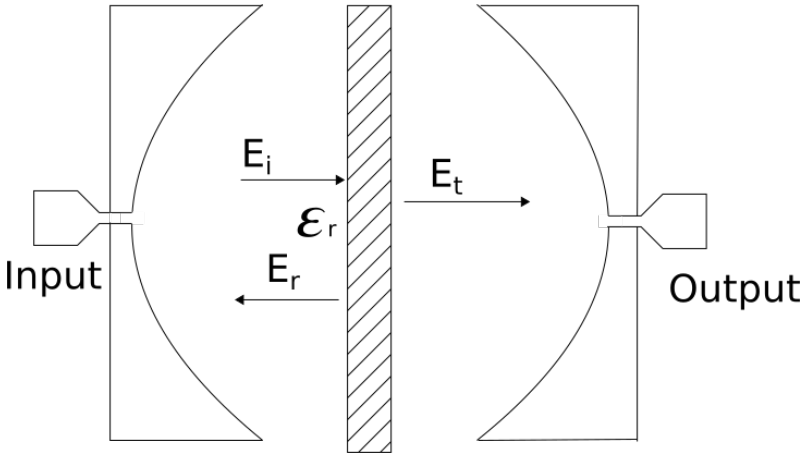

Figure 2.12: The open quasi-optical resonator system in transmission mode. The MUT with permittivity ε_r is placed inside the quasi-optical system. The incident signal $\mathbf{E}_i$ is radiated from Input and the transmission signal $\mathbf{E}_t$ is recorded at Output. In addition, the reflected $\mathbf{E}_r$ is recorded at Input.

2.9.2 Free-space method

A simple method to determine the dielectric properties of the material under test (MUT) is to use the free-space method, wherein the radiated power from one antenna to another is measured. The electrical properties of a MUT may be measured using reflection measurement or transmission measurement. Figure 2.13 shows the two measurement systems. The materials must be large enough so that incident beam covers the sample [42]. The method is suitable for frequencies typically over 5 GHz, so that the diffraction at the boundaries of the MUT is minimal [41].

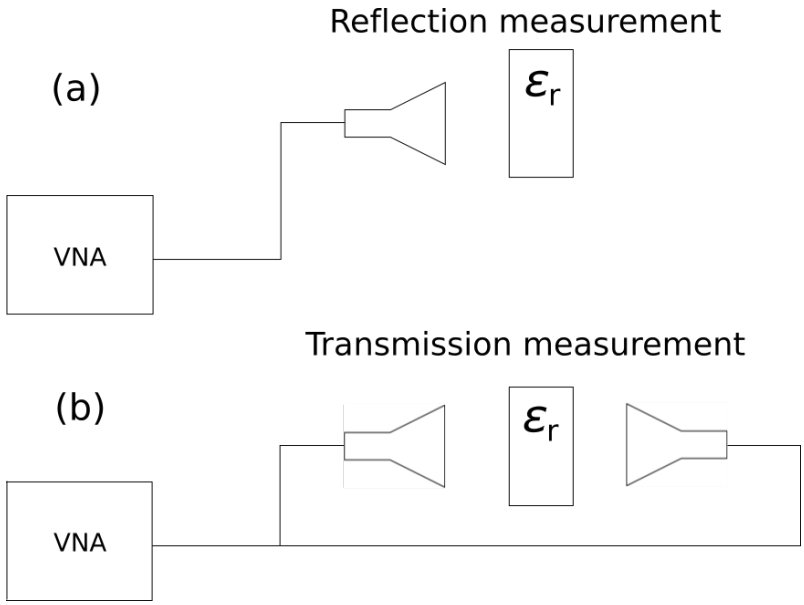

Figure 2.13: The free-space method systems. (a) The reflection measurement and (b) the transmission measurement.

The reflection coefficient for the incident plane wave Γ_r is determined as

$$\Gamma = \frac{(1 - e^{-2jk_r l_r})R}{1 - R^2 e^{-2jk_r l_r}}, \tag{2.9.9}$$

where R is the boundary reflection coefficient defined by (2.8.6), k_r the wavenumber in the MUT defined by (2.7.10), and l_r is the thickness of the MUT. Similarly the transmission coefficient for the plane wave T is determined as

$$T = \frac{(1 - R^2)e^{-jk_r l_r}}{1 - R^2 e^{-2jk_r l_r}}. \tag{2.9.10}$$

At millimetre wavelengths the free-space method often requires a quasi-optical waveguide constructed of mirrors to modify the beam size at the MUT. The quasi-optical system used in the experimental part of this work is presented in Section 3.1.

2.10 Numerical methods

The numerical tool used in this thesis is MATLAB from MathWorks [43]. MATLAB is used to calculate the simulated reflections of human tissue and reference materials used to validate the functionality of the measurement system. In addition, MATLAB is used in signal processing and presenting of the measurement data. The cornea was chosen as the simulated biological structure due to its suitability for *in vivo* millimetre wavelength measurement presented in [7, 31].

2.10.1 Double-Debye model

The water concentration in human tissue is between 20 % to 80 % depending on the type of the tissue [44, 45]. The relevant information measurable of the tissue with millimetre and submillimetre wavelengths is the water concentration, and therefore, the effective permittivity of the tissue structure. The effect of other particles in the cornea, such as, scars or fibres, to the effective permittivity is nearly nonexistent because of their small size (< 50 μm, [7]) relative to the wavelengths used in simulations ($\lambda_0 \geq 900$ μm).

At millimetre and submillimetre wavelengths the dispersive permittivity of water may be modelled with double-Debye method [46]. The model described by Liebe, Huffor, and Manabe, [46], assumes distilled water, and the model is accurate up to 1 THz. The double-Debye model is defined as

$$\varepsilon_w(f, T_w) = \varepsilon_\infty(T_w) + \frac{\varepsilon_\mathrm{s}(T_w) - \varepsilon_{\mathrm{s}2}(T_w)}{1 + jf/f_1} + \frac{\varepsilon_{\mathrm{s}2}(T_w) - \varepsilon_\infty(T_w)}{1 + jf/f_2}, \tag{2.10.1}$$

where $\varepsilon_w(f, T_w)$ is the complex permittivity of water at the frequency f, $\varepsilon_\mathrm{s}(T_w)$ is the permittivity of water at frequency $f = 0$, $\varepsilon_{\mathrm{s}2}(T_w)$ is the first high-frequency constant, $\varepsilon_\infty(T_w)$ is the second high-frequency constant. In addition, f_1 and f_2 are the relaxation frequencies of water. All of these quantities depend on the ambient temperature T_w.

Figure 2.14 illustrates the real and imaginary part of the complex permittivity of distilled water from 200 GHz to 350 GHz and temperature $T_w = 35$ °C computed with (2.10.1). The temperature of 35 °C was chosen since the ambient temperatures of 20-30 °C were reported in [47] to be resulting in temperature of 35 °C in the human cornea. Table 1 displays the approximate parameters used in (2.10.1) to calculate the complex permittivity of distilled water. The permittivity of water is $\varepsilon_w \approx 6 - j7$ at 200 GHz and $\varepsilon_w \approx 5 - j4.5$ at 350 GHz.

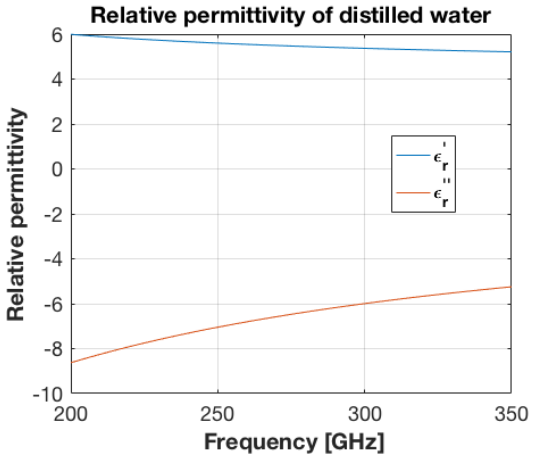

Figure 2.14: The relative permittivity of water calculated with (2.10.1). $\epsilon_r^{'}$ is the real part of the relative permittivity, and $\epsilon_r^{''}$ is the imaginary part of relative permttivity.

Table 1: The parameters used to calculate the relative permittivity response illustrated by Figure 2.14.

Parameter (relative)	Quantity
ε_∞	≈ 3.7189
ε_s	≈ 74.9279
ε_{s2}	≈ 3.7189
f_1	≈ 24.3 GHz
f_2	≈ 967 GHz

The physiological liquid in the human tissues is not pure or distilled water, but rather 0.9 % saline solution. The dispersive response of water changes as ions are added to the medium. The double-Debye model for such liquids at far end of millimetre and submillimetre wavelengths has not been published, to the best knowledge of this author. However, models of seawater permittivity with altering salt concentration at microwave and low end of millimetre wavelengths have been published. A seawater permittivity model proposed by Meissner and Wentz is claimed to be valid up to 90 GHz and temperatures between -2 °C to +29 °C and salinity of 2 parts per thousand (ppt) to 40 ppt [48]. This model is used to further analyse the effect of physiological liquids in the human tissue. The tissue models proposed at millimetre and submillimetre wavelengths assume distilled water and not a physiological solution, to the best knowledge of the author.

The model presented in [48] is an extension of the double-Debye model, where the conductivity of water is added to the double-Debye model. In addition, the salinity concentration, S, changes the relaxation times and adds fitting parameters to the double-Debye model. The seawater model is described as

$$\varepsilon_w(f, T_w) = \varepsilon_\infty(T_w) + \frac{\varepsilon_\mathrm{s}(T_w) - \varepsilon_1(T_w)}{1 + jf/f_1} + \frac{\varepsilon_1(T_w) - \varepsilon_\infty(T_w)}{1 + jf/f_2} - j\frac{\sigma(T_w, S)}{2\pi\varepsilon_0}, \quad (2.10.2)$$

where $\sigma(T_w, S)$ is the conductivity of the seawater, and ε_0 is the permittivity in vacuum. Figure 2.15 shows the complex permittivity of 0.9 % saline solution from 200 GHz to 350 GHz at $T_w = 35$ °C computed with (2.10.2). The permittivity at 200 GHz is $\varepsilon_w \approx 5.5 - j3450$ and at 350 GHz $\varepsilon_w \approx 4.8 - j1940$. The used model does not fit in the limits suggested in [48], and thus, the permittivity values may be erroneous and further research of the saline solution permittivity at millimetre and submillimetre wavelengths is required for an accurate model.

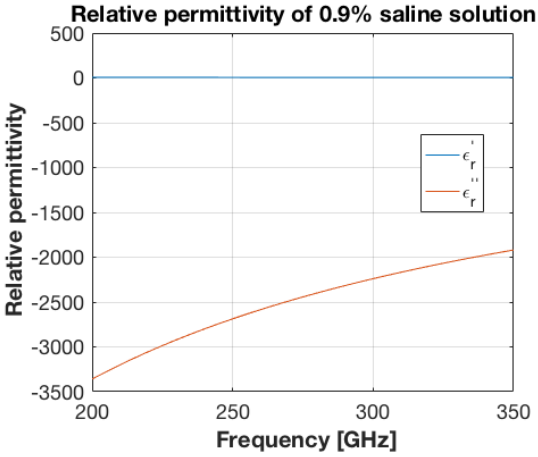

Figure 2.15: The relative permittivity of saline solution calculated with (2.10.2). $\epsilon_r^{'}$ is the real part of the relative permittivity, and $\epsilon_r^{''}$ is the imaginary part of the relative permittivity.

2.10.2 Stratified medium model

A realistic medium is seldom homogenous. If a medium is not homogenous it is considered to be heterogenous or stratified. The electrical properties of a heterogenous medium depend on the location in the medium. In comparison, the electrical properties of a homogeneous medium do not depend on the location in the medium.

The stratified, or multilayer, medium is often modelled by dividing the thickness of the medium to smaller slabs. Each slab is further assumed to have its own absolute permittivity. Figure 2.16 shows a general case stratified structure, wherein the medium has been divided into N dielectric slabs of equal thickness. Moreover, there are $N + 1$ interfaces and $N + 2$ dielectric media due to the bordering half-spaces in front of and behind the stratified structure.

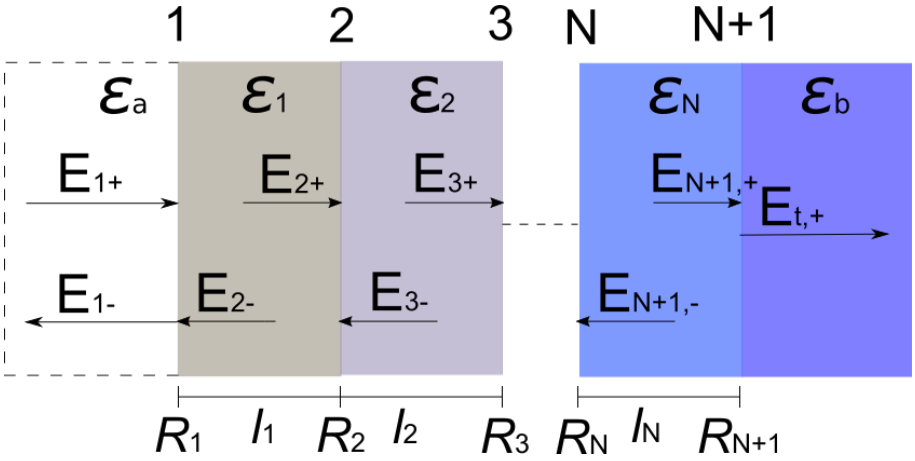

Figure 2.16: A model of stratified medium constructed of N equal length slab. The ε_a and ε_b are absolute permittivities of the bordering half-spaces of the stratified medium.

The absolute permittivity of particular slab can be calculated with several different mixing equations, and in [49] different mixing equations are presented and analysed for different geometries. The stratified structure of the cornea may be calculated with binary-mixture Bruggeman model presented in [50]. The model was first presented by Bruggeman in [51]. The collagen fibre and water of the cornea are thought to be the main factors of the absolute permittivity of the cornea $\varepsilon_{\text{cornea}}$ [7, 29, 31]. In the Bruggeman model for the cornea, such as used in [31], the thickness of the cornea l_{cornea} is divided into N equal length slabs. The relative permittivity of slab i $\varepsilon_{\text{cornea},i}$ may be calculated as

$$p_{w,i}\left(\frac{\varepsilon_{\text{cornea},i}-\varepsilon_w}{2\varepsilon_{\text{cornea},i}+\varepsilon_w}\right)=(p_{w,i}-1)\left(\frac{\varepsilon_{\text{cornea},i}-\varepsilon_{\text{collagen}}}{2\varepsilon_{\text{cornea},i}+\varepsilon_{\text{collagen}}}\right)\ \forall i\in[1,N], \tag{2.10.3}$$

where $p_{w,i}$ is percentile of water in the layer i, $\varepsilon_{\text{collagen}}$ is the frequency independent relative permittivity of collagen fibre, and ε_w is the relative permittivity of water defined by (2.10.1). The collagen fibre and water cannot be volumetrically separated, and thus, $\varepsilon_{\text{cornea},1}=\varepsilon_{\text{collagen}}$ and $\varepsilon_{\text{cornea},N+1}=\varepsilon_w$ [7]. In addition, $p_{w,N}$ denotes the overall corneal tissue water content as $p_{w,N}=\text{CTWC}$.

2.10.3 Reflection from a stratified medium

The reflection from a stratified medium may be described as thin film interference. A thin film interference denotes a phenomenon wherein reflected electromagnetic waves of the upper and lower part of a medium interfere with each other. The thickness of the medium, angle of incidence, and the frequency of the wave result in phase difference between the reflected waves, and thus the overall reflected wave front adds up either constructively or destructively. The rainbow colours seen on a water puddle with a thin oil film is an example of such thin film interference. However, the overall

reflected response from a stratified medium, such as the cornea, cannot be solved as a thin film interference. Fortunately, the overall reflection response may be solved with variety of ways, e.g., by the propagation of the impedances at the interfaces, the propagation of the reflection responses, or the propagation matrices [52].

The overall reflection response $\Gamma_1 = E_{1-}/E_{1+}$ for a homogenous slab may be computed with the propagation of the reflection responses as

$$\Gamma_1 = \frac{R_1 + R_2 e^{-2j\delta}}{1 + R_1 R_2 e^{-2j\delta}}, \tag{2.10.4}$$

where R_1 and R_2 are the reflection coefficients at interfaces 1 and 2 defined by (2.8.6). δ is the effective electrical length of the homogenous slab defined as

$$\delta = k_0 l_r \sqrt{\varepsilon_r}, \tag{2.10.5}$$

where k_0 is the wavenumber in vacuum defined by (2.7.8), l_r is the thickness of the slab, and ε_r is the relative permittivity of the slab.

The overall reflection response Γ_1 may be further generalised for stratified medium by computing the reflection responses recursively starting from the interface $N + 1$ illustrated by Figure 2.16. The recursion reads

$$\Gamma_i = \frac{R_i + \Gamma_{i+1} e^{-2j\delta_i}}{1 + R_i \Gamma_{i+1} e^{-2j\delta_i}}, \; i = N, N-1, .., 1, \tag{2.10.6}$$

where Γ_i is the reflection response of slab i, R_i is the reflection coefficient at interfaces i, δ_i is the effective electrical length of slab i, and Γ_{i+1} is the reflection response of slab $i + 1$. The recursion is initialised by $\Gamma_{N+1} = R_{N+1}$, since no backward propagating wave is assumed from medium $N + 2$.

2.10.4 Simulated reflection response of human tissue

The simulated overall reflection response Γ_1 of cornea was computed for 300 CCT values ranging from 400 μm to 700 μm and 300 CTWC values ranging from 0.77 to 0.79. Moreover, two different media were considered: one homogenous layer and a heterogenous layer. The thickness of the homogenous layer was defined as $l_r = \text{CCT}$ and the relative permittivity of the layer was computed with $p_{w,1} = \text{CTWC}$.

The heterogenous layer was divided into $N = 70$ equal thick slabs as

$$\sum_{i=1}^{N} l_i = \text{CCT}. \tag{2.10.7}$$

The relative permittivity of each slab was computed with (2.10.3) such that the water fraction part $p_{w,1} = 0$ and $p_{w,N} = \text{CTWC}$.

The simulation was computed with two frequencies 220 GHz and 320 GHz. The atmospheric attenuation is relatively low between 220 - 320 GHz. Figure 2.17 presents the atmospheric attenuation of air from 100 GHz to 500 GHz.

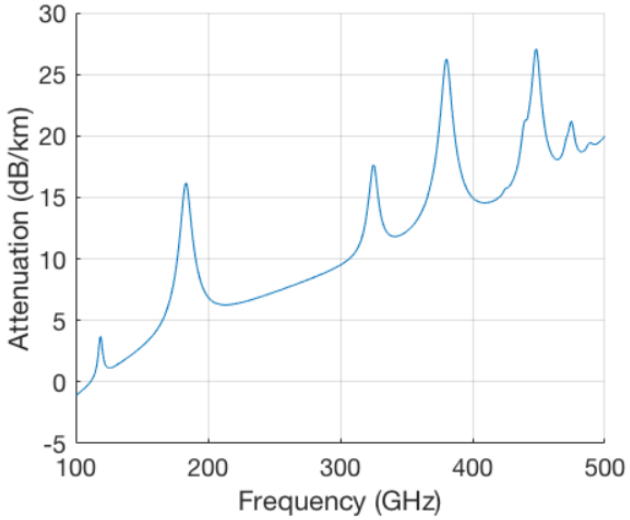

Figure 2.17: Atmospheric attenuation between 100 - 500 GHz. A broad transmission window centred at 260 GHz is visible. Figure created according to ITU-R Recommendations ITU-R P.676-9.

Furthermore, scattering from rough surfaces might cause problems with the measurements. If the surface roughness of the target is close to the wavelength of the incident wave, i.e., the surface is not smooth relative to the incident signal, the object loses its specularity. The typical features of human tissue range from 100's of μm to 1 mm [53]. Therefore, lower frequencies provide less scattering of the reflected signal.

For imaging systems, such as presented in [7], the chosen frequency range has to be a compromise between the hydration sensitivity, scattering, and spatial resolution. As concluded above the lower frequencies are better for minimising scattering and maximising hydration sensitivity. However, the spatial resolution improves with the higher frequencies due to the smaller beam waist radius of the incident beam.

Figure 2.18 presents the simulated amplitude and phase responses of the reflection coefficient computed with (2.10.6) for each CCT and CTWC value. The tissue in this case is assumed to be a homogenous layer consisting of collagen fibre and distilled water. The permittivity of water is computed with (2.10.1).

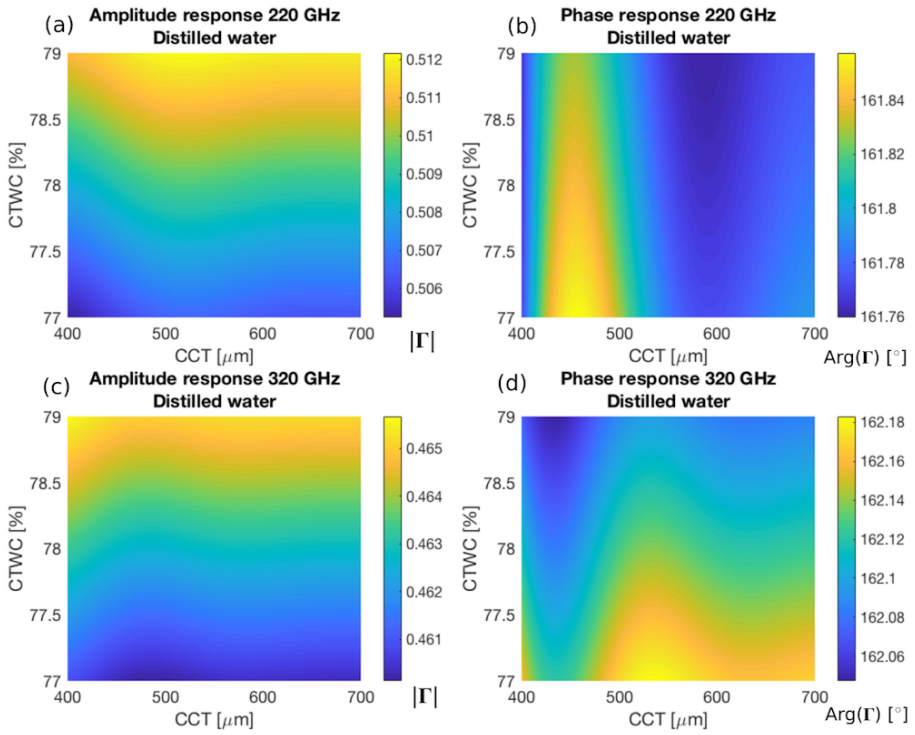

Figure 2.18: Simulated reflection coefficients of cornea model with one homogeneous layer and distilled water at 220 GHz and 320 GHz. (a) Amplitude response of the reflection coefficient at 220GHz, (b) phase response of the reflection coefficient at 220 GHz, (c) amplitude response of the reflection coefficient at 320 GHz, and (d) phase response of the reflection coefficient at 320 GHz.

The amplitude responses at 220 GHz in Figure 2.18 (a) indicate that higher CTWC values result in stronger reflection. The difference between the amplitudes is about 0.6 % or less when the CTWC value changes from 77 % to 79 %. The phase responses at 220 GHz in Figure 2.18 (b) present a difference of 0.09 degrees or less. The amplitude responses at 320 GHz in Figure 2.18 (c) indicate also that higher CTWC values result in stronger reflection. However, the difference in the amplitudes at 320 GHz is less than at 220 GHz, about 0.5 % or less when the CTWC value changes from 77 % to 79 %. The phase responses in Figure 2.18 (d) indicate larger variation of the phase response, about 0.12 degrees or less, when the CTWC value changes from 77 % to 79 %.

Figure 2.19 presents the amplitude and phase responses at 220 GHz and 320 GHz simulated with the stratified media model. The layer is assumed to be consisting of 70 layers homogenous media with increasing water fraction part towards the aqueous humour.

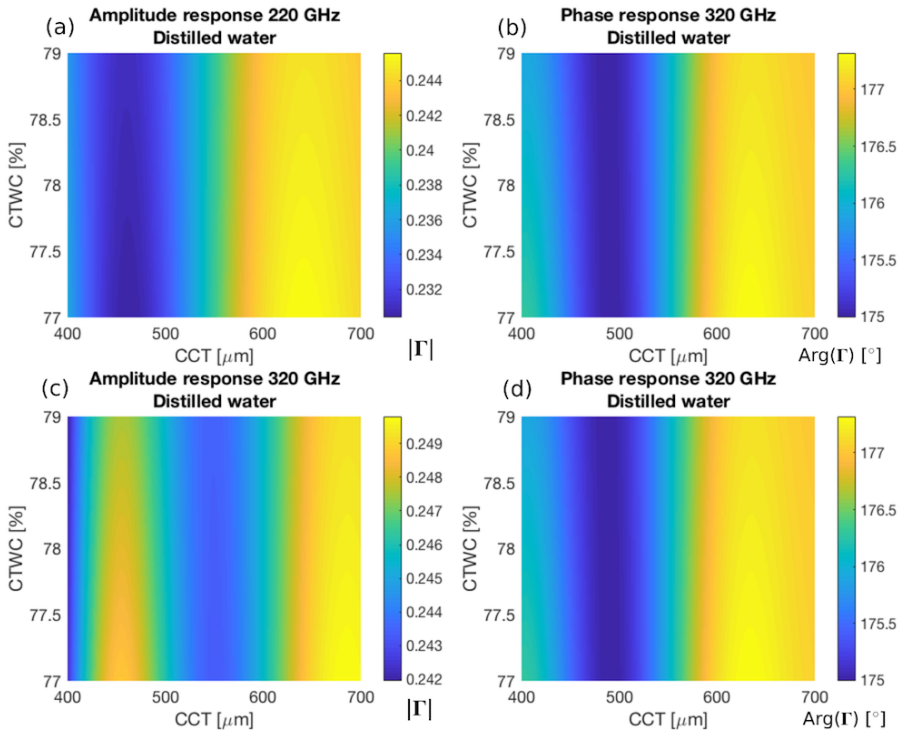

Figure 2.19: Simulated reflection coefficients of cornea model with 70 layers and distilled water at 220 GHz and 320 GHz. (a) Amplitude response of the reflection coefficient at 220GHz, (b) phase response of the reflection coefficient at 220 GHz, (c) amplitude response of the reflection coefficient at 320 GHz, and (d) phase response of the reflection coefficient at 320 GHz.

The reflection coefficients with stratified media model results in different amplitude and reflection responses. The reason might be that the first layer $i = 1$ is assumed to be dry, i.e., $p_{w,1} = 0$. This assumption is unphysical even if only a small part of the model is assumed to be dry. The reflection from the first layer might the reason why the amplitude and phase responses are different. The results suggest that higher CTWC values would not result in stronger reflection.

Figure 2.20 illustrates the amplitude and phase responses at 220 GHz and 320 GHz simulated with one homogenous layer. The layer is assumed to be consisting of collagen fibre and 0.9 % saline solution. The saline solution permittivity is calculated with (2.10.2).

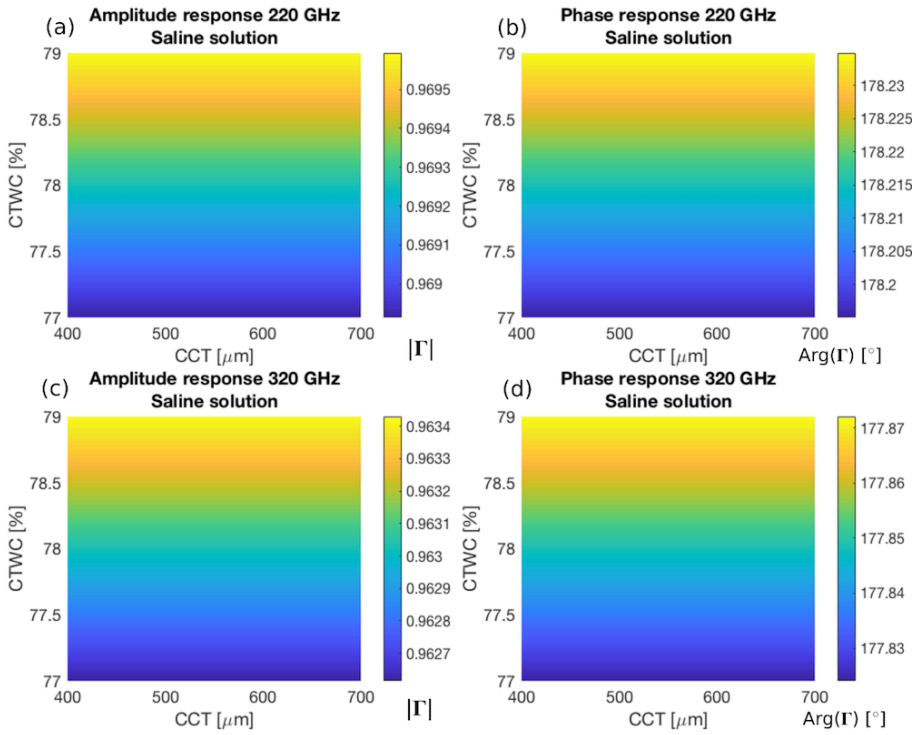

Figure 2.20: Simulated reflection coefficients of cornea model with one homogenous layer and saline solution at 220 GHz and 320 GHz. (a) Amplitude response of the reflection coefficient at 220GHz, (b) phase response of the reflection coefficient at 220 GHz, (c) amplitude response of the reflection coefficient at 320 GHz, and (d) phase response of the reflection coefficient at 320 GHz.

The amplitude and phase responses of both frequencies present almost identical images. The reason is might be the permittivity model used to compute the saline solution permittivity. However, the amplitude responses of both frequencies indicate that higher CTWC value results in stronger reflection. At 220 GHz the difference in the amplitude responses is 0.05 % when the CTWC value changes from 77 % to 79 %, likewise at 320 GHz the amplitude changes 0.07 % when the CTWC value changes from 77 % to 79 %.

Figure 2.21 presents the amplitude and phase responses of the reflection coefficient at 220 GHz and 320 GHz computed with the stratified media model. The layer is assumed to be consisting of 70 layers homogenous media with increasing water fraction part towards the aqueous humour.

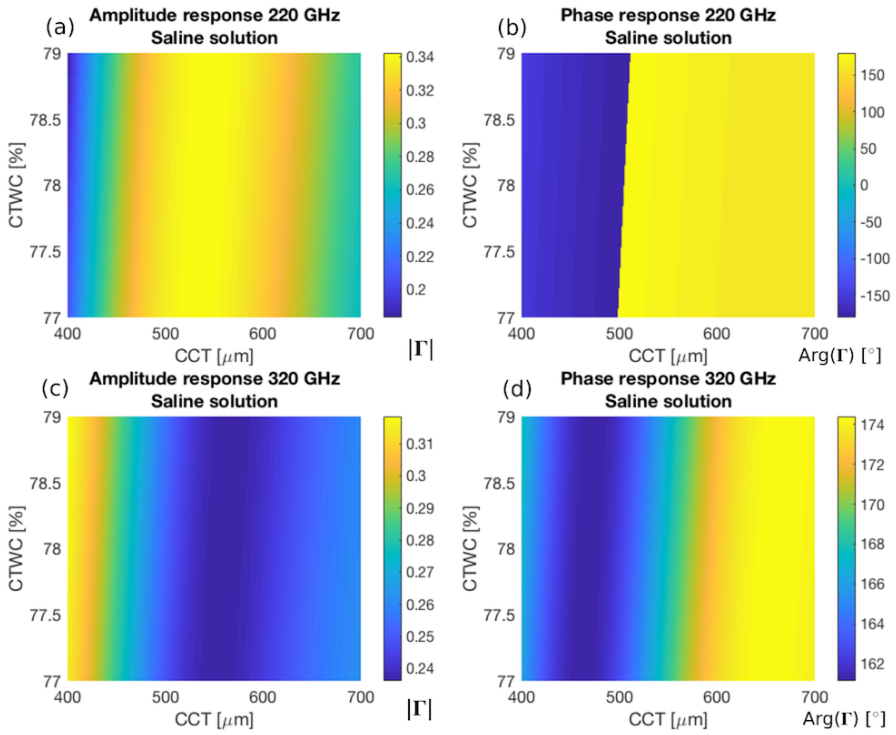

Figure 2.21: Simulated reflection coefficients of cornea model with 70 layers and saline solution at 220 GHz and 320 GHz. (a) Amplitude response of the reflection coefficient at 220GHz, (b) phase response of the reflection coefficient at 220 GHz, (c) amplitude response of the reflection coefficient at 320 GHz, and (d) phase response of the reflection coefficient at 320 GHz.

Figure 2.21 indicate similar results as those in Figure 2.19, wherein the higher CTWC value does not result in stronger reflection. The reason might be again because of the assumed dry layer. More accurate stratified media models the lower and higher CTWC of the cornea model should be determined.

3 Measurement system and measurements

3.1 Quasi-optics

Quasi-optical system can be designed for large frequency bands or single frequency systems. The designed systems can be simple with few quasi-optical components or more complex systems with multiple lenses, mirrors, resonant grids, and frequency-selective surfaces to name a few. The quasi-optical system design begins by determining the architecture and quasi-optical components. The component requirements are followed by the selection of the source of the Gaussian beam, which determines the beam waist radius ω_0 of the radiated beam. In addition, components are selected by the critical beam waist radii at the quasi-optical components. The design procedure is then followed by developing the quasi-optical configuration. In addition, calculating the losses and coupling trough the system is critical before implementing the designed system.

3.1.1 Gaussian beam

In quasi-optical systems the propagating wavefront is described as a Gaussian beam. The Gaussian beam is an effective tool for designing a quasi-optical system. A Gaussian beam is often produced by a corrugated horn antenna, from which 98 % of the power radiated is of the first mode of the Gaussian beam [54].

The corrugated horn radiates a Gaussian beam with a beam waist radius ω_0. As the beam propagates the beam radius changes as

$$\omega(z) = \omega_0 \sqrt{1 + (\frac{\lambda_0 z}{\pi \omega_0^2})^2}, \tag{3.1.1}$$

where λ_0 is wavelength of the wave in vacuum, and z is the propagation distance of the wave from the phase centre of the radiating element, e.g., corrugated horn antenna. Figure 3.1 illustrates the equiphase surfaces of the propagating Gaussian beam.

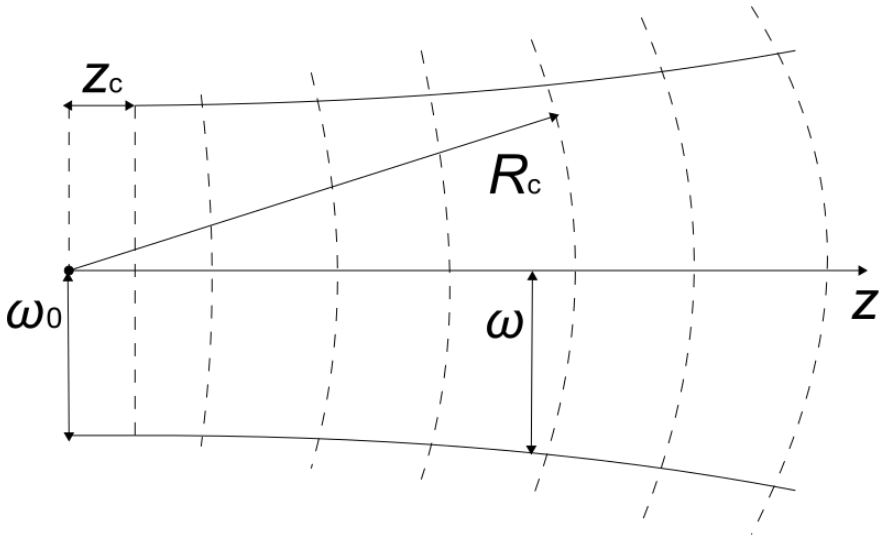

Figure 3.1: Representation of a Gaussian beam propagation. The dashed lines represents the equiphase surfaces, ω_0 is the beam waist radius at $z = 0$, ω is the beam radius, R_c is the radius of curvature, and z_c is the confocal distance.

The radius of curvature of the propagating beam R_c changes as the beam propagates:

$$R_c(z) = z[1 + (\frac{\pi\omega_0^2}{\lambda_0 z})^2]. \tag{3.1.2}$$

Following from (3.1.2) at the origin of the beam $R_c(0) = \infty$ and the wave front is planar. This leads to defining the minimum radius of curvature, which is called the confocal distance as in [55] or Rayleigh range as in [56]. The confocal distance z_c is defined as

$$z_c = \frac{\pi\omega_0^2}{\lambda_0}. \tag{3.1.3}$$

3.1.2 Dual-mode horn

Horn antennas are used as sources of Gaussian beams as discussed above. The best choice is a corrugated horn [54,55]. Other good sources for Gaussian beams are Potter, diagonal, pyramidical, and conical. Also several integrated antennas are possible to implement as source of Gaussian beams [54]. In this thesis a modified dual-mode Potter horn antenna, i.e., Pickett-Potter horn, is used and the antenna is introduced in [57]. The main advantage of the Pickett-Potter horn is its simple construction. Another advantage is its nearly as efficient radiation at the fundamental Gaussian beam mode as that of a corrugated horn [55]. Main disadvantage of a dual-mode horn is its smaller bandwidth compared with a corrugated horn [54], about 10 % from the centre frequency. Figure 3.2 presents a dual mode horn structure.

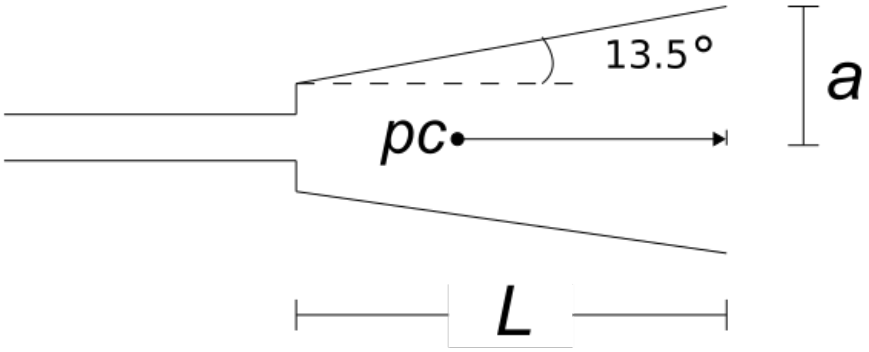

Figure 3.2: The design structure of Pickett-Potter horn antenna. *pc* is the phase centre of the horn, L is the length of the horn, and a is the aperture radius of the horn.

The aperture radius a illustrated in Figure 3.2 is specified as

$$a \approx 3.2\lambda_{\text{centre}}, \tag{3.1.4}$$

where λ_{centre} is the centre wavelength radiated from the antenna. Length of the horn L is specified as

$$L \approx 10.62\lambda_{\text{centre}}. \tag{3.1.5}$$

In addition, the distance of the phase centre *pc* from the aperture is specified at centre frequency as in [57] as

$$pc \approx 6.46\lambda_{\text{centre}}. \tag{3.1.6}$$

The beam waist radius ω_0 at *pc* for a Pickett-Potter or other dual-mode antennas is specified as in [55, 58]

$$\omega_0 \approx 0.59033a, \tag{3.1.7}$$

where a is the horn radius. The equal waist position z_A is specified as in [56, 58]

$$z_A \approx L\sin^2(\Phi_A), \tag{3.1.8}$$

where Φ_A is given by

$$\Phi_A \approx \tan^{-1}(\frac{\pi\omega_0^2}{\lambda L}). \tag{3.1.9}$$

The taper angle of the Pickett-Potter is normally $\theta_0 = 13.5°$ for a optimal beam-width [54, 59]. In addition, it is worth noting that the equal waist position z_A differs from the phase centre, *pc*, slightly [58].

The phase centre *pc* changes as the radiated frequency changes, and thus, the Pickett-Potter horn may only be used with small bandwidths. If the *pc* is assumed to be linearly changing from 220 - 330 GHz the difference would approximately 49.90 mm. This would mean that *pc* is behind the horn horn at 330 GHz ($L = 11.7$ mm). However, Equation (3.1.6) is only valid at the centre frequency of the horn, and thus, more study on how *pc* changes as function of the used frequency is needed.

3.1.3 Reflectors

Traditional waveguides are generally considered too lossy for millimetre waves [54]. In quasi-optical systems the technique to focus and shape the beam is called beam waveguides [1]. The beam waveguides are composed of different quasi-optical components. Lenses, mirrors, dielectric film, different interferometers, and frequency selective films and discs are some quasi-optical components used in beam waveguides [54]. Mirrors are usually used in off-axis (OAP) configuration, where the reflector is placed at an angle to the propagation axis.

The Gaussian beam can be focused on a point with a parabolic or ellipsoid mirror [60]. In the millimetre wavelength region the absorption of the mirrors is only about 0.1 % [54]. The antenna phase centre defines the radiating point of the Gaussian beam. The distance where the mirror should be placed depends on the effective local length of the mirror [55]. The distance from the antenna phase centre to the mirror must be almost the same as the effective focal length of the reflector [55, 58]. The beam starting point z_A can be calculated from (3.1.8).

There are some problems that arise from using mirrors. First problem is that the reflectors are not thin, and thus the beam is distorted by the different lengths to the surface of the mirror. In addition, the intensity changes as the beam propagates and thus will distort the signal. Lastly the reflectors cause cross-polarisation to the signal. With two mirror system the cross-polarisation and amplitude distortion can be sufficiently compensated [54].

Two OAP mirrors form a waveguide that transforms a beam waist radius, ω_{in}, at the focal point of the first OAP to a beam waist radius, ω_{out} at the focal point of the second OAP. The magnification, $\mathbf{M}$, of the beam waist radius is defined as in [61] as

$$\mathbf{M} = \frac{fl_{\text{in}}}{fl_{\text{out}}}, \tag{3.1.10}$$

where fl_{in} is the effective focal length of the first mirror, and fl_{out} is the effective focal length of the second mirror.

The quasi-optical components, such as the OAP mirror, is chosen such that the power that spills over the component is negligible. The phenomenon is known as edge taper T_E, and it is specified as the ratio between the diameter of the component D_m and the beam waist radius of the incident beam at the component ω

$$\frac{D_m}{\omega} = \sqrt{2ln(T_E)}. \tag{3.1.11}$$

The power that is lost is then $1/T_E$. Generally the diameter is chosen to be 4ω ($T_E \approx 0.034$ %) to ensure almost 100 % transmission from the mirror, however, in some systems diameter of $D_m = 3\omega$ is sufficient ($T_E \approx 1.11$ %) [54].

3.2 Measurement setup

The measurements were done with a Keysight N5225A Performance Network Analyzer (PNA) [62] and a Virginia Diodes Vector Network Analyzer Extension Module (VNAX) [63] as the signal generator. The radiation source used was a Radiometer Physics Pickett-Potter Dual Mode horn antenna for frequency range 220 - 325 GHz [64]. The used reflectors were from Edmund Optics [65] and the building blocks as well as the optical breadboards were from Thorlabs [66].

The millimetre extension module and the horn system was placed on an optical table. The quasi-optical waveguide (QOW) was built also on the optical table. The first OAP had a diameter of 76.2 mm and focal length of 76.2 mm [65]. The horn antenna was placed a little less than the focal length away from the first mirror. The second mirror of the waveguide was placed 28 cm away from the first mirror and the mirror was turned 90° in order to direct the beam downwards. The second mirror had a diameter of 76.2 mm and focal length of 152.4 mm. Figure 3.3 shows the waveguide and horn antenna on the optical table.

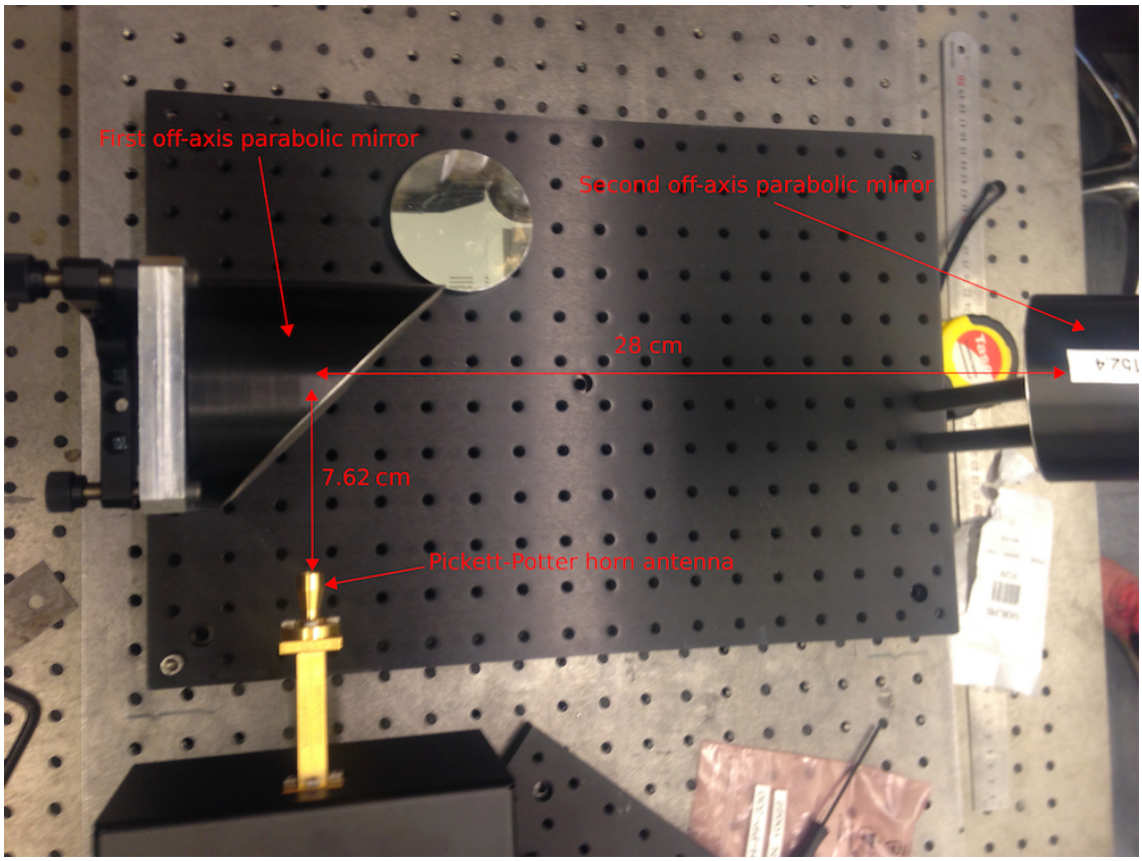

Figure 3.3: The horn antenna in front of the quasi-optical waveguide.

The distance between the horn and the first reflector was mechanically measured. The flat reflector presented by Figure 3.4 was placed 152.4 mm from the second

mirror and the horn was moved towards the first mirror mechanically. The peak maximum amplitude was then observed and thus the optimal distance was found for the horn and the first mirror. However, the distance of maximum reflection changes since the phase centre *pc* changes as the frequency of the wavefront changes, and thus, the determination of exact distances is ambiguous. Figure 3.4 shows the feed horn, QOW, translational stage and a flat reflector as the whole measurement system.

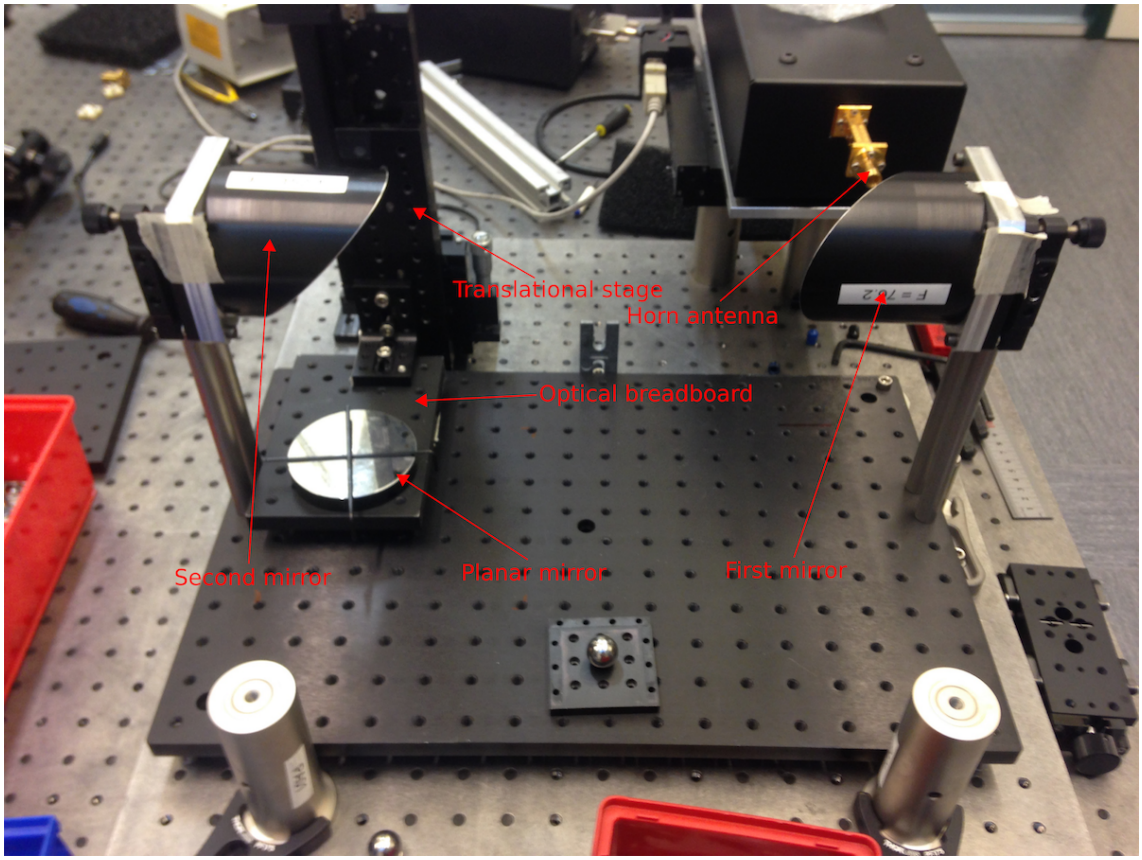

Figure 3.4: The final built far end of the measurement setup.

3.2.1 Technical summary

The used equipment, their specifications, and distances between the equipment are summarised in Table 2. The distances are specified for flat reflector measurement.

Table 2: The dimensions of the reflectors, distances d_1 and d_2, and minimum beam waist radii ω_{01} and ω_{02} of the reflectors.

Mirror	M_1	M_2
Focal length	76.2 mm	152.4 mm
Diameter	76.2 mm	76.2 mm
d_1	76.2 mm	-
d_2	-	152.4 mm
ω_{01}	2.268 mm	-
ω_{02}	-	4.536 mm

Table 2 denotes the focal lengths of the waveguide mirrors as well as their diameters. d_1 indicates the distance where the phase centre point of the horn antenna is placed from the centre of the first OAP. d_2 indicates the distance where the flat reflector is placed from the centre of the second OAP. The beam waist radii, ω_{01} and ω_{02}, are the beam waist radii the beam has at the focal points of each mirror.

The beam waist radius $\omega_0 \approx 2.27$ mm of the Gaussian beam calculated from (3.1.7) for a Pickett-Potter horn antenna at 272.5 GHz. The equivalent waist position z_A, i.e., the position where the beam is expected to radiate, calculated from (3.1.8) is 7.15 mm from the edge of the aperture. The difference between z_A and the phase centre point $p_c \approx 37.61$ μm, meaning that the radiation position is almost the same as the phase centre.

3.3 Materials under test

3.3.1 Planar mirror

The first material under test (MUT) measured was a planar reflector. The primary idea behind the planar reflector (or rather planar mirror) measurement was to determine the overall functionality of the setup, i.e., to see that the measured amplitude was actually measured from the MUT through the quasi-optical waveguide (QOW). Figure 3.5 shows the planar mirror used in the measurements. The first processed results of the mirror measurement indicated that there was aliasing in the system. Aliasing and how it was managed is described in Chapter 4 in detail.

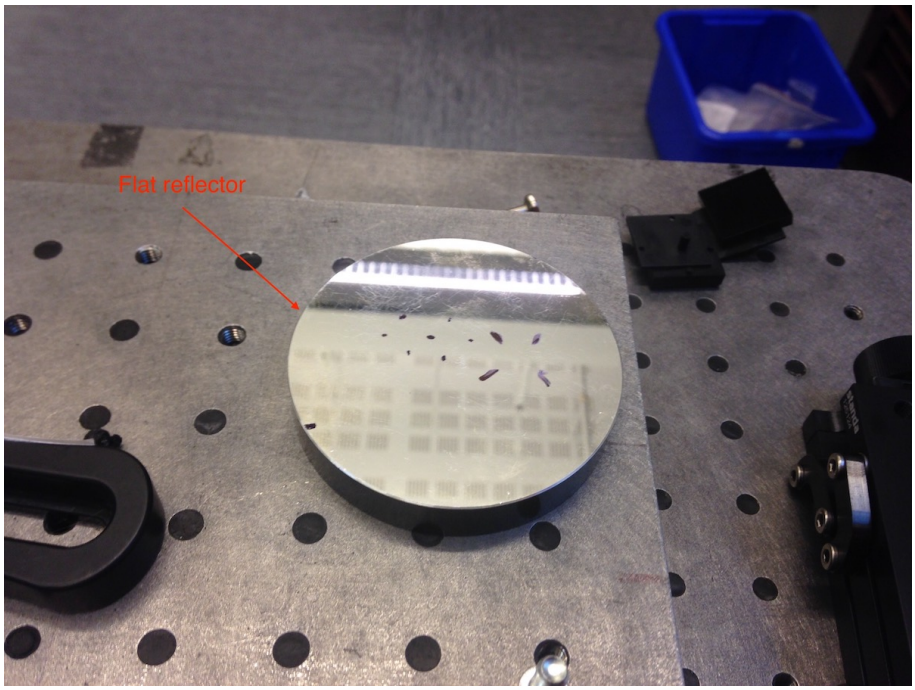

Figure 3.5: The measured flat reflector.

3.3.2 Cyclic-olefin copolymer

A Cyclic-olefin copolymer (COC) piece of 6 cm wide, 6 cm long from TOPAS Advanced Polymers was measured on an absorber [67]. The average thickness of 1.98 mm was measured with a dial thickness gauge from Käfer [68] . The COC piece was placed at the reference plane specified by the planar mirror. Beneath the piece was a few centimetre air gap and a piece of radar absorbing material (RAM). A RAM has low reflectivity and thus the reflections could be considered to be caused only by the material under test (MUT). Figure 3.6 shows the measured COC piece.

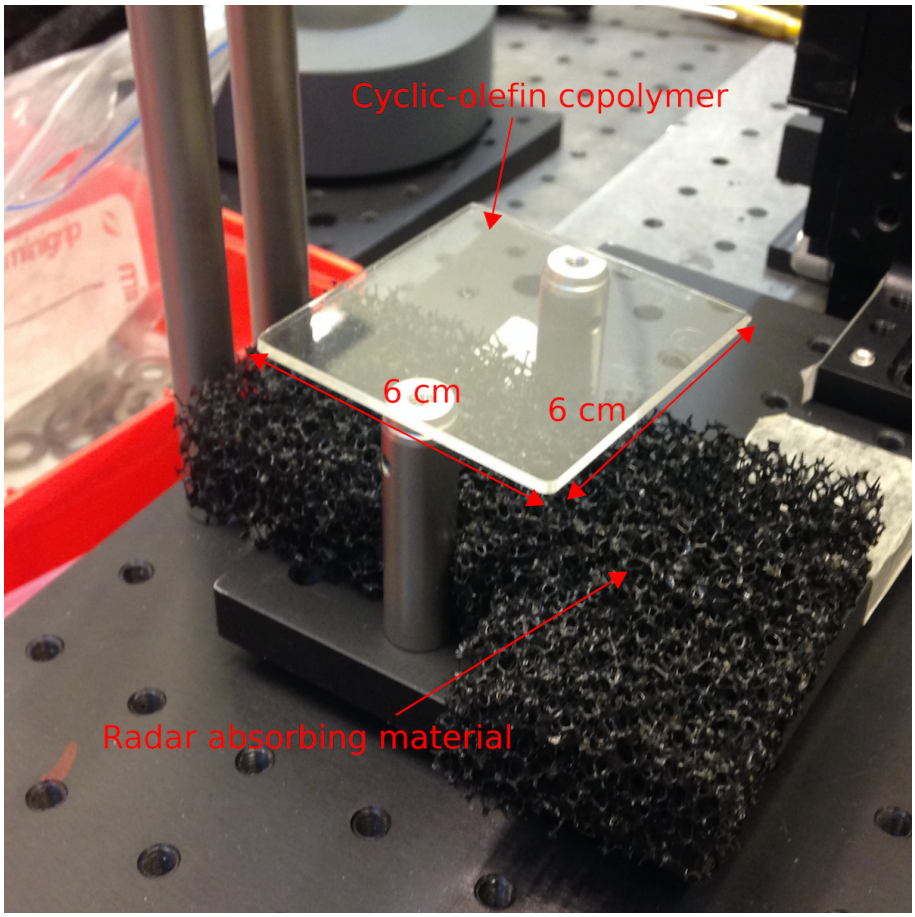

Figure 3.6: The measured TOPAS Cyclic-olefin copolymer (COC) piece on radar absorbing material (RAM).

3.3.3 Silicon

The next material measured was a 1.5 cm wide and 2.5 cm long piece of silicon. The thickness of the piece was measured with a dial thickness gauge from Käfer [68]. The average thickness of the piece was measured to be 510 μm. Figure 3.7 shows the silicon piece now referred to as the smaller piece of silicon. In addition, another piece of silicon with a diameter of 10 cm and slightly different thickness was measured. The thickness of the piece was measured with the same dial thickness gauge and the value measured was 540 μm. Figure 3.8 shows the other piece of silicon in the measurement system, now referred to as the larger piece of silicon.

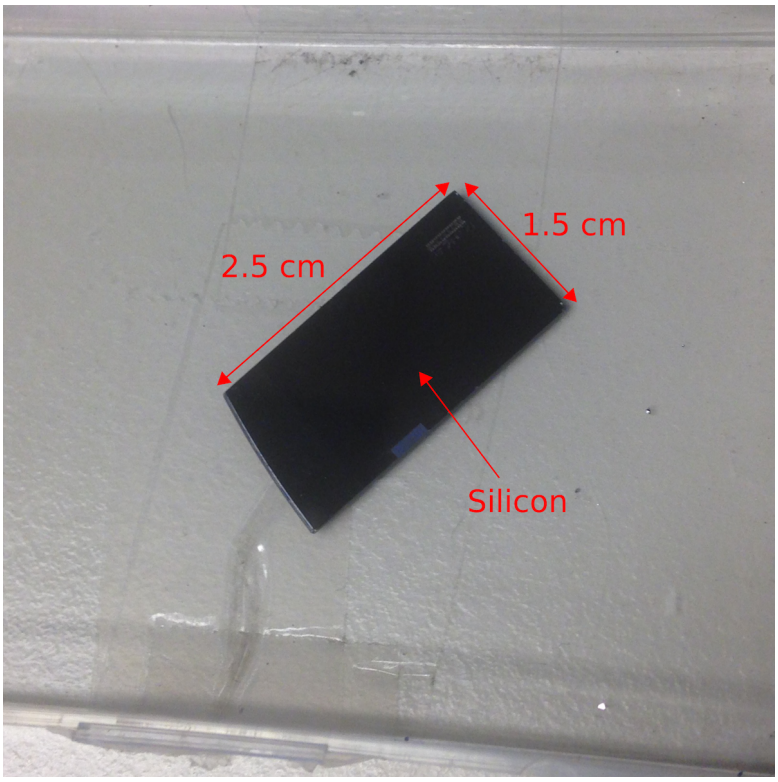

Figure 3.7: The measured smaller piece of silicon (510 μm).

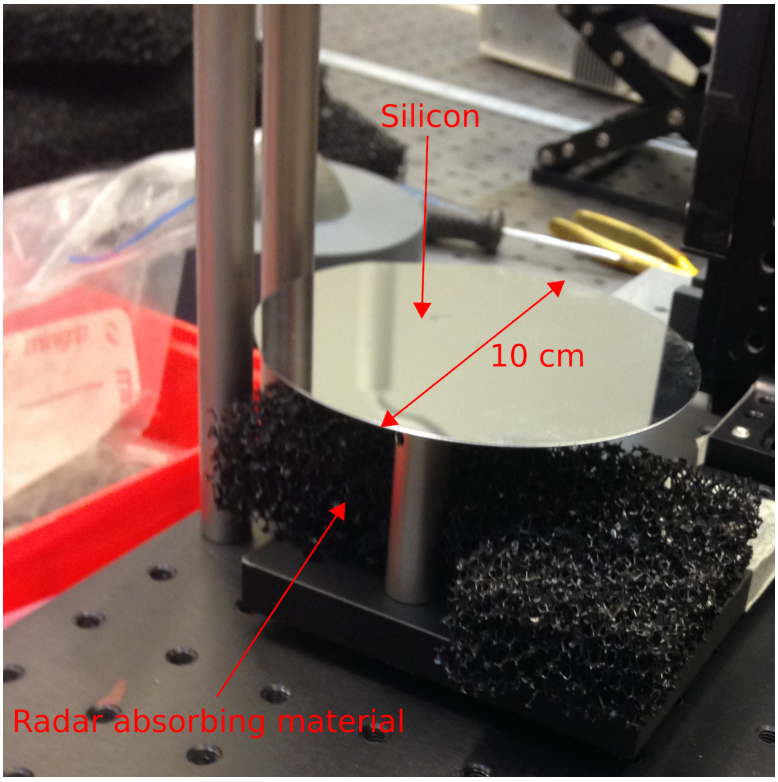

Figure 3.8: The measured larger piece of silicon (540 μm).

3.3.4 Polytetrafluoroethylene

A 8 cm wide 10 cm long piece of polytetrafluoroethylene (PTFE) was also measured. The thickness of the piece was measured with the same dial thickness gauge from Käfer, and the average measured value was 2.89 mm. Figure 3.9 shows the measured piece of PTFE at the measurement situation.

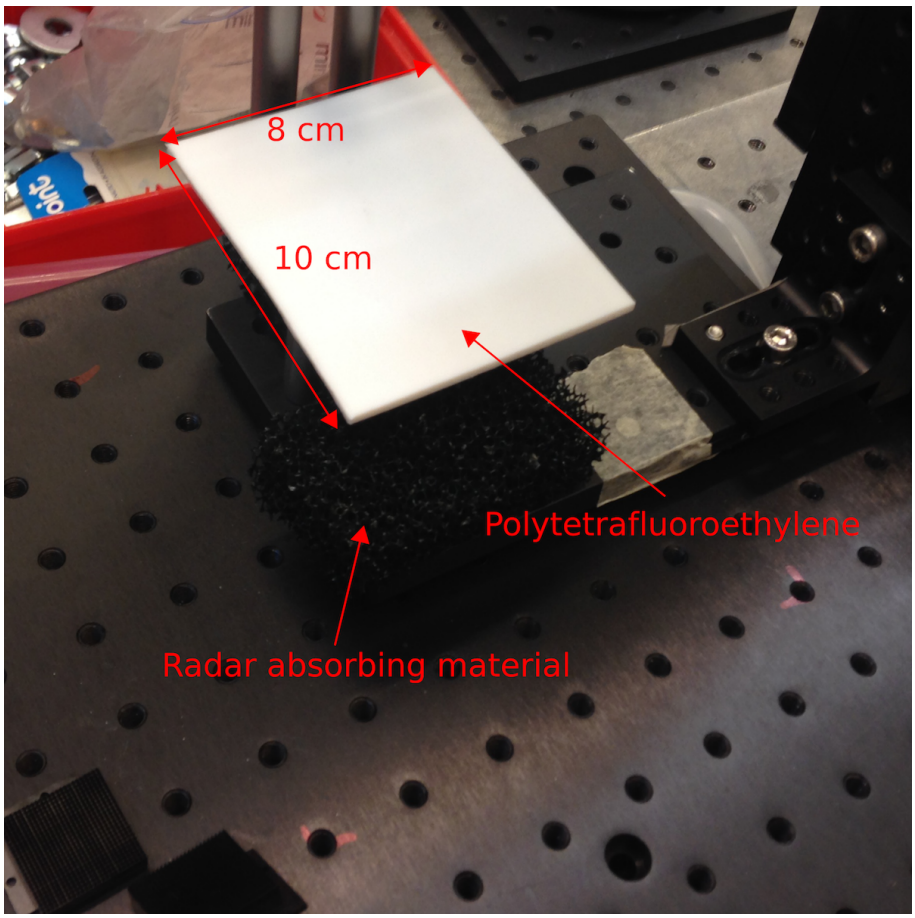

Figure 3.9: The measured piece of PTFE in the measurement setup.

3.3.5 Steel ball

The first curved MUTs measured were two steel balls acquired from Tampereen Laakerikeskus Oy [69]. The measured steel balls had radii of 8.5 mm and 8.73 mm which corresponding to the radius of curvature of human cornea $R_{\text{cornea}} \approx 7.8..8$ mm [70]. Figure 3.10 shows the measured steel balls.

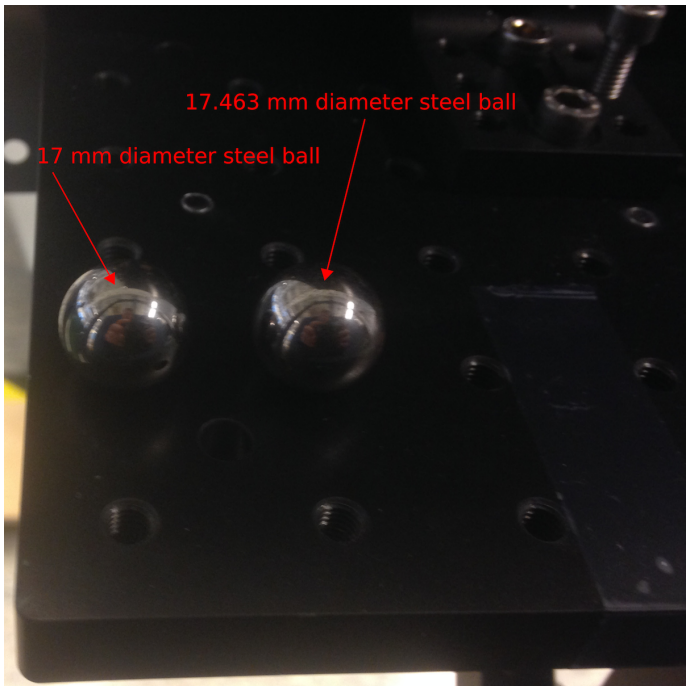

Figure 3.10: The measured steel balls.

3.3.6 Contact lens

10 +6 diopter Acuvue Moist contact lenses were acquired from Coopervision to be used as human tissue phantoms [71]. The reported central thickness of the lenses where reported to be 350 μm. The material the contact lens consisted of was etafilcon A. The material is a hydrogel consisting of 2-hydroxy-ethyl methacrylate, hydrophilic monomers and methacrylic acid. The refractive index at optical wavelengths of the lenses were 1.387. The water content of the lenses were 62 %. Figure 3.11 shows the contact lenses measured in this work.

Figure 3.11: The measured contact lenses in their packing.

3.3.7 Model eye

An eye model was built so that the contact lens could be measured with more realistic configuration. The built model had a base cavity and an upper lock. The base cavity was 28.80 mm long and had a diameter of 8.40 mm. In addition, three pipelines were attached to the base cavity, two for the filling the cavity with liquid and one for removing liquid from the top of the model if it would leak. The upper lock was 15.50 mm long and the inner diameter at the bottom of the lock was 14 mm and the inner diameter at the top of the lock was 9.9 mm. Figure 3.12 shows the built model eye.

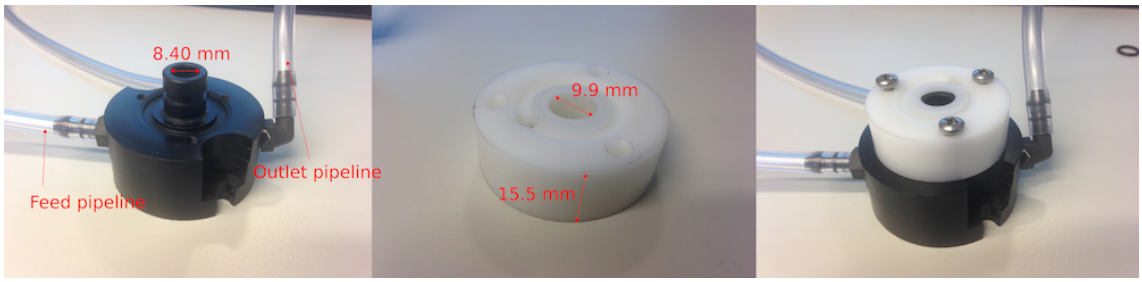

Figure 3.12: The built model eye. (Left) the base cavity, (Middle) the upper lock, and (Right) the model eye.

3.3.8 Cling film

The first material placed in the model eye was cling film with brand name Eskimo Elmukelmu from Eskimo Finland [72]. The cling film was low-density polyethylene based material and the approximate thickness was 30 μm. A piece of the cling film was cut from the roll and placed in the eye model. Figure 3.13 presents the cling film in the eye model.

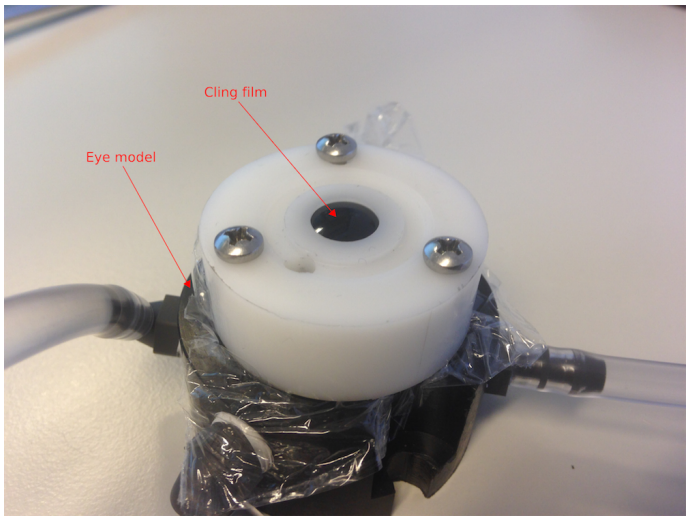

Figure 3.13: The cling film in the eye model with saline solution inside the cavity of the eye model.

3.4 Spherical structure

The cornea has a radius of curvature of $R_{\text{cornea}} \approx 7.5\text{-}8$ mm [70]. The structure of the cornea is very ordered and may be presented as a homogenous model at submillimetre wavelengths [7]. Therefore, the cornea structure is well-defined curved etalon, i.e., the structure can be considered to be a curved thin film [73].

The difference of the curved MUT and the flat MUT arise from the phase difference at the surface of the MUTs. For the flat MUT the beam is considered to have the maximum reflection at the focal point of the OAP mirror. However, the maximum reflection of a curved MUT is considered to be at the point where the radius of curvature of the beam R_c and the radius of curvature of the MUT R_{MUT} coincide.

Figure 3.14 illustrates the simulated R_c from 7.3 cm and 6.8 cm from the focal plane as well as the radii of both steel balls used as MUTs. The efficiency of the phase difference $\eta_{\text{curvature}}$ is calculated as

$$\eta_{\text{curvature}} = \int_S e^{jk_0(z_{0,\text{steel ball}}(x) - z_{1,\text{steel ball}}(x))} dS, \tag{3.4.1}$$

where k_0 is the wavenumber of the propagating wave, and $z_{0,\text{steel ball}}$ is the height of the curvature at line S specified as

$$z_{0,\text{steel ball}}(x) = \sqrt{R^2_{\text{steel ball}} - x^2}, \tag{3.4.2}$$

where $R_{\text{steel ball}}$ is the radius of the steel ball, and x is the point on the line S in the limits $-\omega(z) \leq x \leq \omega(z)$ at $z = R_{\text{steel ball}}$ calculated with (3.1.1). In addition, $z_{1,\text{steel ball}}$ is the height of the radius of curvature of the wavefront R_c at the $z = R_{\text{steel ball}}$ calculated with (3.1.2) and it is specified as

$$z_{1,\text{steel ball}}(x) = \sqrt{R^2_{\text{steel ball}} - x^2} - (R_c - R_{\text{steel ball}}). \tag{3.4.3}$$

Figure 3.14 presents the curvature of radius of the incident wavefronts and the two steel balls measured in this work. In addition, the phase difference of the different curvatures is presented in Figure 3.14.

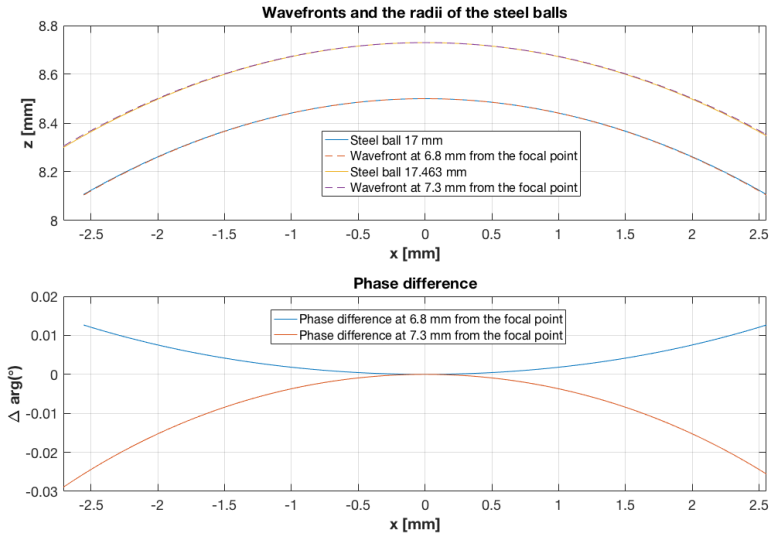

Figure 3.14: Phase matching of spherical objects to the incident beam at 260 GHz. (Up) the radius of curvature of the incident wavefronts and the steel balls, (Down) phase difference of the incident wavefronts and steel balls.

Figure 3.15 illustrates the efficiency phase difference between 220 - 330 GHz. In future research the efficiency should include an amplitude coefficient to more accurately determine the effect of the curvature of radius to the reflection of the incident wavefront.

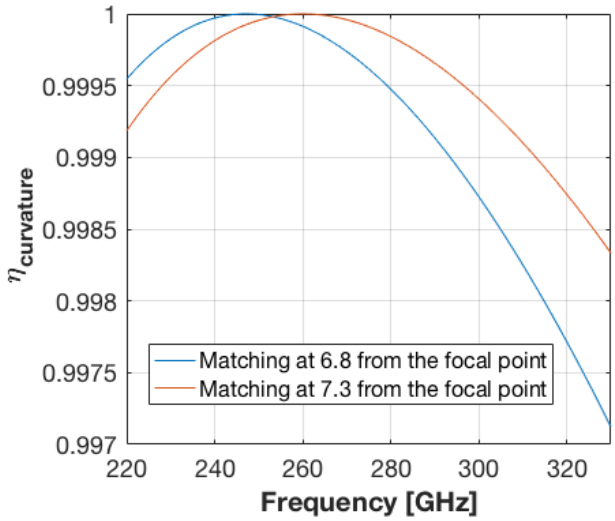

Figure 3.15: Efficiency of the phase difference from 220 GHz to 330 GHZ.

4 Results

This chapter presents and discusses the measurements introduced in Section 3.2. First an overview of the signal processing needed to obtain reliable results is given. After the signal processing methods are determined the verification measurements of planar MUTs are presented and discussed. Lastly the measurement results of MUTs with spherical geometry are presented and discussed.

4.1 Signal processing

4.1.1 Time-domain filtering

In many measurement the raw data will only show some changes in the signal level. Raw data in this sense means the recorded signal data from the PNA. Therefore, the raw data must be processed in order to obtain meaningful results from the measurement. A simple method to post-process the raw data is to calculate the Fourier transform of it, which transforms the measurement from one domain to another, e.g., from frequency domain to time-domain.

The domain switch may be performed by Fourier transform (FT). To optimise computation time many computational environments utilise fast Fourier transform (FFT). Applying FFT to a data in frequency domain will move it to the time-domain or space-domain. Due to the continuous behaviour of the measurement data, the peaks in the time- or spatial-domain will present the multiple reflections of the signal. The signal response in time-domain can be calculated as

$$F(t) = \int_{-\infty}^{\infty} G(f) e^{j2\pi ft} df, \tag{4.1.1}$$

where $F(t)$ is the signal response in time-domain and $G(f)$ is the signal response in frequency domain. Similarly $G(f)$ may be computed back from $F(t)$ as

$$G(f) = \int_{-\infty}^{\infty} F(t) e^{-j2\pi ft} dt. \tag{4.1.2}$$

The time-domain is linked with the spatial domain as

$$r = \frac{tc}{2}, \tag{4.1.3}$$

where r is the distance to the horn antenna.

After the raw data has been transformed from frequency domain to time-domain individual reflections from the MUT can be distinguished from the time-domain. The signal response in time-domain presents multiple peaks with equal time intervals. The first reflection is determined from the first peak after the 0 second point. The second peak is at two times the first signal response and the amplitude value is

usually lower than the amplitude value of the first peak. The signal response in time-domain may be filtered with a filter function. A gaussian filter function may be used, specified as

$$H(r) = e^{-(\frac{r-r_0}{GW})^2}, \tag{4.1.4}$$

where r is the distance from the horn antenna, r_0 is the centre point of the filter function, and GW is the width of the function. The filter is applied to $F(r)$ as

$$\Gamma_{\text{filtered}}(r) = F(r)H(r). \tag{4.1.5}$$

The filtered signal response in time-domain can be now transformed back to frequency domain by applying (4.1.2) or inverse fast Fourier transform (IFFT). The signal has now been filtered and the response only includes one reflection from the MUT. Figure 4.1 represent the filtering process starting from (a) raw measurement data, (b) Fourier transformed measurement data, (c) filtered measurement data in time-domain, and (d) filtered measurement data in frequency domain.

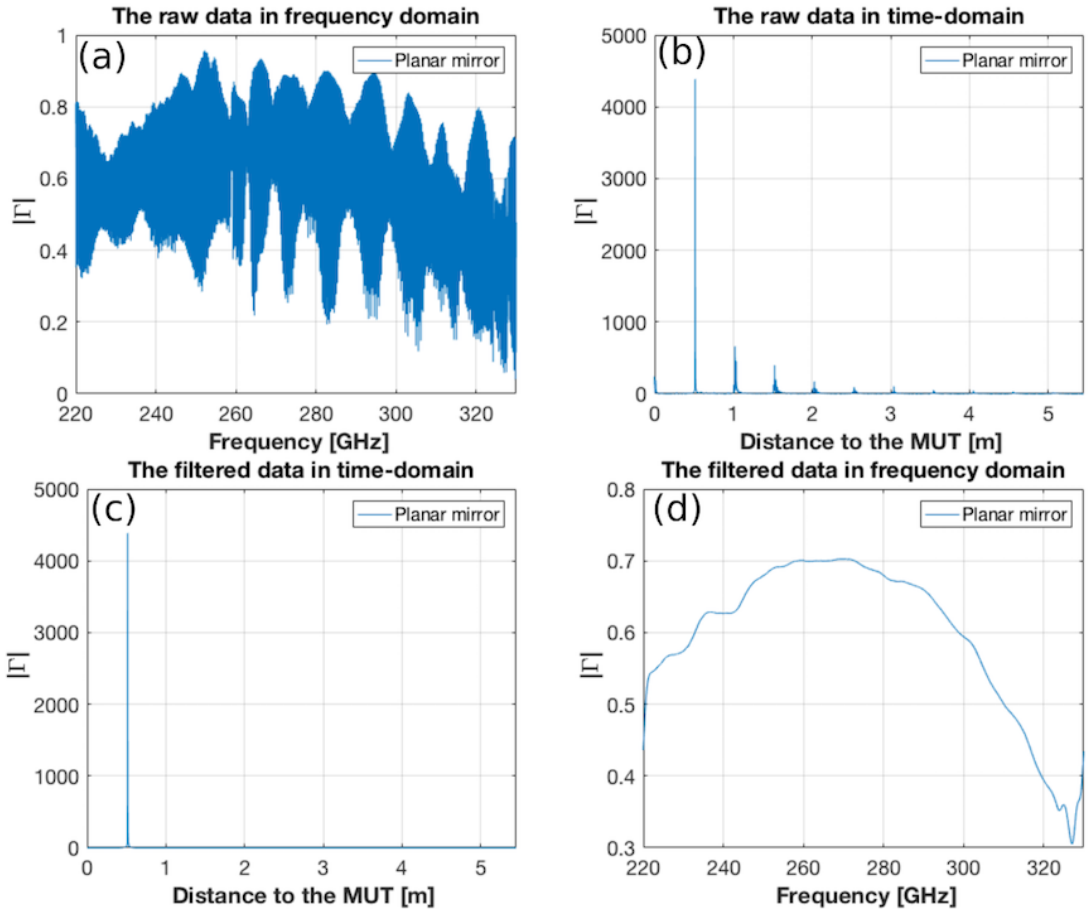

Figure 4.1: Filtering process of a reflection measurement signal measured from a planar mirror. (a) Raw data in frequency domain, (b) raw data in time-domain, (c) filtered measurement data in time-domain, (d) filtered data frequency domain.

The Gaussian filter will only delete the effect of other reflections and the horn antenna

but other artefacts, such as atmospheric attenuation and the effect of distance, still remain in the filtered signal response. The amplitude response of the signal may be further enhanced by measuring a reference short, such as a planar mirror. The amplitude response of the measured material is divided by the amplitude response of the reference short as

$$|\Gamma(f)| = \frac{|\Gamma_{\text{filtered}}(f)|}{|\Gamma_{\text{mirror}}(f)|}, \tag{4.1.6}$$

where $\Gamma(f)$ is the filtered signal response, and $\Gamma_{\text{mirror}}(f)$ is the filtered response of a mirror (reference short). Ideally dividing with amplitude response of a mirror measurement is just dividing by 1, thus in an unideal case the mirror response will calibrate all the measurements with planar geometry.

4.1.2 Phase unwrapping

The phase response of reflection coefficient of the MUT is defined as

$$\text{Arg}(\Gamma(f)) = \arctan(\frac{\text{Im}\{\Gamma(f)\}}{\text{Re}\{\Gamma(f)\}}), \tag{4.1.7}$$

where $\text{Re}\{\Gamma(f)\}$ is the real part of $\Gamma(f)$, and $\text{Im}\{\Gamma(f)\}$ is the imaginary part of the $\Gamma(f)$. The arctan function is not continuous and consists of shifts of 2π, thus periodicity can be extracted with phase unwrapping. The arctan function is unwrapped, i.e., the response is increasing or decreasing without the 2π discontinuity jumps. The phase unwrapping algorithm is defined as in [74] as

$$\phi(f_i) = \phi(f_i) + 2\pi M_\phi, i = 1, 2, ...N - 1, \tag{4.1.8}$$

where f_i is the ith point in the frequency vector and M_ϕ is defined as

$$M_\phi = \begin{cases} M_\phi = 0, & \text{if } i = 1, \\ M_\phi = M_\phi + 1, & \text{if } |\phi(f_{i+1}) - \phi(f_i)| > |\alpha_\phi| \ \wedge \ \phi(f_{i+1}) < \phi(f_i), \\ M_\phi = M_\phi - 1, & \text{if } |\phi(f_{i+1}) - \phi(f_i)| > |\alpha_\phi| \ \wedge \ \phi(f_{i+1}) > \phi(f_i), \end{cases} \tag{4.1.9}$$

where α_ϕ is the tolerance value when the 2π jump is unwrapped.

Now, $\phi(f)$ is linearly extrapolated, and the linearly extrapolated fit is removed from $\phi(f)$ as

$$\text{Arg}(\Gamma(f)) = \phi(f) - O_\phi(f), \tag{4.1.10}$$

where $O_\phi(f)$ is the linearly interpolated fit of $\phi(f)$. The linear fit $O_\phi(f)$ is removed from the unwrapped phase to obtain the actual phase response, and in an ideal case the resulting phase response of a planar mirror would be 0 over the frequency range.

4.1.3 Aliasing

Normally measurements are carried out by measuring a continuous wave. The measurement is based on discrete sampling of the signal, i.e., a number of measurement points or frequency step has to be finite. In case of too few samples the signal might be subject to aliasing. The term alias has many definitions depending on the context it is used. In time-domain an alias is a peak that folds back to the sample bin or window if the Nyquist-Shannon theorem is not enforced. The Nyquist-Shannon theorem states that the measured signal has to be sampled at a frequency of at least twice the highest frequency component of the measured signal.

The Performance Network Analyzer (PNA) used in the measurements is connected to a Vector Network Analyzer Extension Module (VNAX) and the highest frequency measured is a multiple of some other frequency, and thus the highest frequency is cumbersome to determine. Fortunately, the required number of points may be determined with a few assumptions. First it is assumed that the needed alias free distance of the signal is W_{alias} and the distance of the object from the horn antenna is d_{alias}. Next assuming that there are n_{alias} multiple reflections and m_{alias} coefficients, the aliased time instant t_{alias} is determined as

$$t_{\text{alias}} = |n_{\text{alias}}\ t_{\text{center}} - m_{\text{alias}}\ t_{\text{maximum}}|, \tag{4.1.11a}$$

$$t_{\text{center}} = \frac{2d_{\text{alias}}}{c},\ \text{and} \tag{4.1.11b}$$

$$t_{\text{maximum}} = \frac{1}{f_{\text{s}}}, \tag{4.1.11c}$$

where f_{s} is the sampling frequency and it is determined as

$$f_{\text{s}} = \frac{BW}{N_{\text{Signal}} - 1} \tag{4.1.12}$$

where BW is bandwidth of the frequency range and N_{Signal} is the number of measurement points.

In addition, the alias-free distance of the signal is determined as

$$t_{\text{low}} = \frac{2(d_{\text{alias}} - \frac{W_{\text{alias}}}{2})}{c},\ \text{and} \tag{4.1.13a}$$

$$t_{\text{high}} = \frac{2(d_{\text{alias}} + \frac{W_{\text{alias}}}{2})}{c}, \tag{4.1.13b}$$

where t_{low} is the lower boundary of the alias free space and t_{high} is the higher boundary of the alias-free distance of the signal. An alias peak is distorting the measurement if the t_{alias} fulfils the conditions

$$t_{\text{alias}} \geq t_{\text{low}},\ \text{and} \tag{4.1.14a}$$

$$t_{\text{alias}} \leq t_{\text{high}}. \tag{4.1.14b}$$

In general, as the distance to the object grows the signal has more aliased components. To avoid the distortion to the signal is to decrease the distance to the object. This is possible only for free-space method measurements where the free-space path may be adjusted. Fortunately, other options remain, such as increasing the number of sampled points in the measurements.

Figure 4.2 maps regions where aliases appear at distances between 10 cm to 60 cm from the MUT and number of samples of the measurement. The width of the alias-free distance to the signal is 50 mm, when considering up to 9 multiple reflections. Bandwidth is chosen as 110 GHz (330 GHz - 220 GHz).

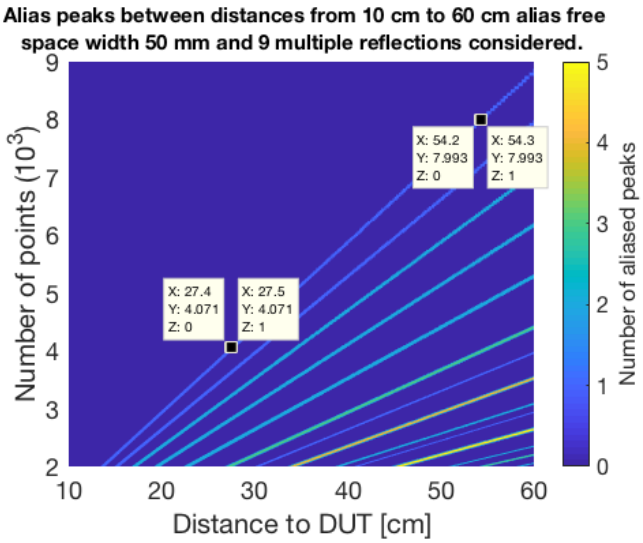

Figure 4.2: Aliasing of measured signal. The alias-free distance of the signal is assumed to be 50 mm and considering up to 9 multiple reflections. At 8047 number of samples aliasing occurs at distance of 49.7 cm.

If the sample is located at 54.2 cm from the horn antenna the number of samples should be 8000 or more. Likewise if the sample is located 27.4 cm from the horn antenna the required number of samples should be 4800 or more. In addition, with narrower bandwidth the number of samples could also be decreased.

4.2 Dynamic range

4.2.1 Planar mirror

The planar mirror was placed to the translational stage and the individual reflections were measured from the mirror by moving the mirror in 0.25 mm steps along the propagation axis of the incident beam. The maximum reflection point was determined from the maximum amplitude value of the reflection coefficient in time-domain. The maximum reflection point is assumed to be the focus point of the off-axis parabolic

(OAP) mirror 2 in the measurement system. Figure 4.3 presents the filtered reflection coefficient amplitude and phase response of the planar mirror.

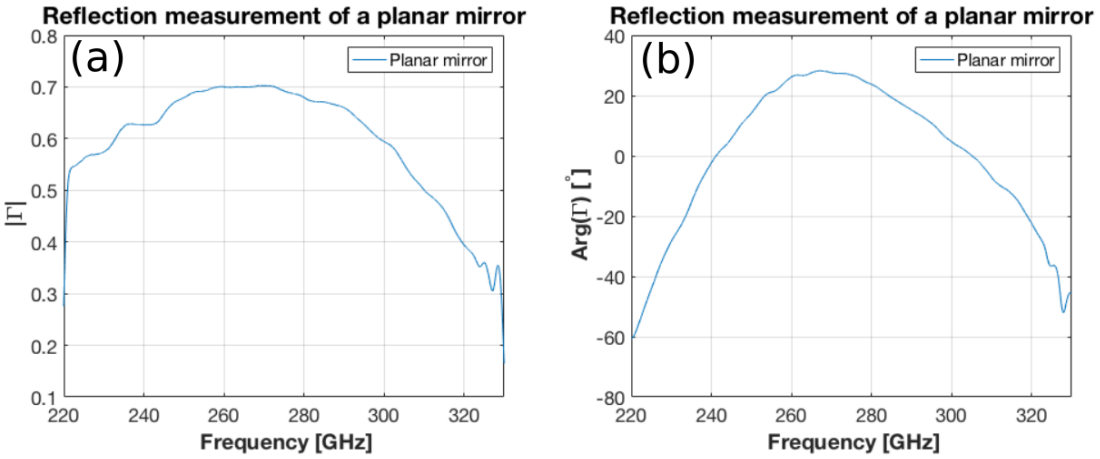

Figure 4.3: The reflection measurement of planar mirror. (a) The reflection coefficient amplitude response, (b) the phase response.

The amplitude response of the filtered data shows a change in the amplitude response of the reflection coefficient in the frequency range presented in Figure 4.3 (a). In addition, same kind of trend is visible in the phase response of the reflection coefficient illustrated by Figure 4.3 (b). The result suggest that there is something that is distorting the measurement also after filtering the signal response. The expected result would be a nearly $|\Gamma| = 1$ throughout the frequency range for a perfect reflector. Fortunately, the amplitude response of the mirror measurement may be used for normalising amplitude responses of planar materials under test.

4.2.2 Radar absorbing material

A piece of radar absorbing material (RAM) was measured to determine the dynamic range of the measurement system. Multiple pieces of RAM were placed in the system in different angles in such a way that measured reflection coefficient would be as low as possible but still detectable from the noise floor. The recorded amplitude would then be the minimum detectable value of the system. The signal-to-noise ratio is defined as

$$\mathrm{SNR} = 20\ \mathrm{Log}(\frac{|\Gamma_{\mathrm{Mirror}}|}{|\Gamma_{\mathrm{RAM}}|}), \tag{4.2.1}$$

where Γ_{RAM} is amplitude of the reflection coefficient of the RAM measurement. Figure 4.4 shows the reflection coefficients of the planar mirror and RAM measurements in decibel (dB) scale.

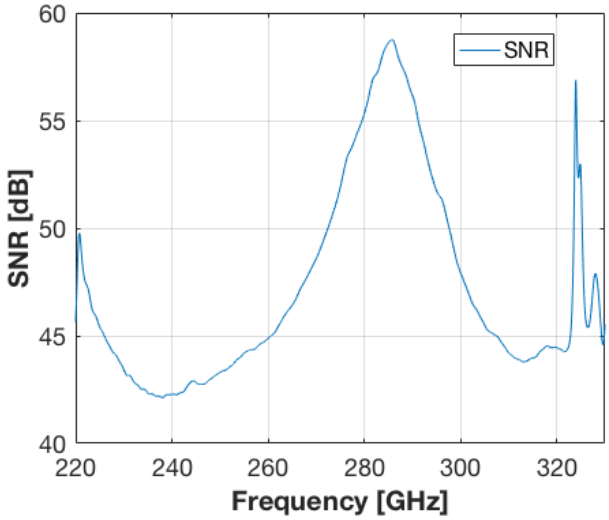

Figure 4.4: The dynamic range of the measurement system. The maximum power detected is the reflection coefficient of the power of the planar mirror, and the minimum power detected is the reflection coefficient of the power of the RAM measurement.

From the results presented in Figure 4.4 the dynamic range can be determined. For the frequency range from 220 GHz to 330 GHz it is about 42 dB or better.

4.3 Validation of the measurement

To validate the measurement setup and to verify that the measured response was actually the response of the MUT, four different materials were measured. All of the measurements were time-gated and the amplitude of the reflection coefficient was normalised with the amplitude of the reflection coefficient of the planar mirror with (4.1.6). The phase response was computed with the unwrapping algorithm presented in Section 4.1.2.

The materials considered were presented in Chapter 3, i.e., a piece of silicon, cyclic-olefin copolymer (COC), and polytetrafluoroethylene (PTFE). Each material was placed on a stand such that the reflection would occur from the material between surrounded by air. Moreover, a piece of RAM was placed a few centimetres beneath the material in order to avoid reflections from the metal building blocks of the measurement system.

4.3.1 Silicon

The well known electric properties of silicon at millimetre wavelengths made the measurement of a piece of silicon a prime candidate for validation of the measurement

system. The thickness of the silicon chip was measured with a thickness dial gauge from Käfer [68]. The thickness was measured to be 510 μm for the silicon chip. The piece was placed on the assumed focus point of the second OAP mirror, similarly as in the planar mirror measurement. Figure 4.5 presents the results of the time-gated and normalised reflection coefficient of the silicon piece.

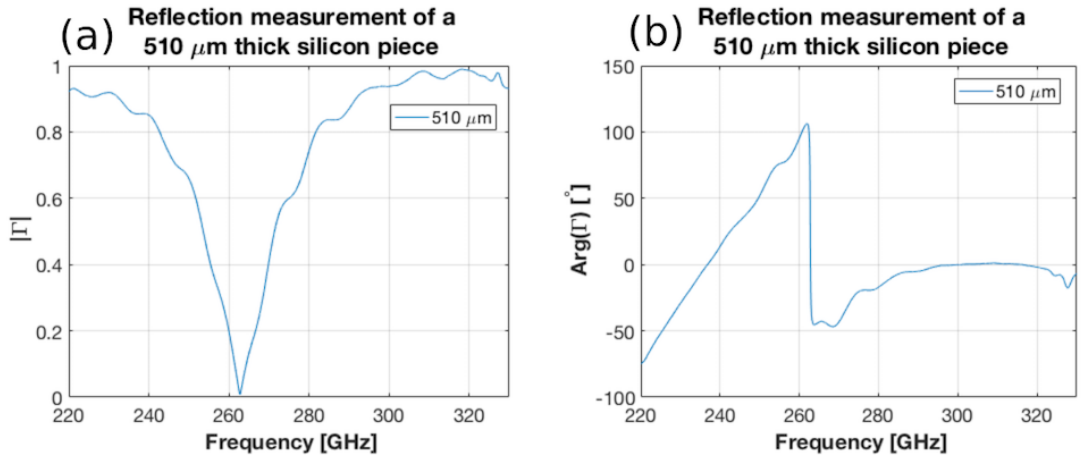

Figure 4.5: The result of reflection measurement of a 510 μm thick piece of silicon. (a) The amplitude response result, (b) the phase response result.

The amplitude of the reflection coefficient is distorted in lower frequencies as well as in the higher frequencies illustrated in Figure 4.5 (a). Fortunately, the clear minimum point around 262 GHz of the amplitude of the reflection coefficient is visible stating that there is a clear etalon effect measured from the piece of silicon. The same zero point is visible also in the phase response of the reflection coefficient illustrated in Figure 4.5 (b). The phase shift denotes the zero point where the phases of the front side reflection coefficient and back side reflection coefficients cancel each other resulting in nearly zero amplitude response. However, the phase response at the lower frequencies act as expected but after about 262 GHz the phase response levels to around zero degrees and the expected sawtooth shape is not visible.

The thicker piece of silicon was also measured with the thickness dial gauge, and the measured value was 540 μm. The thicker piece had also larger surface area than the thinner piece of silicon, which made the positioning of the material under test (MUT) easier. The thicker piece was measured 5 times. Between each measurement the piece was removed from the stand and placed back in order to acquire independent measurement results from different locations on the surface of the MUT. Figure 4.6 shows the results of 5 measurements of the thicker piece of silicon. Both amplitude and phase response of the reflection coefficient of the silicon piece are presented in Figure 4.6.

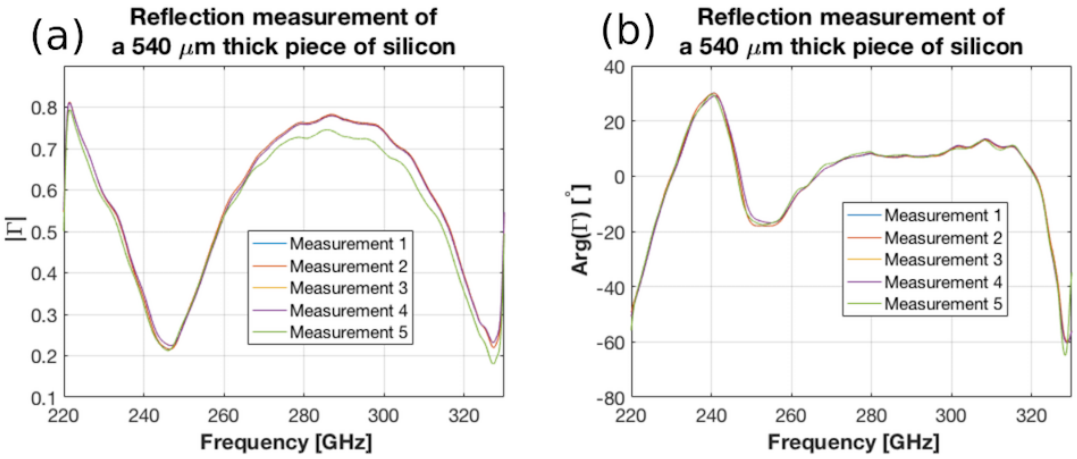

Figure 4.6: The results of reflection measurements of a 540 μm thick piece of silicon. (a) The amplitude response results, (b) the phase response results.

The results of the amplitude of the reflection coefficient, illustrated in Figure 4.6 (a), suggest that the individual measurements are fairly consistent. The result of measurement 5 differs most from the other measurement results, and the reason might be an impurity on the surface. Two minimum points are visible at 246 GHz and at 327 GHz, however, the latter might be also affected by the sharp edges of the time-gating filter function applied. Overall the results suggest a visible etalon effect from the piece of silicon.

The phase responses of the reflection coefficients, presented in Figure 4.6 (b), are more distorted than the amplitude responses. The first phase shift is clearly visible around 246 GHz but then the phase response levels to around 7 degrees. The second phase shift at around 327 GHz is also visible in Figure 4.6 (b) although the phase response is not the expected sawtooth as seen also with the other piece of silicon. The results imply that there might be some artefact present in the phase response since the results are not normalised with the planar mirrors phase response.

4.3.2 Cyclic-olefin copolymer

The electrical properties of cyclic-olefin copolymer (COC) are quite stable at 200-300 GHz, and thus, it is a prime material to be studied at these frequencies [75]. The thickness of the piece of COC was measured with the thickness dial gauge, and value was measured to be 1.98 mm. The piece was moved to the focus point similarly as the planar mirror and 5 individual measurements were recorded of the same piece of COC. The piece was removed and placed back to the focus similarly as the thicker silicon piece. Figure 4.7 presents the measurement results of the amplitude and phase response of the reflection coefficient.

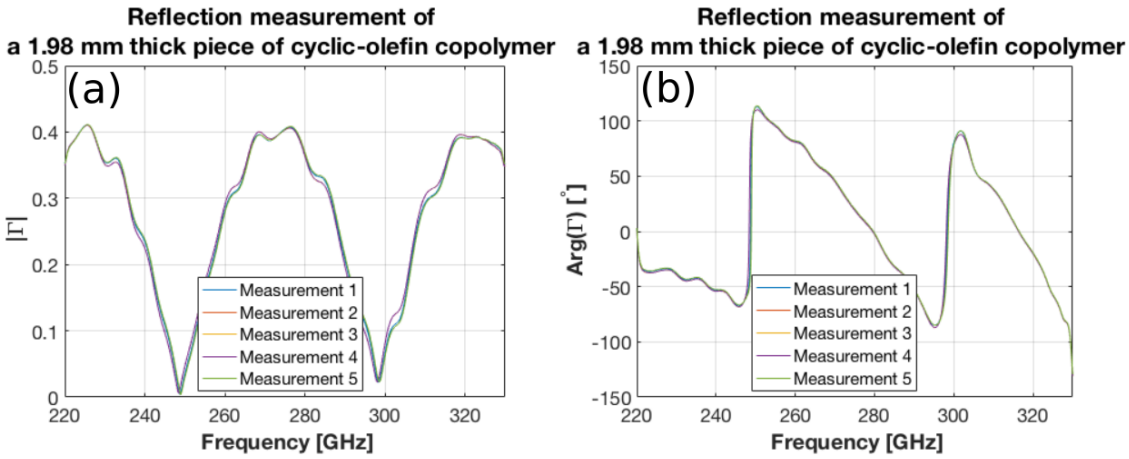

Figure 4.7: The results of reflection measurements of a 1.98 mm thick piece of cyclic-olefin copolymer. (a) The amplitude response results, (b) the phase response results.

The results imply that the results are quite consistent and no large variations in the amplitude or phase responses are visible. The results of the amplitude of the reflection coefficient, illustrated in Figure 4.7 (a), suggest that there is distortion in the amplitude form. Fortunately, the etalon effect is clearly visible with 3 maxima and two minima, first at 249 GHz and second at 297 GHz. The latter minimum implies that the relative permittivity of the COC changes significantly at the higher frequencies since the amplitude value at the 297 GHz is significantly higher than at 249 GHz.

The phase responses of the reflection coefficient, presented in Figure 4.7 (b), have expected sawtooth shaped responses from 247 GHz to 325 GHz. The form is distorted at the lower frequencies as well at the 325 - 330 GHz but overall the responses are similar and the phase shifts at 249 GHz and 297 GHz mark the minima visible in Figure 4.7 (a).

4.3.3 Polytetrafluoroethylene

Polytetrafluoroethylene (PTFE) has quite precisely determined electrical properties at millimetre wavelengths [77]. Therefore, PTFE would be a good candidate for validation measurements. The thickness of the piece of PTFE was measured with a thickness dial gauge, and the measured value was 2.89 mm. The piece was placed on the focal point of the second OAP mirror and 5 individual measurements were recorded of the PTFE. Between each measurement the piece was removed from the focus and placed back to the focus. The results of the amplitude and phase responses of the reflection coefficient are presented in Figure 4.8.

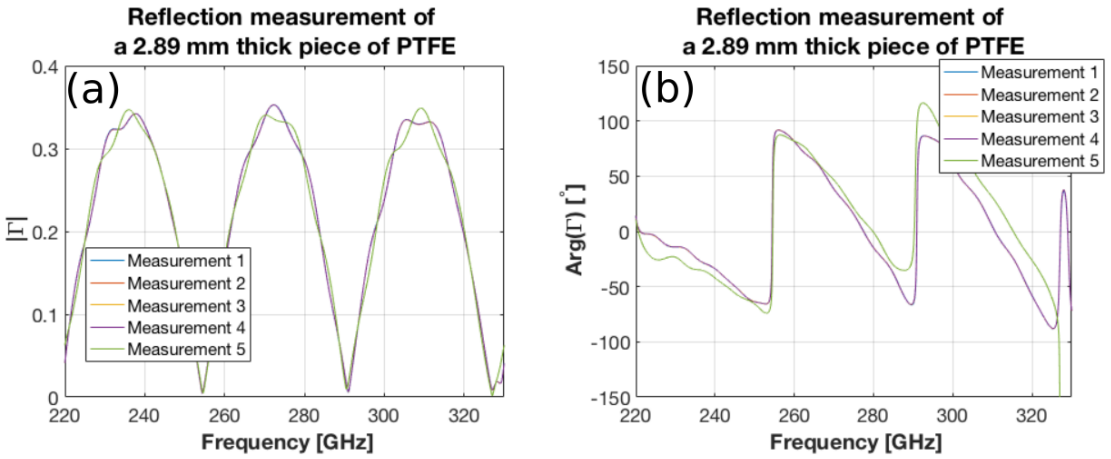

Figure 4.8: The results of reflection measurements of a 2.89 mm thick piece of polytetrafluoroethylene. (a) The amplitude response results, (b) the phase response results.

The amplitude responses of the reflection coefficient, illustrated in Figure 4.8 (a), of measurements 1 - 4 are quite consistent and a slight difference is apparent in measurement 5 relative to other measurements. Overall, the amplitude responses are quite similar and all of them have some sort of the distortion over the frequency range. Fortunately, the expected etalon effect is visible with 3 maxima and 3 minima, first at 255 GHz, second at 291 GHz, and third at 327 GHz.

The phase responses of the reflection coefficient, presented in Figure 4.8 (b), are quite consistent for measurements 1 - 4, but measurement 5 differs from the other measurements. Even though the form of phase response of measurement 5 is significantly different from the other measurements, the first two phase shifts at 255 GHz and 291 GHz are consistent with the other measurements. The difference might be due to uneven surface or impurity on the PTFE piece where measurement 5 was illuminated compared to the other measurements. All of the phase responses present an expected sawtooth shape from 250 GHz to 327 GHz, and some distortion is visible at the lower end of the frequency range as well as at the higher end of the frequency range.

4.4 Spherical objects

4.4.1 Steel balls

The first curved interfaces studied were the 17 mm and 17.463 mm steel balls. Before measuring the steel balls, the system was focused to a screw hole in a solid aluminium breadboard, which was attached to the translational stage, with a flashlight from a mobile phone. The screw hole was illuminated underneath the breadboard and a piece of paper was placed on the breadboard as well as in front of the horn antenna.

The breadboard was moved with the translational stage such that the light from the flashlight coincided with the horn antenna. Figure 4.9 shows the focused measurement setup with the flashlight from the mobile phone. The steel balls could be then easily placed to the propagation axis of the incident beam.

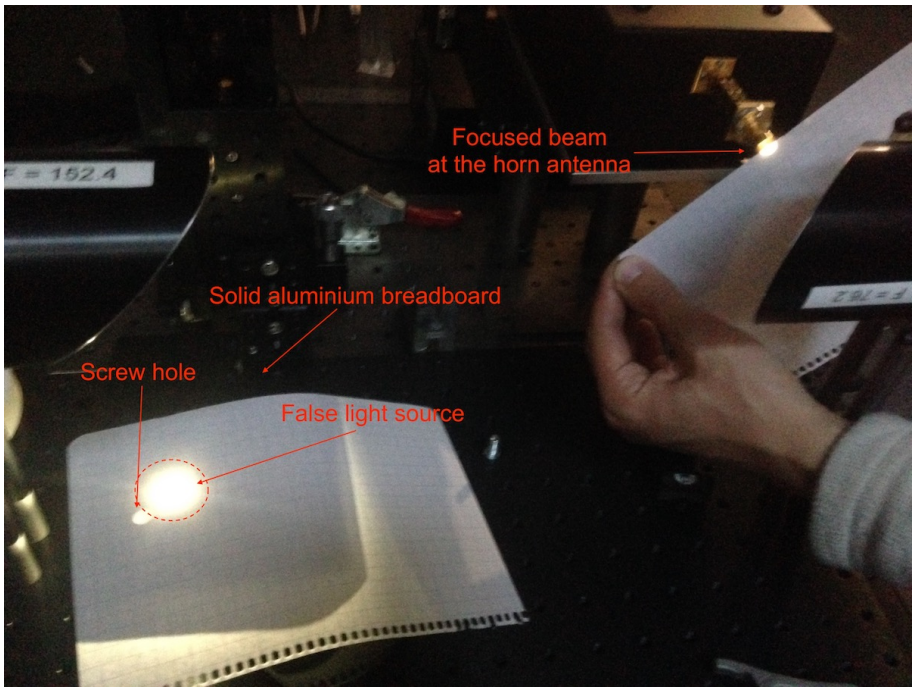

Figure 4.9: The measurement focused to a screw hole in the solid aluminium breadboard. The false light source appears in the picture due to reflection in the lens of the camera and in reality it did not exist.

After the system was focused each steel ball was placed on the screw hole and individual reflection measurements were conducted by moving the steel balls away from the horn antenna in 0.25 mm steps along the propagation axis of the incident beam. Figure 4.10 shows the results of the recorded maximum amplitudes in time-domain, however, presented in spatial-domain.

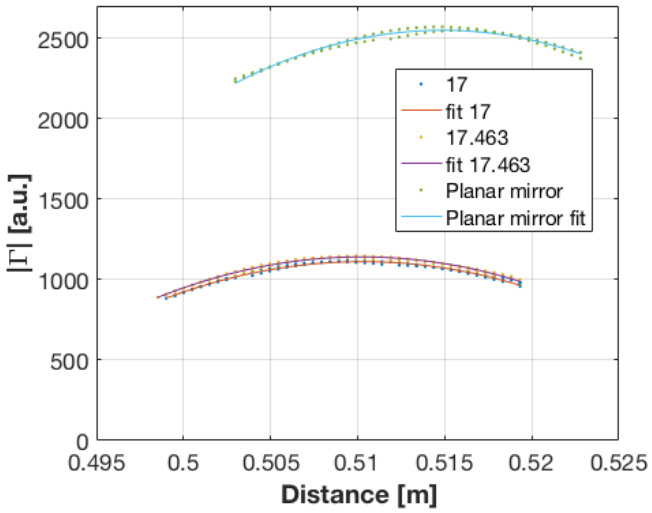

Figure 4.10: The maximum amplitudes of reflection coefficients in time-domain (spatial-domain). The distances where the maximum amplitudes occur: steel ball 17 mm = 50.94 cm, steel ball 17.463 mm = 50.99 cm, planar mirror = 51.49 cm.

The raw data was filtered with a Hann function and it reads

$$HF(i) = \frac{1}{2}(1 - \cos(\frac{2\pi i}{N-1})),\ i = 1, 2, ..., N \tag{4.4.1}$$

where N is the total number of samples. After the Hann function was applied the data was Fourier transformed to time-domain. The maximum amplitude for the steel ball with a diameter of 17 mm was 50.94 cm. Likewise the maximum amplitude for the steel ball with diameter of 17.46 mm at 50.99 cm. The maximum amplitude of the planar mirror was recorded at 51.49 cm

After the maximum distances were determined the raw data was processed as described in Section 4.1, i.e., without the Hann function. Figure 4.11 shows the results of the amplitude and phase responses of the reflection coefficient for the two steel balls as well as the planar mirror.

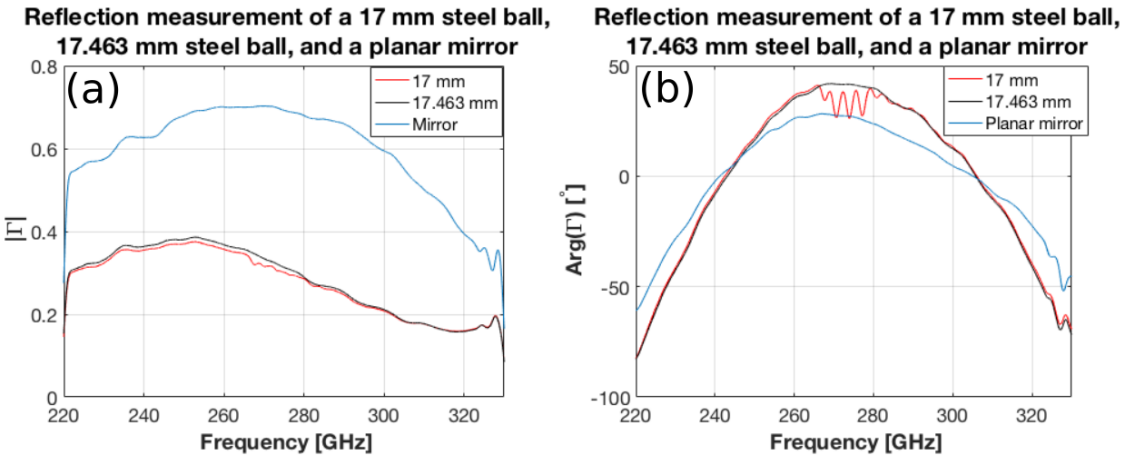

Figure 4.11: The results of steel balls and planar mirror reflection measurements. (a) The amplitude response results, (b) the phase response results.

The results suggest that the amplitude responses have similar shape but the amplitude of the 17.463 mm steel ball has a higher amplitude than that of the 17 mm steel ball. The amplitude responses of the steel balls have similar features compared to the planar mirror, however, the maxima occur at slight different location, for the 17 mm steel ball at 252.7 GHz, for the 17.463 mm steel ball at 253.1 GHz, and for the planar mirror at 270 GHz. In addition, the value decreases faster after the maxima for the steel balls.

The phase responses of the steel balls are fairly similar, however, from 266 GHz to 280 GHz there is some fluctuation in the phase response of the 17 mm steel ball. The phase responses of both steel balls have similar features as the planar mirror, although, the phase responses of the steel balls are steeper compared to the phase response of the planar mirror.

4.4.2 Cling film

The effects of the curved MUT was also examined by using cling film. The cling film was low-density polyethylene based material and the approximate thickness was 30 μm, and thus, the film was nearly invisible for the wavelengths used in the measurement. The cling film was placed in the eye model presented in Section 3.3.7 and a pressure of approximately 306 Pa applied in the cavity. Two sets of measurements were conducted with the film, first with distilled water in the cavity of the wet eye model, and the second set with 0.9 % saline solution. By comparing these results, the effects of the saline solution could be determined.

The measurement sets were conducted by moving the wet eye cavity along the propagation axis of the incident beam. The maximum reflection point along the propagation axis of the incident beam was determined from the highest reflection value in the time-domain. Figure 4.12 shows the results of the amplitude and phase

response of the maximum reflection point from the cling film for both distilled water and saline solution filled cavities.

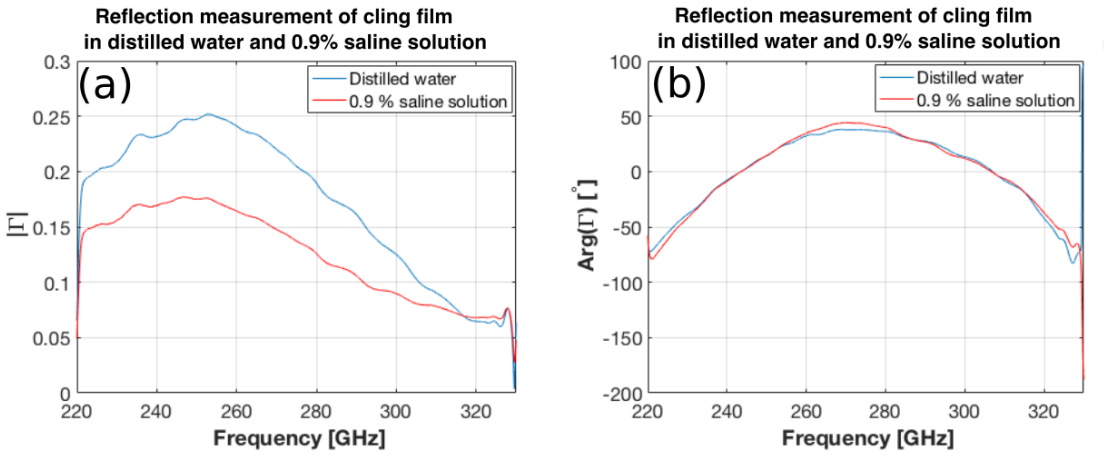

Figure 4.12: The results of cling film measurements. (a) The amplitude response results, (b) the phase response results.

The maximum amplitude responses suggest that the saline solution is more lossy than the distilled water, illustrated in Figure 4.12 (a), as the seawater permittivity model suggested in Section 2.10.1. The shapes of the amplitude responses are similar the maximum of the amplitude of the distilled water is at 247 GHz and the maximum amplitude of the saline solution at 253 GHz. The amplitude response of the distilled water is steeper after the maximum compared with the saline solution. Moreover, the amplitude responses are fairly similar to that of the amplitude responses of both steel balls.

The phase response of the reflection coefficient, presented in Figure 4.12 (b), are similar for both measurements. The phase responses are similar to the phase responses measured for the steel balls. Figure 4.13 illustrates the combined amplitude and phase responses of the reflection coefficient measurements. The results suggest that the cling film does not present a resonance for the used frequencies and the spherical geometry of the water ball is measured as well as the effect of the liquid used behind the cling film. In addition, the result imply that the amplitude response of the cling film results could be used to normalise the amplitude responses of materials with spherical geometry on either distilled water or saline solution.

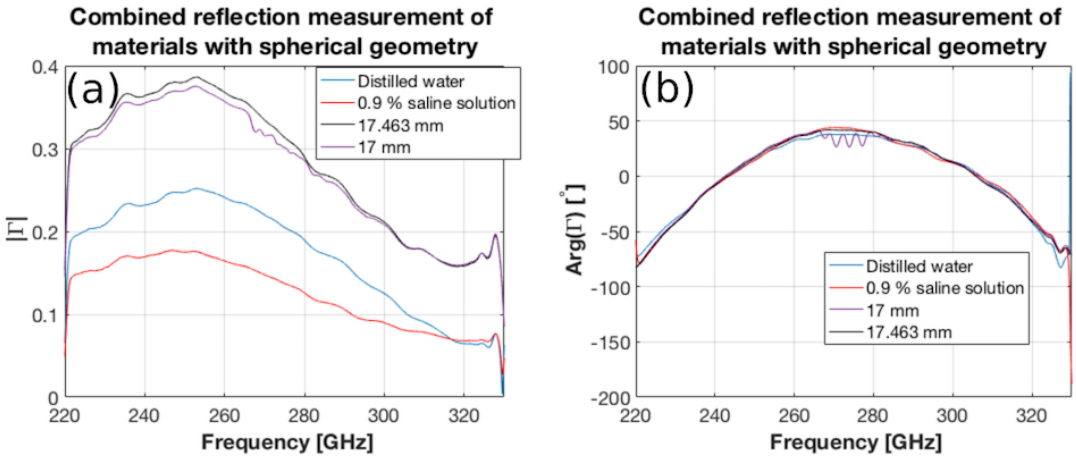

Figure 4.13: The combined reflection measurement results of steel ball measurements and cling film measurements. (a) The amplitude results, (b) the phase response results.

4.5 Human tissue phantom

4.5.1 Contact lens

Two +6 diopter contact lenses were measured by measuring individual reflection coefficients along the propagation axis of the incident beam, similarly as the cling film and steel ball measurements. One contact lens was placed in distilled water over 24 hours. Afterwards the lens was rinsed with distilled water and placed in the eye model before filling the cavity with distilled water. The other contact lens was placed immediately in to eye model after the pack was opened and before the cavity was filled with 0.9 % saline solution. Figure 4.14 presents the amplitude and phase responses of the maximum reflection point of both contact lenses.

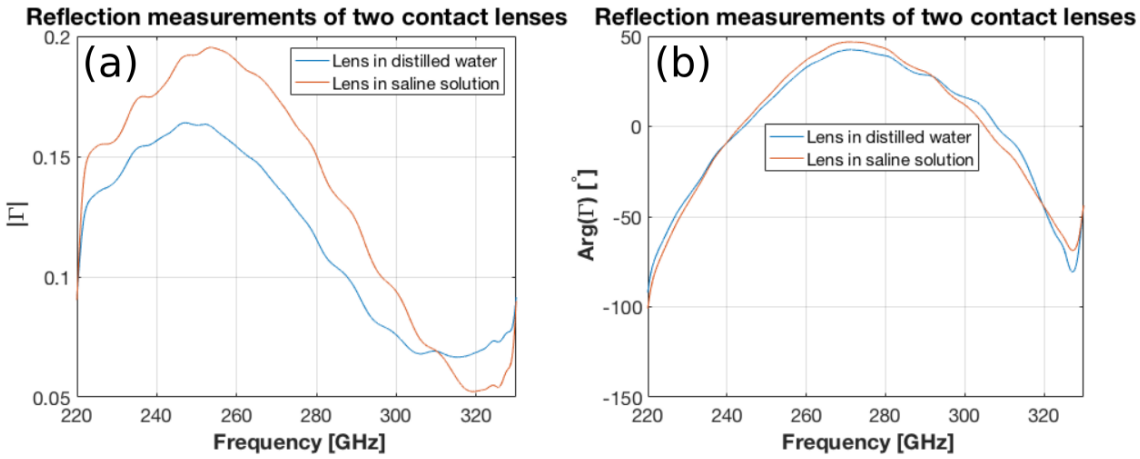

Figure 4.14: Reflection measurements of one contact lens in distilled water and one contact lens in 0.9 % saline solution. (a) The amplitude response results, (b) the phase response results.

Figure 4.14 (a) illustrates the amplitude responses of the reflection coefficient of both contact lens measurements. The maximum amplitude value of the contact lens in saline solution is 0.195 at 254 GHz, whereas the maximum amplitude value of the contact lens in distilled water is 0.164 at 247 GHz. In addition, the decrease in the amplitude value of the contact lens in saline solution is steeper compared with the contact lens in distilled water. The reason might be due to the different radius of curvature lenses have when the lenses are placed in the eye model. Similar feature can be seen with the cling film measurements as well as with the steel ball measurements.

Figure 4.14 (b) shows the phase responses of the maximum reflection point of both contact lens measurements. The phase responses are quite similar over the frequency range. The difference of the phase values at 273 GHz is about 4 degrees. The phase responses are also similar to the cling film and steel ball measurements indicating that the there is no significant difference between the phase responses of the contact lens and other spherical materials measured. Figure 4.15 illustrates the combined amplitude and phase responses of the maximum reflection points for all of the spherical object measurements.

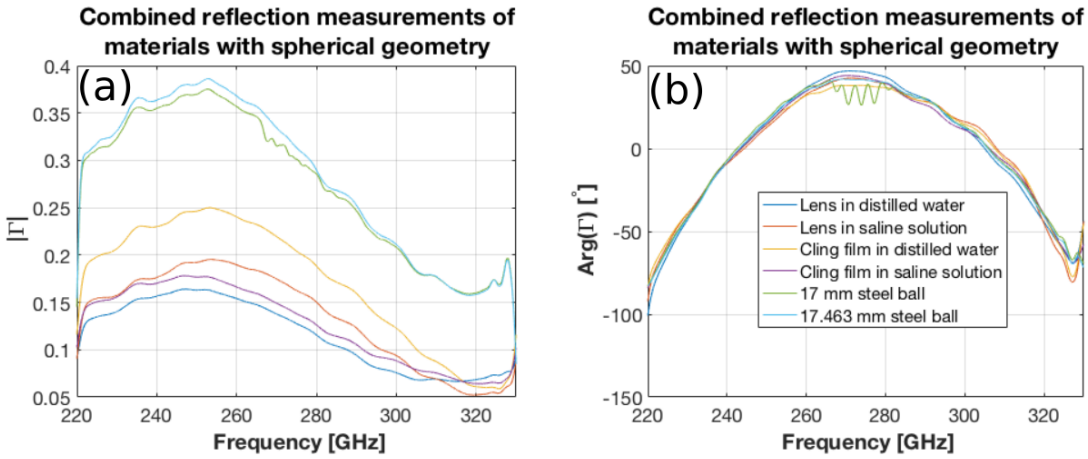

Figure 4.15: Combined reflection measurements of contact lenses and cling film in distilled water and one contact lens in 0.9 % saline solution as well as the steel balls. (a) The amplitude response results, (b) the phase response results.

Figure 4.15 (a) shows that the amplitude responses of the measured spherical objects. The results indicate that the curvature has an effect on the amplitude response, which is visible in the shape of each response. In addition, the amplitude response of the contact lens in distilled water is lower than that of the cling film in distilled water nearly throughout the frequency range. However, the amplitude response of the contact lens in saline solution is lower than that of the cling film in saline solution. Figure 4.15 (b) presents the phase responses of the measured spherical objects. The results verify the similarity of the shapes with all of the spherical objects, and that no etalon effect is visible in the contact lens measurements, at least not in the phase responses.

The maximum reflection points in time-domain for the contact lens in distilled water, the contact lens in saline solution, cling film in distilled water, and cling film in saline solution are 50.97 cm, 51.37 cm, 51.51 cm, and 51.10 cm, respectively. The distance differences are significant indicating that the curvature of the objects has been different. Therefore, the maximum reflection point of the cling film in saline solution is shorter than the maximum reflection point of the contact lens in saline solution indicating that the radius of curvature of the cling film in saline solution would be much shorter than that of the contact lens in saline solution. The difference in the maximum reflection points is 2.7 mm. This assumption is based on the difference in the amplitude level of the two steel balls where the larger radius results in higher amplitude response. The contact lens in distilled water and cling film in distilled water measurements the difference in the maximum reflection points is 5.45 mm.

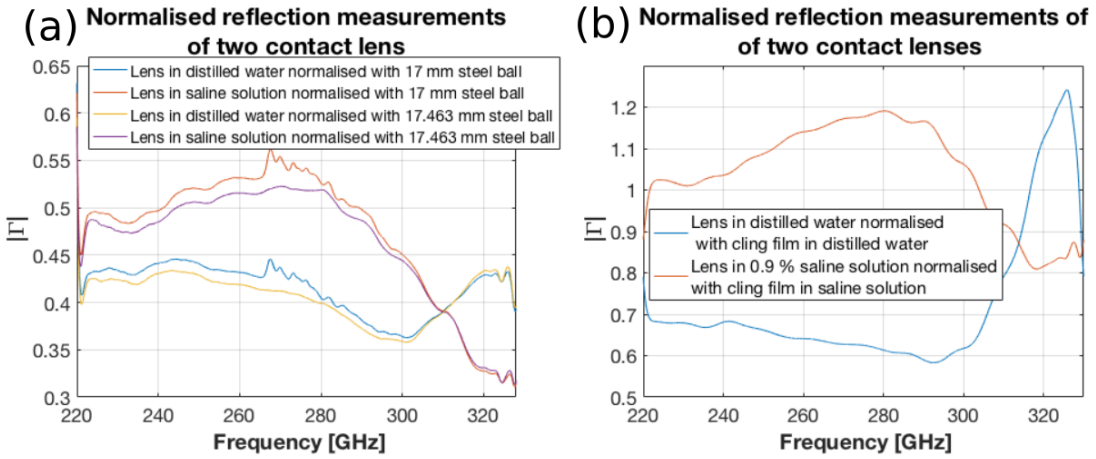

Figure 4.16: Normalised amplitudes of reflection coefficients of the contact lens reflection measurements. (a) Amplitudes normalised with steel ball measurements, (b) amplitudes normalised with cling film measurements.

Another +6 diopter contact lens was placed in the eye model and the cavity was filled with 0.9 % saline solution such that the pressure in the cavity was 306 Pa. The eye model was fastened on the bread board and the maximum amplitude of the reflection was search by manually tuning the translational stage and looking at the amplitude of the reflection coefficient in time-domain. When the maximum amplitude had been found, 4 sets of measurements were conducted. Each set of measurements consisted of 20 individual reflection coefficient measurements over 2 minutes. Figure 4.17 shows the results of the first set of measurements.

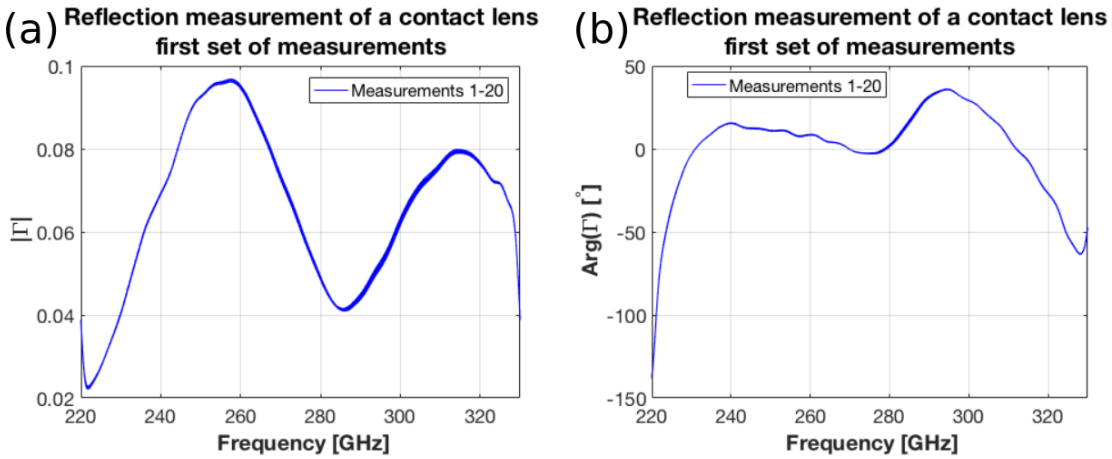

Figure 4.17: The first set of measurements of a contact lens. (a) The amplitude responses, (b) the phase responses.

The results are quite consistent and the results suggest that the radius of curvature has not changed between the measurements, at least not significantly. However, the amplitude responses, presented in Figure 4.17 (a), are not similar to that of other

measurements conducted with spherical geometry. The reason might be that there has been a bubble of air between the contact lens and saline solution.

Figure 4.18 shows the results of the second set of reflection measurements of the same contact lens. The second set was measured almost immediately after the first set. The eye model was not moved between the measurements, nor was it touched between the measurements. The results of the first two sets of measurements are fairly similar and the minimum points at 286 GHz are roughly at the same level.

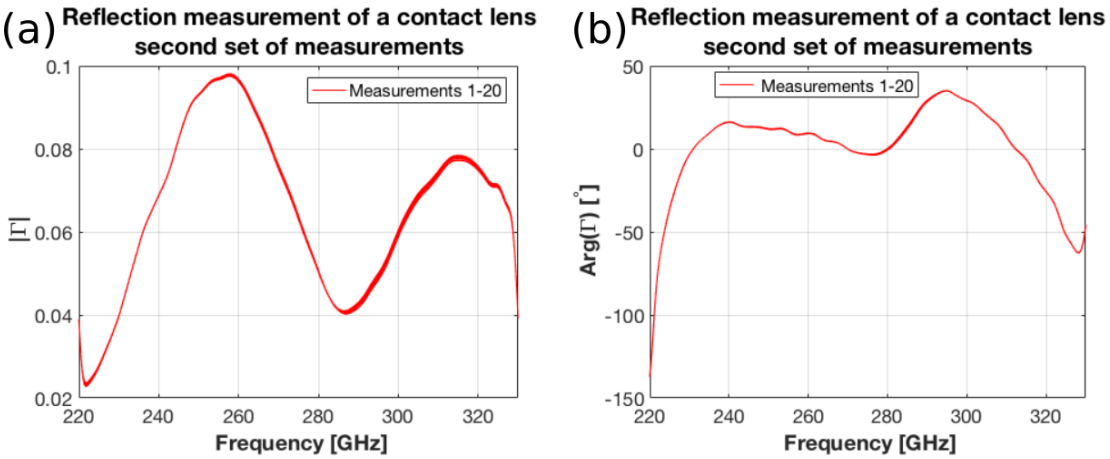

Figure 4.18: The second set of measurements of a contact lens. (a) The amplitude responses, (b) the phase responses.

Figure 4.19 and Figure 4.20 present the results of measured reflection coefficients of third and fourth set of measurements respectively. The third set was measured 15 minutes after the second set of measurements and the fourth set was measured immediately after the third set. The amplitude responses and the phase responses of the third and fourth set of measurements are quite similar.

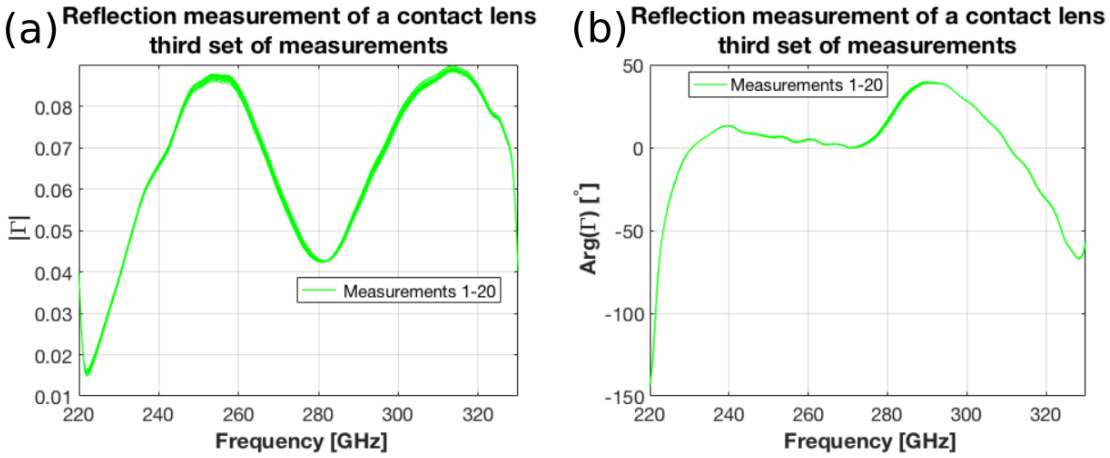

Figure 4.19: The third set of measurements of a contact lens. (a) The amplitude responses, (b) the phase responses.

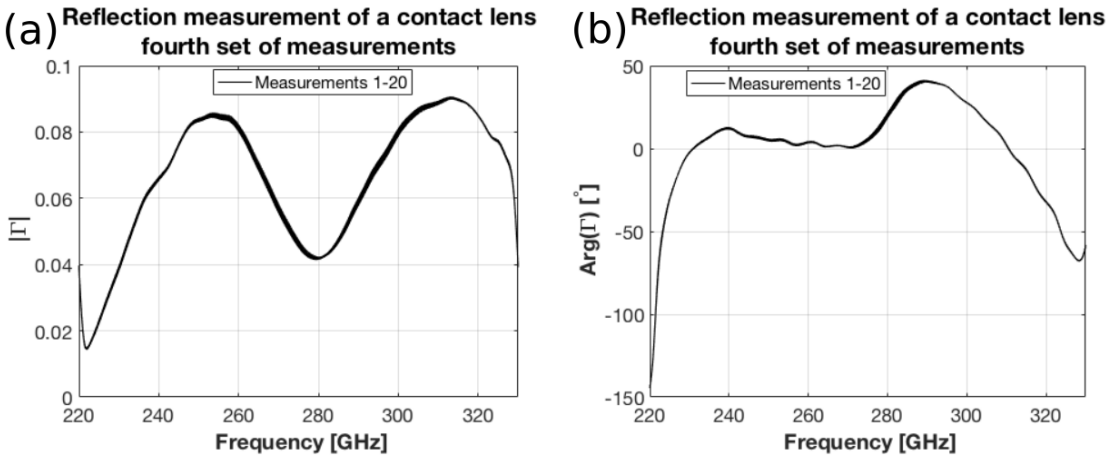

Figure 4.20: The fourth set of measurements of a contact lens. (a) The amplitude responses, (b) the phase responses.

Figure 4.21 (a) illustrates all amplitude responses and phase responses of the four sets of measurements. The differences between the second and third set of measurements are the decrease in the amplitude value around 254 GHz, increase of the amplitude value around 318 GHz, and the shift of the minimum point from 285 GHz to 279 GHz. This would mean that the contact lens has dried between the second and third set of measurements. As the water content of the lens changes the losses in the material decrease and the thickness of the sample also would change due to the hydrophilic behaviour of the contact lens material. However, the decrease of the amplitude value around 254 GHz is not explained with the drying of the contact lens. Another reason might be that the contact lens has leaked saline solution from the cavity and the curvature has changed between the second and third set of measurements. The same can be seen from the phase responses illustrated in Figure 4.21 (b).

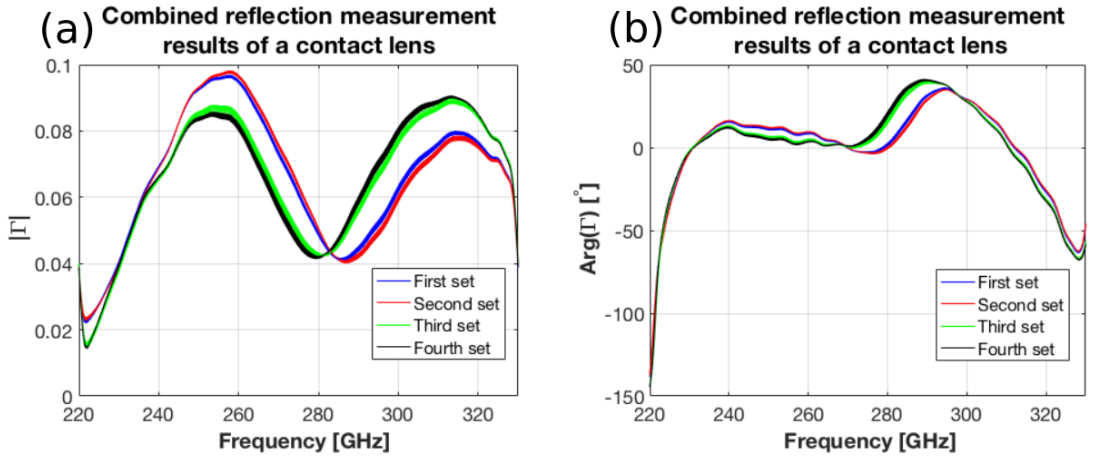

Figure 4.21: The combined reflection measurement results of a contact lens. (a) The amplitude response, (b) the phase response.

5 Uncertainty analysis and parameter estimation

A common uncertainty analysis process is to apply a residual analysis of the simulation and measurement data. A residual analysis in this case is referred as the difference between the estimated value, $\overline{X}_i$, and the observed value X_i. In mathematical terms this means,

$$\overline{r}_i = \overline{X}_i - X_i, i = 1, 2, .., N_\mathrm{r} \tag{5.0.1}$$

where $\overline{r}_i$ is the residual of ith point. In terms of simulation and measurement data estimated value is the simulated value and likewise observed value is the measured value. Generally, the residual analysis may be used for fitting the simulated data to the measured values. A quick and straightforward fitting algorithm is the least square algorithm, and the it reads

$$\min \overline{S} = \sum_{i=1}^{N} \overline{r}_i^2, \tag{5.0.2}$$

where $\overline{S}$ is the sum of squares, and $\overline{r}_i$ is the residual defined by (5.0.1). The best solution may be computed by inserting suitable starting parameter values ($\varepsilon_r^{'}$ and $\varepsilon_r^{''}$) for $\overline{X}_i$ defined by (2.10.4). The sum of squares is then minimised by a minimising function, e.g., in MATLAB *fminsearch*.

In this work the sum of least square fitting is produced with MATLAB *lsqcurvefitting* function [76]. The initial parameter values for $\varepsilon_r^{'}$ and $\varepsilon_r^{''}$ are picked from the literature. The thickness l_r for the simulation is chosen from the dial thickness gauge measurements. The boundary values of the *lsqcurvefitting* function are chosen such that the all of the parameter values are positive. Furthermore, the specific boundaries are presented in each section separately.

5.1 Residuals of verification measurements

The measured materials silicon, cyclic-olefin copolymer, and polytetrafluoroethylene are examined to analyse the overall functionality and accuracy of the measurement system. The results should be close to the values reported in literature to validate the functionality of the measurement system.

5.1.1 Silicon

Table 3 presents the $\varepsilon_r^{'}$ and $\varepsilon_r^{''}$ values used as reference as well as the simulated relative permittivity values that best fit the measurement data. Figure 5.1 illustrates the fitted curve of fitting algorithm as well as the normalised amplitude of the reflection coefficient of the larger silicon piece measurements. The initial parameters for the fitting algorithm are chosen as $\varepsilon_r^{'} = 11.884$ and $\varepsilon_r^{''} = 11{\times}10^{-4}$. Table 4 presents the limits of the parameters.

Table 3: The studied relative permittivity values of silicon at 100-450 GHz as well as the fitted parameter values.

$\varepsilon_r^{'}$	$\varepsilon_r^{''} \times 10^{-4}$	Range [GHz]	Reference
11.884 - 11.882	11 - 6	100 - 450	[77]
11.485	3950	220 - 330	This work (Larger piece)
11.27	11	220 - 330	This work (Smaller piece)

Table 4: The limits of the parameters for the fitting algorithm.

Parameter	Lower limit	Higher limit
$\varepsilon_r^{'}$	11	15
$\varepsilon_r^{''}$	0	1

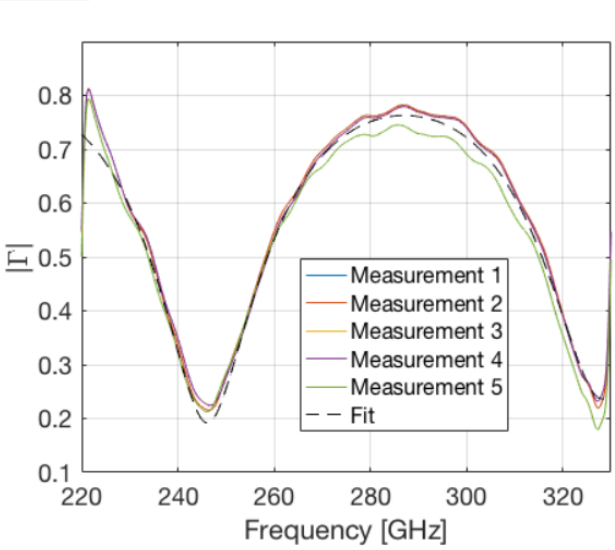

Figure 5.1: Data fit of the larger 540 μm silicon piece. The simulated values of the relative permittivity are $\varepsilon_r^{'} = 11.485$ and $\varepsilon_r^{''} = 0.395$.

The parameters values best fitted to the measurement data are $\varepsilon_r^{'} = 11.485$ and $\varepsilon_r^{''} = 0.395$. However, the measurement data suggest that the silicon would have higher losses than what the literature suggests. The reason might be that there has been some coating on the piece that has not been reported since the piece had been used in other projects previous to this work.

Figure 5.2 shows the fitted curve of the data fitting algorithm as well as the normalised amplitude of the reflection coefficient of the smaller piece of silicon. The same limits and initial parameter values for the $\varepsilon_r^{'}$ and $\varepsilon_r^{''}$ are used for the fitting algorithm.

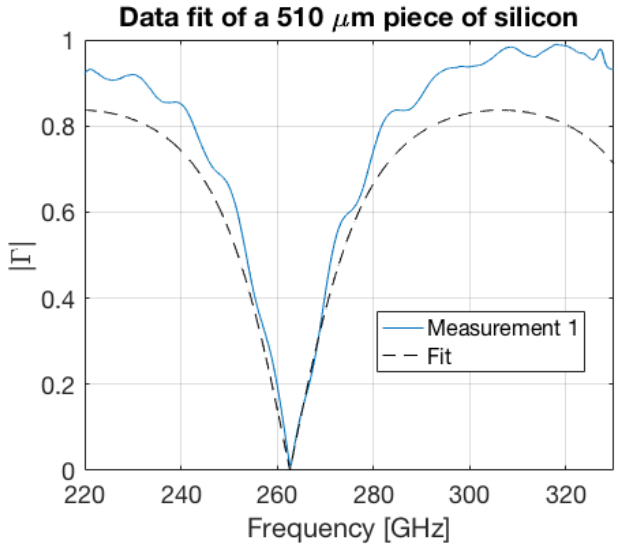

Figure 5.2: Data fit of the larger 510 μm silicon piece. The simulated values of the relative permittivity are $\varepsilon_r^{'} = 11.27$ and $\varepsilon_r^{''} = 11 \times 10^{-4}$.

The result of the data fit is better for the smaller piece. However, the fitted curve and the measurement data do not overlap outside the minimum point at 262 GHz. In addition, the reflection responses away from the 262 GHz are distorted and almost result in an amplitude of 1. The reason the piece is distorted might be due to the unknown coating on the piece since the smaller piece was used in previous projects before this work.

5.1.2 Cyclic-olefin copolymer

Table 5 presents the parameter values of cyclic-olefin copolymer (COC) from the literature as well as the initial parameter values used for data fitting algorithm. Table 6 presents the boundary values used in the data fitting algorithm. Figure 5.3 presents the fitted curve and normalised amplitude responses of the reflection coefficients of the five COC measurements.

Table 5: The studied relative permittivity values of Cyclic-olefin copolymer at 220 - 330 GHz as well as the fitted parameter values.

$\varepsilon_r^{'}$	$\varepsilon_r^{''} \times 10^{-4}$	Range [GHz]	Reference
2.35	2.2	100 - 1000	[78]
2.34	4.46	100 - 1000	[75]
2.308	1.3 - 1.6	140 -220 & 325 - 500	[79]
2.321	9.431 $\times 10^{-7}$	220-330	This work

Table 6: The limits of the parameters for the fitting algorithm.

Parameter	Lower limit	Higher limit
$\varepsilon_r^{'}$	1	3
$\varepsilon_r^{''}$	0	1

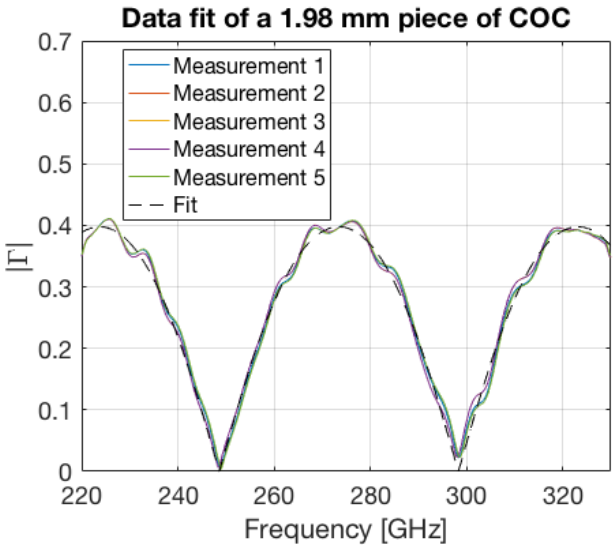

Figure 5.3: Data fit of the five COC measurements. The simulated parameter values are $\varepsilon_r^{'} = 2.321$ and $\varepsilon_r^{''} = 9.431 \times 10^{-11}$.

The results of the five COC measurements and the fitted curve agree fairly good and the simulated values agree with the parameter values used as references. The result of the data fitting suggest that the measurement system is fairly accurate at least with the COC piece. $\varepsilon_r^{'}$ agrees with the literature values, whereas the $\varepsilon_r^{''}$ is much lower than the literature values presented.

5.1.3 PTFE

Table 7 presents the parameter values of polytetrafluoroethylene (PTFE) from the literature as well as the initial parameter values used for data fitting algorithm. Table 8 presents the boundary values used in the data fitting algorithm. Figure 5.4 presents the fitted curve and normalised amplitude responses of the reflection coefficients of the five PTFE measurements.

Table 7: The studied relative permittivity values of polytetrafluoroethylene at 200-400 GHz as well as the fitted parameter values.

$\varepsilon_r^{'}$	$\varepsilon_r^{''} \times 10^{-4}$	Range [GHz]	Reference
2.07	1.3 -1.4	200 - 300	[80]
2.07	4 - 10	90 - 300	[81]
2.071 - 2.069	18 - 11	90 - 300	[82]
2.023	0.241	220-330	This work

Table 8: The limits of the parameters for the fitting algorithm.

Parameter	Lower limit	Higher limit
$\varepsilon_r^{'}$	1	3
$\varepsilon_r^{''}$	0	1

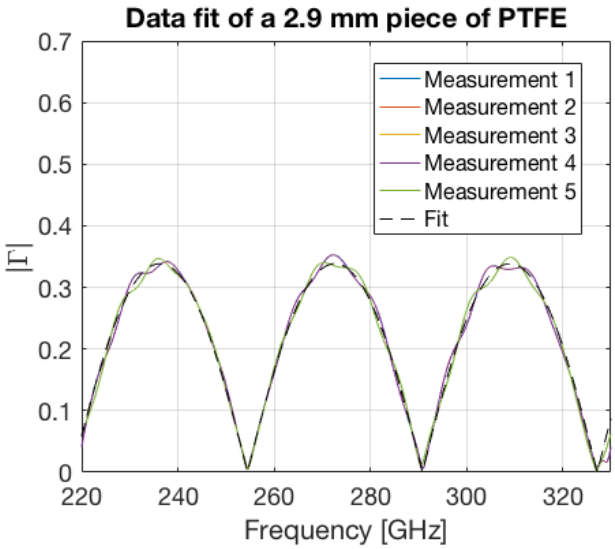

Figure 5.4: Data fit of the five PTFE measurements. The simulated parameter values are $\varepsilon_r^{'} = 2.023$ and $\varepsilon_r^{''} = 2.41 \times 10^{-5}$.

The results of the five PTFE measurements and the fitted curve agree fairly good with each other. The simulated values are similar to the values reported from the literature and the dial thickness gauge measurement. Similarly to the COC measurement the results suggest fairly good accuracy of the measurement system compared with the reported literature values.

6 Conclusions

In this work measurement of human tissue at millimetre wavelengths was studied. In literature review the history of millimetre- and submillimetre-wave technology was discussed as well as possible applications in dermatology, dentistry and ophthalmology were presented. The most promising application in ophthalmology was further analysed with the numerical methods.

The experimental part of this thesis consisted of building a quasi-optical measurement system operating from 220 GHz to 330 GHz. The validation of the measurement system was carried out with four materials with planar geometry. These materials where two different size silicon pieces, a piece of cyclic-olefin copolymer and a polytetrafluoroethylene piece. The material parameters of the cyclic-olefin copolymer and PTFE could be determined fairly close to the literature values presented as reference. However, the parameter values of the two silicon pieces could not be determined to agree with the literature values. Especially, the determined imaginary part of the relative permittivity of the larger silicon piece differs from the literature values.

The human tissue measurements were conducted with a curved contact lens. In addition, 3 materials with spherical geometry where measured. The effect of the spherical geometry was also analysed by their maximum amplitude reflection distances in time-domain. The effect of the radius of curvature with two steel balls with different diameters did not have significant difference in their amplitude responses. However, the cling film and contact lens measurements suggested a significant difference in their amplitude responses and the radius of curvature of these measurements might have been different.

The material parameters of the contact lens could not be determined with the help of the measurements conducted in this work. Furthermore, the four sets of contact lens measurement presented suggested different amplitude and phase response compared to the contact lens measurement conducted by moving the materials in the propagation axis of the incident beam. However, the effect of the curved radius was analysed and a simulation model was included to estimate the effect of the curvature of the material under test to the reflected beam.

6.1 Future research

In the future measurements the contact lens material with planar geometry should be measured. The thickness of the material should be controlled to determine the electrical properties of the material at these wavelengths. If the electrical properties are determined at the used frequencies the fitting of the data for a curved object could be simpler.

The saline solution model presented in this work did not present convincing results at the simulated frequencies and the salinity amount. The relative permittivity of

saline solution should be further analysed and determined to create a reliable model for the used frequency range. The model could be used to obtain a closer-to-reality simulations of the human tissue reflection.

The phase centre change of the Potter horn has to be studied in future research. In addition, larger bandwidth measurements may be conducted with a corrugated horn since the Potter horn may be used only for a 10 % bandwidth. However, the change of the phase centre of the corrugated horn should also be studied.

The coupling of the incident Gaussian beam and the spherical surface should be further analysed. The model presented in this work only considers the phase matching of the spherical object and the incident Gaussian beam. The effect of amplitude distortion due to the spherical geometry should also be studied.

The contact lens measurements conducted in this thesis were normalised by cling film measurements. However, since the radius of curvature was different, the amplitude response of the contact lens could not be normalised to physically possible limits. In future studies the measured spherical objects should have the same curvature of radius to obtain reliable results of the normalised amplitude response.

References

[1] Carpintero, G., García Muñoz, L. E., Hartnagel, H. L., Preu, S., Räisänen, A. V. (eds.), *Semiconductor Terahertz Technology: Devices and Systems at Room Temperature Operation*. Chichester, United Kingdom, John Wiley & Sons Ltd. and IEEE press, 2015.

[2] Penzias, A. A., Burrus, C. A.,"Millimeter-wavelength radio-astronomy techniques," *Annual Review of Astronomy and Astrophysics*, 1973, vol. 11, no. 1, pp. 51-72.

[3] Thaddeus, P., "The short-wavelength spectrum of the microwave background," *Annual Review of Astronomy and Astrophysics*, 1972, vol. 10, no. 1, pp. 305-335.

[4] Cooper, K. B., Dengler, R. J., Llombart, N., Thomas, B., Chattopadhyay, G., Siegel, P. H., "THz imaging radar for standoff personnel screening," *IEEE Transactions on Terahertz Science and Technology*, 2011, vol. 1, no. 1, pp. 169-182.

[5] Tamminen, A., *Developments in imaging at millimeter and submillimeter wavelengths*, Doctoral dissertation, Aalto University, Department of Radio Science and Engineering, Espoo, Finland, 2013.

[6] Taylor, Z. D., Singh, R. S., Bennet, D. B., Tewari, P., Kealey, C. P., Bajawa, N., Culjat, M. O., Stojadinovic, A., Lee, H., Hubschman, J-P., Brown, E. R., Grundfest, W. S. "THz medical imaging: *in vivo* hydration sensing,"*IEEE Transactions on Terahertz Science and Technology*, 2011, vol. 1, no. 1, pp. 201-219.

[7] Taylor, Z. D., Garritano, J., Sung, S., Bajwa, N., Bennet, D. B., Nowroozi, B., Tewari, P., Sayre, J., Hubschman, J-P., Deng, S., Brown, E. R., "THz and mm-wave sensing of corneal tissue water content: electromagnetic modelling and analysis," *IEEE Transactions on Terahertz Science and Technology*, 2015, vol. 5, no. 2, pp. 170-183.

[8] Woodward, R. M., Wallace, V. P., Cole, B., E., Pye, R. J., Arnone, D. D., Linfield, E. H., Pepper, M., "Terahertz pulse imaging in reflection geometry of skin tissue using time-domain analysis techniques," *Proceedings of SPIE 4625, International Symposium on Biomedical Optics; Clinical Diagnostic Systems: Technologies and Instrumentation*, San Jose, CA, USA, 19-25.1.2002.

[9] Siegel, P. H., "Terahertz technology," *IEEE Transactions on Microwave Theory and Techniques*, 2002, vol. 50, no. 3, pp. 910-928.

[10] Mittleman, D. M., Jacobsen, R. H., Nuss, m. C., "T-ray imaging," *IEEE Journal of Selected Topics in Quantum Electronics*, 1996, vol. 2, no. 3, pp. 679-692.

[11] Smith. P. R., Auston, D. H., Nuss, M. C., "Subpicosecond photoconducting dipole antennas," *IEEE Journal of Quantum Electronics*, 1988, vol. 24, no. 2, pp. 255-260.

[12] Grüner, G., Dahl, C. (eds.), *Millimeter and Submillimeter Wave Spectroscopy of Solids*. 1. edition, Berlin, Germany, Springer, 1998.

[13] Hu, B. B., Nuss, M. C., "Imaging with terahertz waves," *Optics Letters*, 1995, vol. 20, no. 16, pp. 1716-1718.

[14] Mittleman, D. M., Gupta, M., Neelamani, R., Baraniuk, R. G., Rudd, J. V., Koch, M.,"Recent advances in terahertz imaging," *Applied Physics B*, 1999, vol. 68, no. 6, pp. 1085-1094.

[15] Taylor, Z. D., Singh, R. S., Culjat, M. O., Suen, J. Y., Grundfest, W. S., Lee, H., Brown, E. R., "Reflective terahertz imaging of porcine skin burns," *Optics Letters*, 2008, vol. 33, no. 11, pp. 1258-1260.

[16] Tewari, P., Kealey, C. P., Bennett, D. B., Bajwa, N., Barnett, K. S., Singh, R. S., Culjat, M. O., Stojadinovic, A., Grundfest, W. S., Taylor, Z. D., "In vivo terahertz imaging of rat skin burns," *Journal of Biomedical Optics*, 2012, vol. 17, no. 4, pp. 20-24.

[17] Reiss, E., Stirman, J. A., Artz, C. P., Davies, J. H., Amspacher, W. H., "Fluid and electrolyte balance in burns," *Journal of the American Medical Association*, 1953, vol. 152, no. 14, pp. 1309-1313.

[18] Woodward, R. M., Cole, B., Wallace, V. P., Arnone, D. D., Pye, R., Linfield, E. H., Pepper, M., Davies, A. G., "Terahertz pulse imaging of in-vitro basal cell carcinoma samples," *Technical Digest. Summaries of papers presented at the Conference on Lasers and Electro-Optics*, Baltimore, MD, 11-11.5.2001, pp. 329-330.

[19] Warden, G. D., "Burn shock resusciation," *World Journal of Surgery*, 1992, vol. 16, no. 1, pp. 16-23.

[20] Wallace, V. P., Fitzgerald, A. J., Shankar, S., Flanagan, N., Pye, R., Cluff, J., Arnone, D. D., "Terahertz pulsed imaging of basal cell carcinoma ex vivo and in vivo," *British Journal of Dermatology*, 2004, vol. 151, no. 2, pp. 424-432.

[21] Arnone, D. D., Ciesla, C. M., Corchia, A., Egusa, S., Pepper, M., Chamberlain, J. M., Bezant, C., Linfield, E. H., Clothier, R., Khammo, N., "Applications of terahertz (THz) technology to medical imagining," *Proceedings of SPIE 3828, Terahertz Spectroscopy and Applications II*, 1999, vol. 3828, no. 1, pp. 209-219.

[22] Klintworth, G. K., "Corneal dystrophies," *Orphanet Journal of Rare Diseases*, 2009, vol. 4, no. 7, p. 38.

[23] Yue, B. Y., Sugar, J., Schrode, K., "Histochemical studies of keratoconus," *Current Eye Research*, 1988, vol. 7, no. 1, pp. 81-86.

[24] Adamis, A. P., Filatov, V., Tripathi, B. J., Tripathi, R. A. M. C., "Fuchs' endothelial dystrophy of the cornea," *Survey of Ophthalmology*, 1993, vol. 38, no. 2, pp. 149-168.

[25] Krachmer, J. H., Feder, R. S., Belin, M. W., "Keratoconus and related noninflammatory corneal thinning disorders," *Survey of Ophthalmology*, 1984, vol. 28, no. 4, pp. 293-322.

[26] Panda, A., Vanathi, M., Kumar, A., Dash, Y., Priya, S., "Corneal graft rejection," *Survey of Ophthalmology*, 2007, vol. 52, no. 4, pp. 375-396.

[27] Doughty, M. J., Zaman, M. L., "Human corneal thickness and its impact on intraocular pressure measures: A review and meta-analysis approach," *Survey of Ophthalmology*, 2000, vol. 44, no. 5, pp. 367-408.

[28] Lackner, B., Schmidinger, G., Pieh, S., Funovics, M. A., Skorpik, C., "Repeatability and reproducibility of central corneal thickness measurement with Pentacam, Orbscan, and ultrasound," *Optometry and Vision Science*, 2005, vol. 82, no. 10, pp. 892-899.

[29] Bennet, D. B., Taylor, Z. D., Tewari, P., Singh, R. S., Culjat, M. O., Grundfest, W. S., Sassoon, D. J., Johnson, R. D., Hubschman, J-P., Brown, E. R., "Terahertz sensing in corneal tissues," *Journal of Biomedical Optics*, 2011, vol. 16, no. 5, 8 p.

[30] Hughes, A., "A schematic eye for the rabbit," *Vison Research*, 1972, vol. 12, no. 1, pp. 123-138.

[31] Bennet, D., Taylor, Z., Tewari, P., Sung, S., Maccabi, A., Singh, R., Culjat, M., Grundfest, W., Hubscman, J-P., Brown, E., "Assessment of corneal hydration sensing in the terahertz band: in vivo results at 100 GHz," *Journal of Biomedical Optics*, 2012, vol. 17, no. 9, 7 p.

[32] Johnson, C., Guy, A., "Nonionizing electromagnetic wave effects in biological materials and systems," *Proceedings of the IEEE*, 1972, vol. 60, no. 6, pp. 692-718.

[33] Räisänen, A., Lehto, A., *Radiotekniikan perusteet*. 11. edition, Helsinki, Finland, Hakapaino Oy, 2003.

[34] International Comission on Non-Ionizing Radiation Protection (ICNRP), "Guidelines for limiting exposure to time-varying electric, magnetic, and electromagnetic fields (up to 300 GHz)," *Health Physics*, 1998, vol. 74, no. 4, pp. 494-522.

[35] Maxwell, J. C., *A Treatise on Electricity and Magnetism*, [Online book], Oxford, England, Clarendo press, 1873. Cited 20.4.2017. Available: http://gallica.bnf.fr/ark:/12148/bpt6k95176j/f1.image

[36] Pozar, D. M., *Microwave Engineering*. 2. edition, USA, John Wiley & Sons Inc., 1998.

[37] Unz, H., "Oliver Heaviside (1850-1925)," *IEEE Transactions on Education*, 1963, vol. 6, no. 1, pp. 30-33.

[38] Lindell, I. V., *Methods for Electromagnetic Field Analysis*. 2. edition, New York, USA, IEEE, 1995.

[39] Kettunen, H., *Complex electromagnetic responses from simple geometries*, Doctoral dissertation, Aalto University, Department of Radio Science and Engineering, Espoo, Finland, 2011.

[40] Sihvola, A., Lindell, I., *Sähkömagneettinen kenttäteoria: 2. Dynaamiset kentät*. 3. edition, Helsinki, Hakapaino Oy, 2002.

[41] Lehto, A., Räisänen, A., *Mikroaaltomittaustekniikka*. 6. edition, Helsinki, Finland, Hakapaino Oy, 2007.

[42] Afsar, M. N., Birch, J. R., Clarke, R. N., "The measurement of properties of materials," *Proceedings of the IEEE*, 1986, vol. 74, no. 1, pp. 183-199.

[43] The MathWorks Inc., MATLAB R2017a for Technical Computing - MathWorks, [Online], 2017. available: www.mathworks.com

[44] Manchester, P. T., "Hydration of the cornea," *Transactions of the American Ophthalmology Society*, 1970, vol. 68, no. 1, pp. 427-461.

[45] Warner, R. R., Myers, M. C., Taylor, D. A., "Electron probe analysis of human skin: Determination of the water concentration profile," *Journal of Investigative Dermatology*, 1988, vol. 90, no. 2, pp. 218-224.

[46] Liebe, H. J., Hufford, G. A., Manabe, T., "A model for the complex permittivity of water at frequencies below 1 THz," *International Journal of Infrared and Millimeter Waves*, 1991, vol. 12, no. 7. pp. 659-675.

[47] Kessel, L., Johnson, L., Arvidsson, H., Larsen, M., "The relationship between body and ambient temperature and corneal temperature," *Investigative Ophthalmology & Visual Science*, 2010, vol. 51, no. 12, pp. 6593-6597.

[48] Meissner, T., Wentz, F. J., "The complex dielectric constant of pure and sea water from microwave satellite observations," *IEEE Transactions on Geoscience and Remote Sensing*, 2004, vol. 42, no. 9, pp. 1836-1849

[49] Jylhä, L., *Modeling of electrical properties of composites*, Doctoral dissertation, Helsinki University of Technology, Department of Radio Science and Engineering, Espoo, Finland, 2008.

[50] Niklasson, G. A., Granqvist, C. G., Hunderi, O., "Effective medium models for the optical properties of inhomogeneous materials," *Applied Optics*, 1981, vol. 20, no. 1, pp. 26-30.

[51] Bruggeman, D. A. G., "Berechnung verschiedener physikalischer Konstanten von heterogenen Substanzen," Annalen der Physik, 1935, vol. 416, no. 7, pp. 636-664.

[52] Orfanidis, S. J., *Electromagnetic Waves and Antennas*. New York, USA, [Online book], 2016, cited 1.6.2017. Available: http://www.ece.rutgers.edu/~orfanidi/ewa.

[53] Singh, R, S., Taylor, Z. D., Tewari, P., Bennet, D., Culjat, M., O., Lee, H., Brown, E. R., Grundfest, W. S., "THz imaging of skin hydration: motivation for the frequency band," *Proceedings of SPIE, Advanced Biomedical and Clinical Diagnostic Systems VIII*, San Francisco, CA, 2010, publication no. 75513.

[54] Lehto, A., Räisänen, A., *Millimetriaaltotekniikka*. 2. edition, Helsinki, Finland, Hakapaino Oy, 2002.

[55] Goldsmith, P. F., *Quasioptical Systems*. New Jersey, USA, IEEE Press, 1998.

[56] Walker, C. K., *Terahertz Astronomy*. Florida, USA, CRC Press, 2016.

[57] Pickett, H. M., Hardy, J. C., Farhoomand, J., "Characterization of a dual-mode horn for submillimeter wavelengths," *IEEE Transactions on Microwave Theory and Techniques*, 1984, vol. 32, no. 8, pp. 363-937.

[58] Johansson, J. F., "A Gauss-Laguerre analysis of the dual-mode ('Potter') horn," *Proceedings of the Fourth International Symposium on Space Terahertz Technology*, Session 4, Los Angeles, California, USA, 1993, pp. 134-148.

[59] Smith, W. J., *Modern Optical Engineering: The Design of Optical Systems*. 3. edition, Boston, USA, McGraw-Hill, 2000.

[60] Peiponen, K-E., Zeitler, J. A., Kuwata-Gonokami, M. (eds.), *Terahertz Spectroscopy and Imaging*. Berlin, Germany, Springer, 2013.

[61] Bergfalk, A., *Optical Simulations and characterisations of antenna integrated YBVO THz detectors*, Master's thesis in wireless photonics and space engineering, Chalmers University of Technology, Department of Microtechnology and Nanoscience, Göteborg, Sweden, 2014.

[62] Keysight Technologies Inc., "Keysight 2-Port and 4-Port PNA Network Analyzer: Data sheet and Technical Specifications," [Online], cited 9.11.2017. Available:http://literature.cdn.keysight.com/litweb/pdf/N5224-90001.pdf?id=2080073.

[63] Virginia Diodes Inc., "VNA Extender - VDI Model: WR3.4-VNAX," [Online], cited 9.11.2017. Available:https://vadiodes.com/index.php/en/products/vector-network-analyzer?id=855.

[64] Radiometer Physics, Pickett-Potter Horn Antennas - Technical Information, [Online], cited: 20.5.2017. Available: http://www.radiometer-physics.de/products/mmwave-and-terahertz-products/antennas-optics/pickett-potter-horn-antennas.

[65] Edmund Optics, Off-Axis Parabolic Metal Mirrors - Technical Information, [Online], cited: 27.6.2017. Available: https://www.edmundoptics.eu/optics/

optical-mirrors/focusing-concave-mirrors/Off-Axis-Parabolic-Metal-Mirrors/#accessories.

[66] Thorlabs, Home, [Online], cited: 18.7.2017. Available: https://www.thorlabs.com/index.cfm.

[67] TOPAS Advanced Polymers, TOPAS 5013L-10 - Technical Information, [Online], cited: 18.7.2017. Available: http://www.topas.com/sites/default/files/TDS_5013L-10_e_US.pdf.

[68] Kafer Messuhernfabrik GmbH & Co. KG, Thickness Dial Gauges - Technical Information, [Online], cited: 25.10.2017. Available: http://www.kaefer-messuhren.de/lang/english/thicknessdialgauges.html

[69] Tampereen Laakerikeskus Oy, 17 mm and 17.463 mm diameter steel balls - Technical Information, [Online], cited 9.11.2017. Available: http://www.tampereenlaakerikeskus.com/tuotteet.html?id=36/&p=3

[70] Wyszecki, G., Stiles, W. S., *Color Science: Concepts and Methods, Quantitative Data and Formulae*, Weinheim, Germany, Wiley-VCH, 2000.

[71] CooperVision, PROCLEAR (omafilcon A) Soft (Hydrophilic) Contact Lenses - Technical Information, [Online],Cited: 18.7.2017. Available: https://coopervision.com/sites/default/files/PI014F_Package%20Insert_omafilcon%20A_Proclear_Sphere%20Asphere%20Toric%20Multifocal.pdf.

[72] Eskimo Finland, Elmukelmu cling film - Technical Information, [Online], cited 1.11.2017. Available: https://www.eskimofinland.fi/eskimo-elmukelmu-30cmx20m

[73] "Measurement of the thickness and refractive index of very thin films and the optical properties of surfaces by ellipsometry," *Journal of Research of the National Bureau of Standards*, 1963, vol. 67, no. 4. pp. 363-377.

[74] Hoffman, M., *Novel techniques in thz-time-domain-spectroscopy*, Doctoral dissertation, Albert Ludwig University of Freiburg, Department of Mathematics and Physics, Freiburg, 2006.

[75] Maestrojuan, I., Palacios, I., Ederra, I., Gonzalo, R., "Use of COC substrate for millimetre-wave devices," *Microwave and Optical Technology Letters*, 2015, vol. 57, no. 2, pp. 371-377.

[76] MathWorks, "lsqcurvefit," [Online], cited: 2.11.2017, Available:https://se.mathworks.com/help/optim/ug/lsqcurvefit.html.

[77] Afsar, M. N., "Dielectric measurement of millimeter-wave materials," *IEEE Transactions on Microwave Theory and Techniques*, 1984, vol. 32, no. 12, pp. 1598-1609.

[78] Cunningham, P. D., Valdes, N. N., Vallejo, F. A., Hayden, L. M., Polishak, B., Zhou. X.-H., Luo, J., Jen, A. K.-Y., Williams, J. C., Twieg, R. J.,

"Broadband terahertz characterization of the refractive index and absorption of some important polymetric and organic electro-optic material," *Journal of Applied Physics*, 2011, vol. 109, no. 4, pp. 043505-043510.

[79] Private communication between Duncan A. Robertson and Aleksi Tamminen 29.9.2015.

[80] Afsar, M. N., "Precision millimeter-wave measurements of complex refractive index, complex dielectric permittivity, and loss tangent of common polymers," *IEEE Transactions on Instrumentation and Measurement*, 1987, vol. IM-36, no. 2, pp. 530-536.

[81] Afsar, M. N., Chi, H., Tkachov, I. I., "Millimeter- and submillimeter-wave transmission and dielectric properties of radome materials," *Proceedings of SPIE 2558, Millimeter and Submillimeter Waves II*, 1995, vol. 2558, no. 1, pp. 73-85.

[82] Afsar, M. N., "Dielectric measurement of common polymers at millimeter wavelength," *1985 IEEE MTT-S International Microwave Symposium Digest*, St. Louis, Mo, USA, 4-6.6.1985, pp. 439-442